



<https://theses.gla.ac.uk/>

Theses Digitisation:

<https://www.gla.ac.uk/myglasgow/research/enlighten/theses/digitisation/>

This is a digitised version of the original print thesis.

Copyright and moral rights for this work are retained by the author

A copy can be downloaded for personal non-commercial research or study, without prior permission or charge

This work cannot be reproduced or quoted extensively from without first obtaining permission in writing from the author

The content must not be changed in any way or sold commercially in any format or medium without the formal permission of the author

When referring to this work, full bibliographic details including the author, title, awarding institution and date of the thesis must be given

Enlighten: Theses

<https://theses.gla.ac.uk/>
research-enlighten@glasgow.ac.uk

Thesis submitted to Department of Aerospace Engineering, Faculty of
Engineering, University of Glasgow

MSc by Research

Computation of Transonic Buffet

© V.Spaine, July 2005

ProQuest Number: 10390521

All rights reserved

INFORMATION TO ALL USERS

The quality of this reproduction is dependent upon the quality of the copy submitted.

In the unlikely event that the author did not send a complete manuscript and there are missing pages, these will be noted. Also, if material had to be removed, a note will indicate the deletion.



ProQuest 10390521

Published by ProQuest LLC (2017). Copyright of the Dissertation is held by the Author.

All rights reserved.

This work is protected against unauthorized copying under Title 17, United States Code
Microform Edition © ProQuest LLC.

ProQuest LLC.
789 East Eisenhower Parkway
P.O. Box 1346
Ann Arbor, MI 48106 – 1346

GLASGOW
UNIVERSITY
LIBRARY:

Contents

Contents	1
List of figures	3
Nomenclature	15
Abstract	19
Acknowledgement	20
1 Introduction	21
1.1 Scope and motivation of project	21
1.2 Transonic Aerodynamics	23
1.2.1 Transonic Aerodynamics of Aerofoils and Wings	23
1.2.2 Transonic buffet of aerofoils and buffet boundaries	25
1.3 Shock induced separation	29
1.3.1 Flow separation	29
1.3.2 Types of separation	30
1.3.3 Shock wave location	35
Increasing incidence	35

Increasing Mach number	35
1.4 Experimental work on aerofoil buffet	36
1.4.1 18% thick circular arc	36
1.4.2 12% thick NACA 16 series aerofoil	43
1.4.3 14% Thick Biconvex Wing	49
1.4.4 CAST 7/DOA1	52
1.5 Computational work on aerofoil buffet	57
1.5.1 18% Circular Arc Aerofoil computations by Levy . . .	57
Computational set-up	57
Results	58
1.5.2 NACA0012 Aerofoil computations by Raghunathan . .	61
Computational Set-up	61
Results	62
1.5.3 NACA0012 Aerofoil computations by Barakos and Drikakis	64
Computational set-up	64
Results	65
2 Description of test cases	68
2.1 Previous work on test cases	68
2.1.1 Test Case 1 : BGK No.1 Aerofoil	68
2.1.2 Test Case 2 : OAT15A aerofoil	73
2.2 Computational set-up for test cases	77
2.2.1 Test Case 1- BGK No.1 Aerofoil	77
2.2.2 Test Case 2 - OAT15A Aerofoil	81

3	Validation and discussion of computational results	86
3.1	BGK No.1 Aerofoil	86
3.1.1	Shock/boundary layer flow field	86
3.1.2	Unsteady mechanism of buffet	101
3.1.3	Grid and time step refinement	112
	Steady flow field	112
	Unsteady flow field	113
3.1.4	Unsteadiness due to employed turbulence models . . .	131
3.2	OAT15A Acrofoil	135
3.2.1	Unsteadiness due to change in angle of attack	135
3.2.2	Unsteadiness due to grid refinement	144
4	Conclusion and Future Work	153
	Appendix	156

List of Figures

1.1	Transonic flow pattern[51]	24
1.2	Buffet boundary from [79]	27
1.3	Buffet onset according to [36]	28
1.4	Region of shock oscillation for BGK No. 1 aerofoil [32]	29
1.5	Variation of normal force with Mach number at α approximately 6° [36]	30
1.6	Types of bubble flow [61]	31
1.7	Sketch illustrating shock boundary layer interaction: (a) bubble separation, (b) bubble and rear separation [61]	33
1.8	Possible types of flow separation on aerofoils [60]	34
1.9	Shadowgraph of steady shock-induced separation with an overlay showing mean velocity profiles, $M=0.79$ and $Re=11$ million	38
1.10	Experimental and computed pressures and skin friction on the aerofoil surface, $M=0.79$ and $Re=11$ million	39
1.11	Surface pressure time histories on the aerofoil with unsteady flow, $M=0.76$ and $Re=11$ million [46]	40

1.12 Time history of mean velocity components from conditionally sampled data for one cycle of flow oscillation, $M=0.76$ and $Re=11$ million; $x/c=0.7$ and $y/c=0.125$ [46]	41
1.13 Unsteady flow domain [52]	43
1.14 Classification of shock/boundary layer interactions and excitation on the aerofoil [58]	45
1.15 Flow domains for a 14% thick biconvex aerofoil $\alpha = 0^\circ$, fixed transition domains [48]	49
1.16 The CAST 7/DOA1 model and instrumentation [79]	53
1.17 Averaged pressure distributions at pre and post-buffet onset conditions [79]	54
1.18 Relation between shock movement, shock strength and trailing edge boundary thickness [79]	55
1.19 Dependence of the reduced shock oscillation frequency on Reynolds number [79]	56
1.20 Computed and experimental pressure distributions on the circular arc aerofoil, $Re = 11 \times 10^6$ [46].	59
1.21 Computed and experimental skin-friction distributions on the circular arc aerofoil, $Re = 11$ million, $M = 0.783$ [72]	60
1.22 Computed and experimental velocity and eddy diffusivity profiles on the circular arc aerofoil, $Re = 11$ million, $M = 0.79$ [46]	61
1.23 Periodic shock motion on the NACA 0012 aerofoil, $M=0.7$, $Re=10$ million and $\alpha = 6^\circ$ [65]	62
1.24 NACA0012 airfoil at $M=0.7$, $Re = 10$ million and $\alpha = 5^\circ$ [65].	63

1.25	Pressure coefficient distribution around the NACA0012 aerofoil:(a)grid size effects, (b)comparisons between linear turbulence models (c)comparison between non-linear turbulence models [7].	66
1.26	Buffet onset for the NACA0012 aerofoil (Re= 10 million, M=0.775, $\alpha = 4^\circ$). Solution obtained using the Spalart Allmaras model(crosses) and the non-linear k- ω model (squares) [7].	67
2.1	Schematic of the BGK No.1 aerofoil showing pressure orifice locations[37]	69
2.2	Location of the fast response transducers[37]	69
2.3	Steady pressure distributions on the upper surface of BGK No.1 aerofoil at various α [37]	71
2.4	Variations of pressure intensities on the upper of BGK No.1 aerofoil at various angles of attack [37]	72
2.5	Ensemble-averaged pressure coefficient at various angles of attack[37]	73
2.6	Mesh around the OAT15A aerofoil	74
2.7	Steady pressure distribution at M=0.73 and $\alpha = 2.5^\circ$	75
2.8	Temporal evolution of the shock location	76
2.9	Mean pressure fluctuations, computational results at $\alpha = 4.5^\circ$ and experimental results at $\alpha = 3^\circ$ and 3.5°	77
2.10	BGK No.1 aerofoil - coarse grid	80
2.11	BGK No.1 aerofoil - fine grid	81
2.12	BGK No.1 aerofoil - finer grid	82

2.13	OAT15A aerofoil - coarse grid	84
2.14	OAT15A aerofoil - Fine grid	85
3.1	Pressure contours and streamlines plot at $M = 0.71$, $Re=20 \times 10^6$ and $\alpha = -0.316^\circ$	87
3.2	Pressure contours and streamlines plot at $M = 0.71$, $Re=20 \times 10^6$ and $\alpha = 1.396^\circ$	87
3.3	Pressure contours and streamlines plot at $M = 0.71$, $Re=20 \times 10^6$ and $\alpha = 3.017^\circ$	88
3.4	Pressure contours and streamlines plot at $M = 0.71$, $Re=20 \times 10^6$ and $\alpha = 4.905^\circ$	89
3.5	Mach number contours and velocity vector plots at $M = 0.71$, $Re=20 \times 10^6$ and $\alpha = 4.905^\circ$	90
3.6	Mach number contours and velocity vector plot at $M = 0.71$, $Re=20 \times 10^6$ and $\alpha = 6.970^\circ$	90
3.7	Shock location related to angle of attack for the different tur- bulence models	91
3.8	Attached flows at two different angles of attacks	92
3.9	Attached and separated flow at $\alpha=3.017^\circ$	92
3.10	Attached and separated flow at $\alpha=4.905^\circ$	93
3.11	Attached and separated flow at $\alpha=6.970^\circ$	93
3.12	Turbulence Reynolds number profiles before the shock ($x/c=0.35$) for different turbulent models, $\alpha = 4.905^\circ$, $M = 0.71$ and $Re = 20 \times 10^6$	94

3.13 Turbulence Reynolds number profiles after the shock ($x/c=0.6$) for different turbulent models for $\alpha = 4.905^\circ$, $M = 0.71$ and $Re = 20 \times 10^6$	95
3.14 Residual plots for $\alpha = -0.316^\circ$, $M = 0.71$ and $Re =$ 20×10^6	96
3.15 Residual plots for $\alpha = 3.017^\circ$, $M=0.71$ and $Re = 20 \times 10^6$	97
3.16 Residual plots for $\alpha = 4.905^\circ$, $M = 0.71$ and $Re =$ 20×10^6	98
3.17 Residual plots for $\alpha = 6.970^\circ$ $M = 0.71$ and $Re = 20 \times 10^6$	99
3.18 Steady surface pressure plots on the upper surface of the BGK No.1 aerofoil at $\alpha = -0.316^\circ$	100
3.19 Steady surface pressure plots on the upper surface of the BGK No.1 aerofoil at $\alpha = 1.396^\circ$	101
3.20 Steady surface pressure plots on the upper surface of the BGK No.1 aerofoil at $\alpha = 4.905^\circ$	102
3.21 Lift coefficient plots using the Baseline model for various an- gles of attack using the coarse grid, $M = 0.71$ and $Re = 20 \times 10^6$	103
3.22 Shock movement with the Baseline model	104
3.23 One cycle of shock movement at $\alpha = 4.905^\circ$, Baseline and coarse grid	105
3.24 One cycle of shock movement at $\alpha = 4.905^\circ$, Baseline and coarse grid	106
3.25 Variations in shock movement, shock height and boundary layer thickness through time for $\alpha = 4.905^\circ$	107

3.26	Experimental unsteady pressures compared with computational unsteady pressures using the Baseline model, $\alpha = 4.905^\circ$, $M = 0.71$ and $Re=20 \times 10^6$	109
3.27	A closer comparison between experimental and computational unsteady pressures using the Baseline model $\alpha = 4.905^\circ$, $M = 0.71$ and $Re=20 \times 10^6$	110
3.28	Variations of pressure spectra at various probe locations at $M = 0.71$, $Re=20 \times 10^6$ and $\alpha = 4.905^\circ$ using the Baseline model and coarse grid.	111
3.29	Effects of grids on surface pressures at $\alpha = -0.316^\circ$	112
3.30	Effects of grids on surface pressure at $\alpha = 1.396^\circ$	113
3.31	Lift coefficient plots using the Baseline model for various angles of attack using the coarse grid, $M = 0.71$ and $Re = 20 \times 10^6$	114
3.32	Lift coefficient plots using time steps of 0.1 and 0.5	115
3.33	Lift coefficient plots using time steps of 0.1 and 0.02	116
3.34	Pressure intensity plots using time steps of 0.1 and 0.02	116
3.35	Shock movement using the three different grids at $\alpha = 4.905^\circ$	117
3.36	Temporal variation in separation regions during an upstream shock movement at $\alpha = 4.905^\circ$ using the Baseline model and the coarse grid.	118
3.37	Temporal variation in separation regions during a downstream shock movement at $\alpha = 4.905^\circ$ using the Baseline model and the coarse grid.	119
3.38	Pressure spectra plots at different probe locations for $\alpha = 4.905^\circ$ using the Baseline model and the fine grid	120

3.39	Temporal variation in separation regions during an upstream shock movement at $\alpha = 4.905^\circ$ using the Baseline model and the fine grid.	121
3.40	Temporal variation in separation regions during a downstream shock movement at $\alpha = 4.905^\circ$ using the Baseline model and the fine grid.	122
3.41	Shock movement using the SST and the Baseline models with the fine grid at $\alpha = 4.905^\circ$	123
3.42	Pressure spectra plots at different probe locations for $\alpha = 4.905^\circ$ using the SST model and the fine grid	123
3.43	Temporal variation in separation regions during an upstream shock movement at $\alpha = 4.905^\circ$ using the SST model and the fine grid.	124
3.44	Temporal variation in separation regions during a downstream shock movement at $\alpha = 4.905^\circ$ using the SST model and the fine grid.	125
3.45	Shock movement using the SST and the Baseline models with the finer grid at $\alpha = 4.905^\circ$	126
3.46	Shock movement using the SST model at $\alpha = 4.905^\circ$	126
3.47	Shock height using different grids	127
3.48	Trailing edge displacement thickness with different grids at $\alpha = 4.905^\circ$	127
3.49	Shock height related to shock movement for the Baseline and SST models at $\alpha = 4.905^\circ$	128

3.50 Trailing edge displacement thickness related to shock movement for the Baseline and SST models at $\alpha = 4.905^\circ$ 129

3.51 Pressure intensities for the Baseline model using two different grid levels at $\alpha = 4.905^\circ$ 130

3.52 Pressure intensities for the Baseline and SST models using the fine grid at $\alpha = 4.905^\circ$ 130

3.53 Reynolds turbulence stress, τ_{xy} profiles along the upper surface for three different turbulence models, $M=0.71$ and $\alpha=4.905^\circ$. 132

3.54 Reynolds turbulence stress, τ_{xx} profiles along the upper surface for three different turbulence models, $M=0.71$ and $\alpha=4.905^\circ$. 133

3.55 Reynolds turbulence stress, τ_{yy} profiles along the upper surface for three different turbulence models, $M=0.71$ and $\alpha=4.905^\circ$. 134

3.56 Lift coefficient plots at two different angles of attacks for $M = 0.73$ and $Re = 3 \times 10^6$ 135

3.57 Streamlines indicating a separation bubble at $\alpha=2.5^\circ$ 136

3.58 Streamlines indicating a separation bubble and trailing edge separation at $\alpha=3^\circ$ 137

3.59 Streamlines indicating a separation bubble, trailing edge separation and an interaction region between the circulation regions at $\alpha=3.5^\circ$ 137

3.60 Streamlines indicating a separation bubble, trailing edge separation and an interaction region between the circulation regions at $\alpha=3.91^\circ$ 138

3.61 Residual plots at two different angles of attack, $M = 0.73$ and $Re = 3 \times 10^6$ 139

3.62	Re_t contours at the separation bubble, $M = 0.73$, $Re = 3 \times 10^6$ and 3°	140
3.63	Re_t contours at the separation bubble, $M = 0.73$, $Re = 3 \times 10^6$ and 3.5°	141
3.64	Turbulent Reynolds number plot along the upper surface for 3 and 3.5 deg.	141
3.65	Turbulent Shear stress, τ_{xy} plots along the upper surface for 3 and 3.5 deg.	142
3.66	Turbulent x-normal stress, τ_{xx} plots along the upper surface for 3 and 3.5 deg.	142
3.67	Turbulent y-normal stress, τ_{yy} plots along the upper surface for 3 and 3.5 deg.	143
3.68	Normal stress profiles in the wake for two different angles of attack, $M = 0.73$ and $Re = 3 \times 10^6$	143
3.69	Temporal variation in separation regions during an upstream shock movement at $\alpha = 3.0^\circ$ using the Baseline model and the coarse grid.	145
3.70	Temporal variation in separation regions during a downstream shock movement at $\alpha = 3.0^\circ$ using the Baseline model and the coarse grid.	146
3.71	Temporal variation in separation regions during an upstream shock movement at $\alpha = 3.91^\circ$ using the Baseline model and the coarse grid.	147

3.72 Temporal variation in separation regions during a downstream shock movement at $\alpha = 3.91^\circ$ using the Baseline model and the coarse grid.	148
3.73 Pressure intensity plot along the upper surface at 4.5 deg.	149
3.74 Shock movement at 4.5 deg.	149
3.75 Pressure intensity plot along the upper surface at 5 deg.	150
3.76 Pressure intensity plot along the upper surface at 5.5 deg.	150
3.77 Temporal variation in separation regions during an upstream shock movement at $\alpha = 3.91^\circ$ using the Baseline model and the fine grid.	151
3.78 Temporal variation in separation regions during a downstream shock movement at $\alpha = 3.91^\circ$ using the Baseline model and the fine grid.	152

List of Tables

2.1	Numerical parameters used for test case 1	78
2.2	Details of the finite volume grids used for test case 1	80
2.3	Numerical parameters used for test case 2	83
2.4	Details of the finite volume grids used for test case 2	83
4.1	Summary of experimental work done on the BGK No.1 aerofoil	157
4.2	Summary of experimental work on the Joukouski aerofoil . . .	158
4.3	Summary of experimental work done on the WTEA II aerofoil	158
4.4	Summary of experimental work done on the 12% thick NACA 16 series aerofoil	159
4.5	Summary of experimental work done on the NACA 0012 . . .	159
4.6	Summary of experimental work done on the 14% thick bicon- vex aerofoil	160
4.7	Summary of experimental work done on the Cast 7/DOA1 aerofoil	160
4.8	Summary of experimental work done on the NACA 631-012 . .	161
4.9	Summary of experimental work done on the 18% circular acr .	161

Nomenclature

c	Chord
c_f	Skin Friction coefficient
c_p	Pressure coefficient
C_L	Lift coefficient
e	Energy
E	Total energy
$E(\kappa)$	Energy spectral density
f	Dominant (buffet) frequency
f_0	Pitching frequency
$\mathbf{F}, \mathbf{G}, \mathbf{H}$	Flux vectors
h	Enthalpy
h_0	Stagnation enthalpy
H	Total enthalpy
$\mathbf{i}, \mathbf{j}, \mathbf{k}$	Cartesian unit vectors
k	Kinetic energy of turbulent fluctuations per unit mass
\mathbf{I}	Identity matrix
J	Jacobian matrix of transformation
l	Characteristic eddy size

M	Freestream Mach number
\mathbf{n}	Unit normal to a streamline (natural coordinates)
P, P^*	Non-dimensional pressure, dimensional pressure
Pr	Prandtl number
p	Pressure
ρ	Density
q	Dynamic pressure
q	Heat flux component
\mathbf{R}	Vector of residuals
Re	Reynolds Number (based on root chord length)
Re_T	Turbulent Reynolds number (μ_T/μ)
S	Entropy
s	Direction along streamline (natural coordinates)
t, t^*	Non-dimensional time, dimensional time
T	Temperature
u, v, w	Cartesian velocity components
U_∞, U_{inf}	Freestream velocity
\mathbf{W}	Vector of independent flow variables
x, y, z	Cartesian coordinate system

Greek Symbols

α	Angle of attack
$\Delta\mathbf{W}$	Vector of conservative updates
ϵ	Dissipation per unit mass

η	Kolmogorov length scale
γ	Ratio of specific heats
μ	Molecular viscosity
μ_T	Turbulent eddy viscosity
ω	Specific dissipation rate, magnitude of vorticity vector
ϕ	Helix angle
ρ	Density
ξ, η, ζ	Curvilinear coordinates

Subscripts

<i>crit</i>	critical
<i>i</i>	inlet conditions
<i>rms</i>	root mean square
∞	Freestream value

Superscripts

*	Dimensional quantity
-	Time averaged component i.e. $\bar{\rho}$
'	Turbulent fluctuation component i.e. ρ'
^	Vector of variables in conservative form i.e. $\hat{\mathbf{F}}$
~	Instantaneous component i.e. \tilde{C}_p

Acronyms

<i>CFL</i>	Courant-Friedrichs-Levy
<i>PMB</i>	Parallel multi-block
<i>RANS</i>	Reynolds-Averaged Navier Stokes
<i>RET</i>	Turbulent Reynolds number (μ_T/μ)
<i>S - A</i>	Spalart Allmaras
<i>SST</i>	Shear Stress Transport

Abstract

The computation of the unsteady aerodynamic phenomenon of buffet is becoming more feasible with the advent of faster computers and better numerical methods. This thesis is concerned with the computation of the Reynolds Average Navier-Stokes equations (RANS) in an attempt to further the understanding of the physics related to transonic buffet despite RANS being an approximation. The report concentrates on 2-dimensional (2-D) buffet of two supercritical aerofoils and comparisons of experimental and computational results are presented. Different turbulence models were employed in the computations. Results show that both steady and unsteady flow fields are heavily dependent on the turbulence models used. The two equation SST and Baseline models are found to be the most reliable models in predicting the onset of buffet. However, the Baseline model tends to over-predict the intensity of the buffet phenomenon. A comparison of various turbulence properties was made in order to explain why buffet occurs at certain angles of attack. Detailed time and grid refinement studies were also performed, although further grid refinement is necessary.

Acknowledgement

I would like to give my sincere thankfulness to my project supervisor Prof. K. Badcock for giving me the opportunity to work in the field of Computational Fluid Dynamics. His guidance and support were most appreciated during my university years.

The financial support provided by EPSRC and BAE Systems is gratefully acknowledged.

I would also like to thank my Head of Department and the Accommodation Office for their support during the difficult stages of my studies.

I also want to thank my mother and my younger brother. Because of their financial and spiritual support, I have been able to come to Glasgow and study at an advanced academic level.

I am grateful to all the present and past members of the CFD Laboratory at Glasgow University especially Dr. G. Barakos for their help and many useful discussions we had during the project.

Last but not least, I thank the almighty Lord for his grace.

Chapter 1

Introduction

1.1 Scope and motivation of project

One of the most challenging problems in computational fluid dynamics is the computation of unsteady viscous flows around aerofoils. Turbulence and viscous effects are of fundamental importance to the aerospace industry, being paramount in aerodynamic design. This is becoming even more important because, as the design of aircraft, helicopters and jet engines is improved, a large number of unsteady phenomena appear that have serious implications in terms of achievable performance or safety. As the speed and memory capacity of computers continues to increase, the computation of unsteady flows is becoming more feasible, however it is still quite expensive. In addition, relatively little effort has been spent in the systematic analysis of the time-accurate computations of unsteady flows. Current efforts have been focused on improving our understanding and modelling of complex, viscous, unsteady flow phenomena such as turbulence, transition and shock-boundary layer in-

teraction.

The present study deals with the computations of the RANS equations for 2-D aerofoils in transonic and high Reynolds Number flows. Two test cases were studied in this project; test case 1 involves work done on the BGK No.1 supercritical aerofoil and test case 2 is on the OAT15A supercritical aerofoil with a blunt trailing edge. Previous work on test case 1 has mainly been experimental work by Lee[32,34,36,37], whilst previous work on the OAT15A aerofoil has been both experimental and computational work done at ONERA[12]. 2-D aerofoil buffet computations can now be conducted at relatively low computational costs and there are large quantities of experimental data available for validation.

Buffet was detected over fifty years ago but the physics and cause of the periodic shock motion is still not fully understood. This study aims at improving our knowledge of the self-sustained motion of shock waves in a buffet flow regime. At transonic flow conditions, many unsteady phenomena are associated with shock wave interactions with separated regions. The resulting pressure fluctuations can cause control surface oscillations known as aileron buzz, periodic flows in supersonic intakes and cascades, and many other undesirable unsteady effects [36].

The onset of buffet can be predicted by numerical methods using fast computers. Viscous effects such as viscous-inviscid interactions can be numerically simulated on modern computers with relatively low CPU costs. However, the efficiency in predicting buffet onset using computational methods still has room for improvement.

Solving the Navier-Stokes equations is usually done by averaging the conser-

vation equations, Reynolds Average Navier-Stokes (RANS) equations. These equations were proposed by Osborne Reynolds over a century ago. In the Reynolds-average approach to turbulence, all of the flow parameters are assumed to be composed of a mean and a fluctuating quantity. Averaging the Navier-Stokes equations gives rise to terms that must be modelled, known as Reynolds stresses. The presence of Reynolds stresses means that the RANS equations are not closed. Some approximations are needed to represent the Reynolds stresses. The approximations introduced are called turbulence models. The models mainly used in this study are the $k-\omega$, SST and Baseline two equation models and the Spalart Allmaras one equation model. The equations, therefore must be used with caution if they are to be used to understand flow physics.

1.2 Transonic Aerodynamics

1.2.1 Transonic Aerodynamics of Aerofoils and Wings

Transonic flow occurs when there is mixed sub- and supersonic local flow in the same flow field (typically with freestream Mach numbers from $M = 0.6$ or 0.7 to 1.2). Usually the supersonic region of the flow is terminated by a shock wave, allowing the flow to slow down to subsonic speeds. As the Mach number increases, shock waves appear in the flow field, getting stronger as the speed increases. Figure 1.1, taken from Mason[51], shows the development of the flow with increasing Mach number, starting from subsonic speeds.

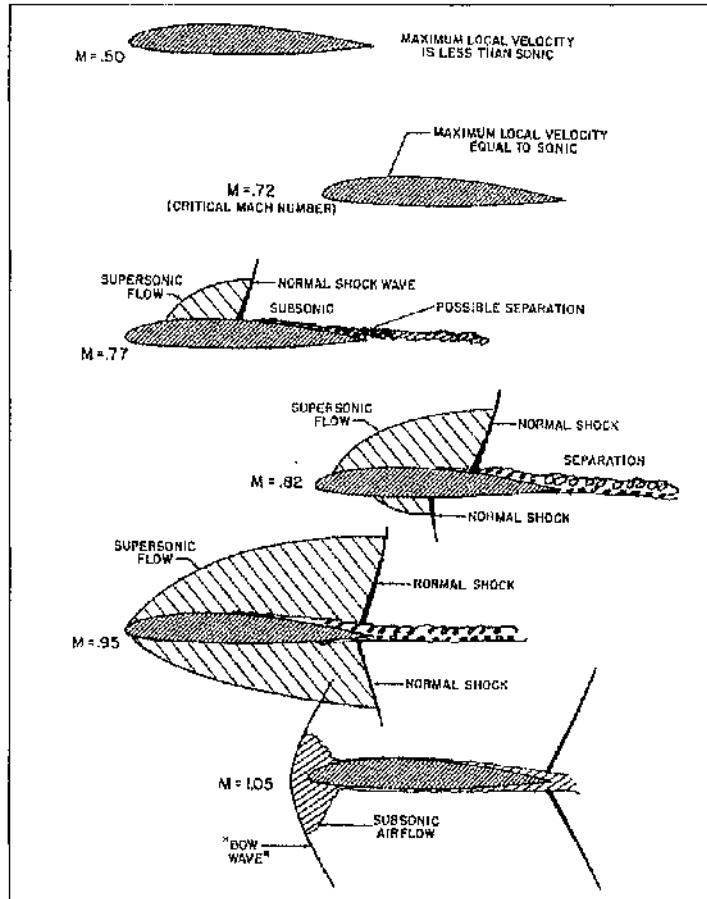


Figure 1.1: Transonic flow pattern[51]

At some Mach number the flow becomes sonic at a single point on the upper surface where the local flow reaches its highest speed. This is the critical Mach number. As the Mach number increases further, a region of supersonic flows develops. Normally the flow is brought back to the subsonic region by the occurrence of a shock wave in the flow. As the Mach number increases, the shock moves aft and becomes stronger. As the Mach number continues to increase, a supersonic region and shock will develop on the lower

surface. As the Mach number approaches unity, the shocks move all the way to the trailing edge. Finally, when the Mach number becomes slightly greater than one, a bow wave appears just ahead of the aerofoil, and the shocks at the trailing edge become oblique, many variations in the specific details of the flow field development are possible, depending on the specific geometry of the aerofoil.

1.2.2 Transonic buffet of aerofoils and buffet boundaries

Buffeting is the dynamic response of an aircraft structure, such as a wing, to unsteady forces acting on it. The buffet loads at transonic speeds are far more severe than those at low subsonic or supersonic, that is why this review mainly concentrates on transonic buffeting. Transonic buffet is of greater importance in terms of aircraft manoeuvrability and structural integrity considerations. The process is essentially driven by the interaction of the shock wave with the boundary layer which influences the development of the shock-induced separation or rear separation. The divergence of an aerofoil's trailing edge pressure can be used to estimate the magnitude of buffet loads. A normal practice in buffet aerodynamics is to define a buffet boundary. An example of one of the early definitions of the buffet boundary illustrated in a lift versus Mach number plot is shown in Figure 1.2. Thomas[79] defined the onset boundary to be a curve separating the regions where the flow is essentially attached or partially separated and those where the flow is fully separated. In the subsonic region the boundary coincides with the maximum

lift versus Mach number curve. As the flight speed is increased, a shock wave is formed and it moves rearwards and finally reaches the trailing edge of the aerofoil. Separation will disappear and we have a buffet-free supersonic flow. For thin wings at small incidence, this condition can be reached even before the shock wave has attained an intensity great enough to initiate buffeting. There is a buffet-free corridor whereby it is possible for a suitably designed supersonic aircraft to pass through the transonic region without encountering buffeting. The onset of buffet is defined similarly for fighter and transonic aircraft, but permissible operation of the aircraft excursion into the buffet regime is different. For a combat aircraft, light buffeting is defined as the first appearance of sizeable vibrations noticed by the pilot and the aircraft can safely operate in that regime. The margin set for moderate buffeting represents the highest values of instantaneous pull-ups or turn rates at which the weapon platform may still be effective in releasing stores or carrying out a tracking mission. Heavy buffet is determined by the structural limits of the aircraft and should be avoided at all costs. For transport aircraft during normal cruise, the aircraft may encounter a strong gust which carries it over the buffet boundary. However, excursion inside this boundary for any prolonged period of time is not permissible.

Pearcy[60] and Pearcy and Holder[61] defined one of the earliest methods to determine buffet onset. Buffet onset is determined by the Mach number or incidence when the bubble reaches the trailing edge and bursts. This can also be obtained from the divergence of the trailing edge pressure. Mabey[48] also defined another method for determining buffet onset using unsteady forces or pressure measurements. In two-dimensional aerofoil testing, a convenient

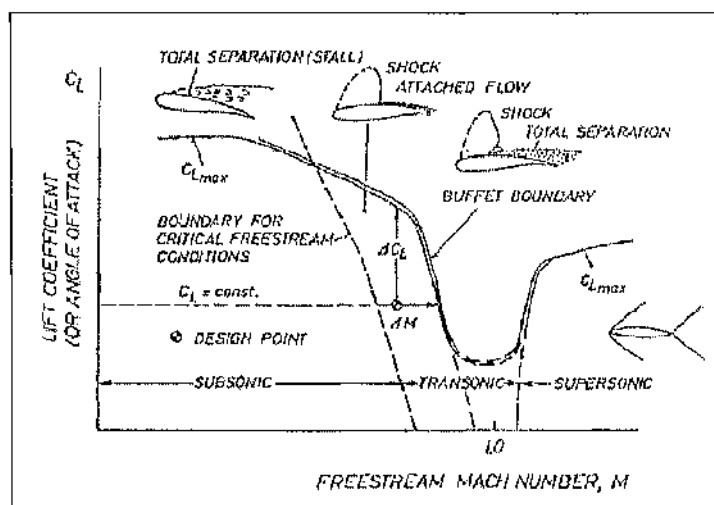


Figure 1.2: Buffet boundary from [79]

quantity to use is the unsteady normal force obtained either from integration of the unsteady pressures on the aerofoil surfaces or from direct measurement with a force balance. Lee and Tang[43] used the divergence of this quantity to define the buffet boundary. Lee and Ohman[42] have shown experimentally that for the BGK No.1 aerofoil, large fluctuations in the normal forces are detected at Mach number approximately 0.733. It is shown in Figure 1.3 that the aerofoil can experience a large normal force from a small excursion into the buffet regime at transonic flow conditions. The source of this behaviour is associated with the presence of the periodic shock motions.

Figure 1.4 shows the region where shock oscillation occurs for the BGK No. 1 aerofoil. Comparison with Figure 1.3 shows the region where large values of normal force fluctuation is detected lies inside the shock oscillation region. This region where discrete frequency oscillations occur increases in dimension for thicker supercritical aerofoils.

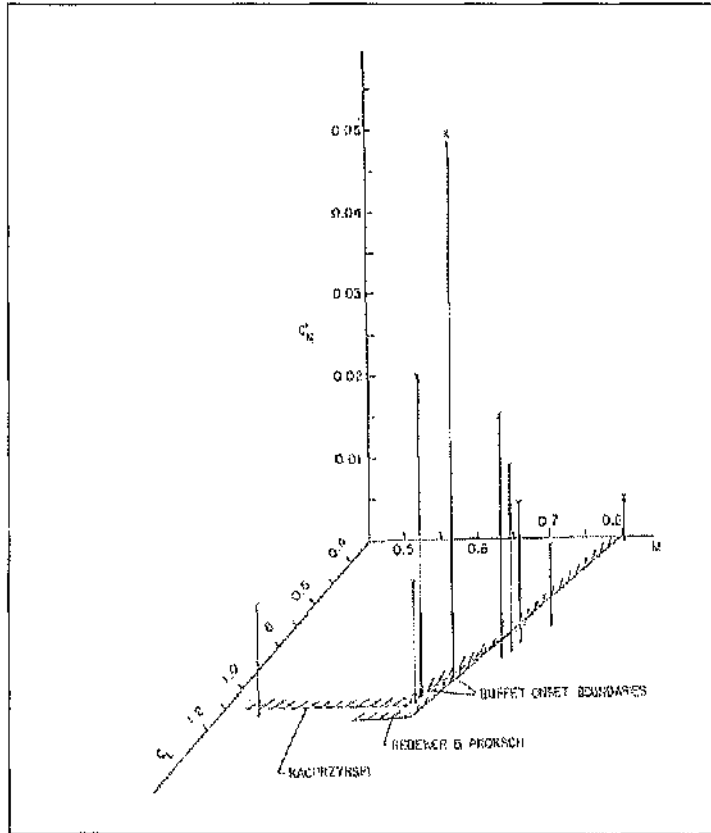


Figure 1.3: Buffet onset according to [36]

The excursion into the buffet regime is shown in Figure 1.5 where α is fixed at approximately 6° and the Mach number varied from 0.6 to 0.81. The results obtained by Lee for the BGK No.1 aerofoil show the fluctuating normal force to increase almost linearly from $M = 0.6$ to 0.69. The onset boundary is crossed at $M = 0.615$ and the shock oscillation region begins at $M = 0.67$. Between $M = 0.67$ and $M = 0.69$, the shock is very weak and the normal force continues to increase approximately in a linear manner. A maximum normal force is located at $M=0.733$ close to the design value of

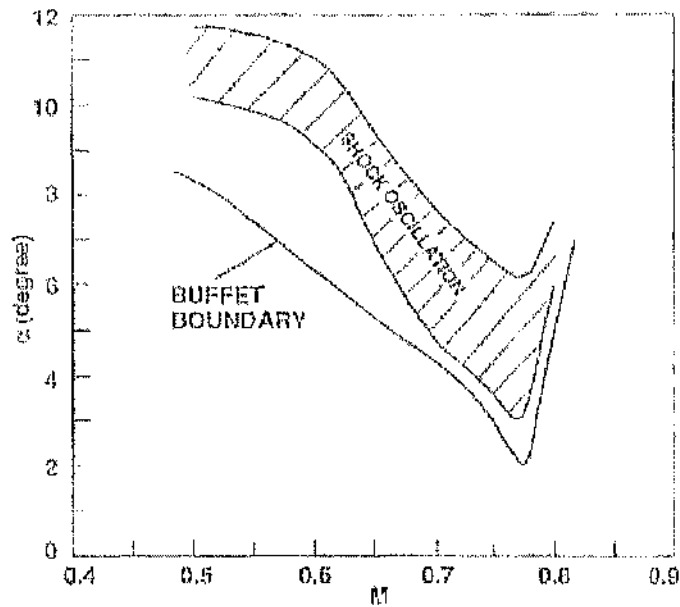


Figure 1.4: Region of shock oscillation for BGK No. 1 aerofoil [32]

0.75. The slope of the graph for $0.616 < M < 0.69$ is much smaller than for $0.69 < M < 0.733$ where fairly strong shock oscillations occur in the latter range of M . At the higher values of Mach numbers ($M > 0.733$), the shock weakens and the pressure field due to shock oscillations decreases with increasing M , resulting in a decrease in the normal force.

1.3 Shock induced separation

1.3.1 Flow separation

Some familiar types of flow separation encountered in or around engineering structures are shown in Figure 1.6. These are quasi 2-D bubble separations

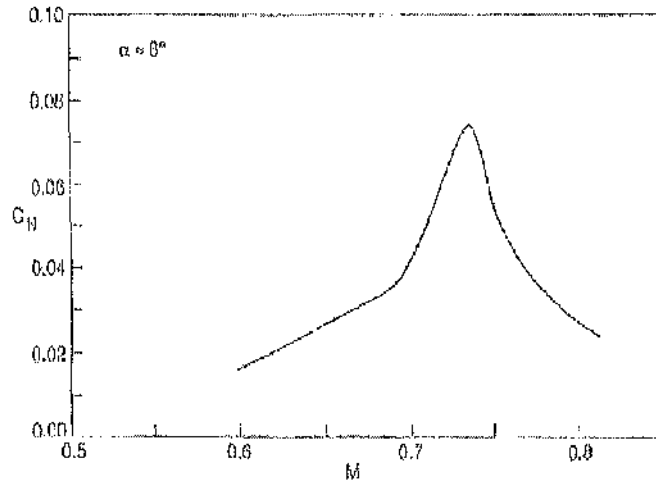


Figure 1.5: Variation of normal force with Mach number at α approximately 6° [36]

which can be modelled and the associated pressure fluctuations predicted. However, aircraft performance is also influenced by the increase of drag and buffeting arising from the separation of a boundary layer from an essentially smoothly-contoured lifting surface. Because of the wide variation of Mach number and angle of attack, flow separation on combat aircraft wings can be expected in certain regions of the flight envelope. In manoeuvring flight a combat aircraft wing exhibits a complex, changing pattern of attached, separated and vortex flows across its span. The management of separated flows and minimization of buffet requires significant design effort.

1.3.2 Types of separation

For the subsonic attached flow past an aerofoil, viscous effects are usually assumed to be confined to a thin layer adjacent to the aerofoil surface and in

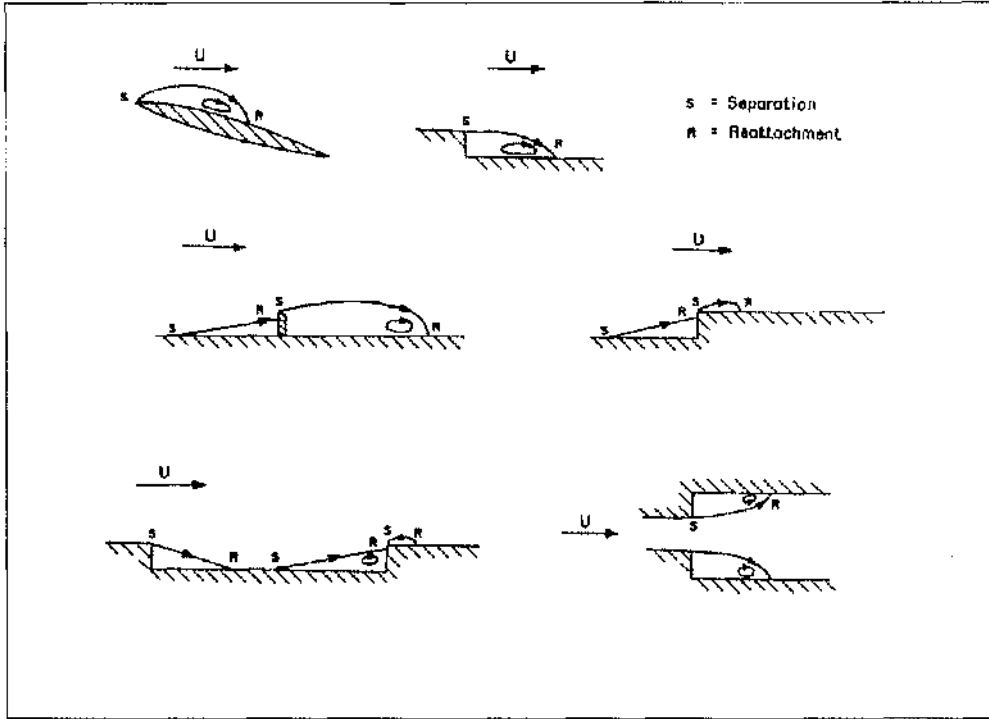


Figure 1.6: Types of bubble flow [61]

the wake. As Mach is increased, a critical value is reached. Above the critical Mach number, a supersonic region appears which is generally terminated by a shock wave. When the pressure rise across the shock reaches a sufficiently large value, shock-induced separation of the boundary layer occurs.

In considering shock-induced boundary layer separation on aerofoils, there is always a region of supersonic/subsonic flow separated by a shock wave. This is followed by the presence of continuous adverse pressure gradient in the subsonic flow downstream of the shock. Development of upper-and lower-surface boundary layers near the trailing edge and their merging into the wake have significant influence on the circulation, and through it the pressure

distribution and shock location.

At low incidences when shock waves occur on both surfaces, the introduction of a disturbance at the foot of the shock will cause a change in the pressure recovery downstream of the shock. The flow at the lower surface is affected which in turn causes the shock to move rearwards. The static pressure along the wake is also disturbed and in order that the pressure may fall to the freestream value to satisfy the compatibility condition, the shock and the separation point on the upper surface must move forward. The compatibility condition is where the static pressure on the two sides of the wake has to be equal, or near equal[60].

Pearcy[60] and Pearcy and Holder[61] studied mostly bubble separation. A sketch of this type of separation found commonly in aerofoils of conventional design is shown in Figure 1.7 where a supersonic region extends along the edge of the bubble downstream of the foot of the shock. This region lies in an area where the pressure increases in the downstream direction causing the streamlines to converge. This offsets the tendency for the shear layer to re-attach and delays the closure of the bubble. On the other hand, a local subsonic flow with diverging streamlines would help to promote re-attachment. As long as the rise near the forward part of the bubble re-establishes subsonic flow, the bubble size would tend to be self-limited.

In addition to the presence of a bubble separation, rear separation tends to occur and spread forward from the trailing edge for thick supercritical aerofoils. The onset and rate of forward movement depends mainly on the thickness and velocity profiles of the boundary layer approaching the trailing edge as well as local pressure gradient. Complicated interactions between

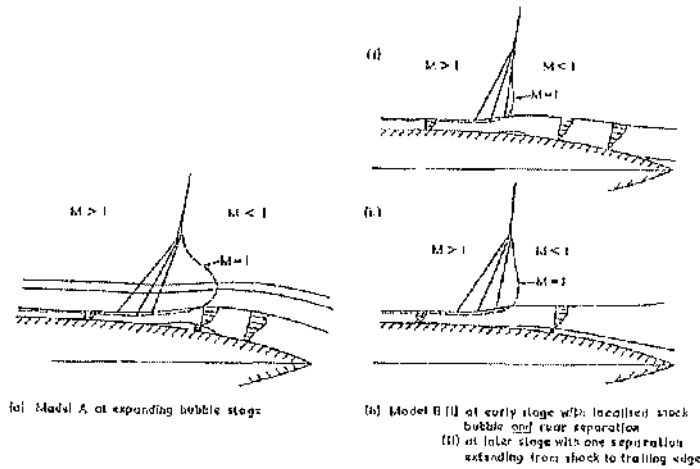


Figure 1.7: Sketch illustrating shock boundary layer interaction: (a) bubble separation, (b) bubble and rear separation [61]

rear and bubble separation can occur. If the boundary is already on the verge of separating near the trailing edge when a bubble separation occurs further forward, this bubble will likely disturb the boundary layer profile sufficiently to trigger rear separation. Pearcy et al [61] named this flow separation as model B to distinguish from the bubble separation which is model A (see Figure 1.7).

As stated earlier, the nature of flow separation is complex. Figure 1.8 illustrates several different characteristics encountered in the flow over the upper surface of the aerofoil as incidence is increased for a range of subsonic speeds [60]. In producing high maximum lift at low speed a strong adverse pressure gradient is generated well forward on the section which can separate the boundary layer (possibly still laminar) as a bubble close to the leading edge. The bubble itself is a source of buffet and circumstances can cause a sudden

expansion of the bubble, creating a wide unsteady wake, a rapid increase of buffet (Cases 1 and 2 in Figure 1.8). In practice excessively high suction on the leading edge could be relieved by introducing camber. In that case, the initial buffet would arise from the growth of separation spreading forward from the aerofoil trailing edge (Case 3).

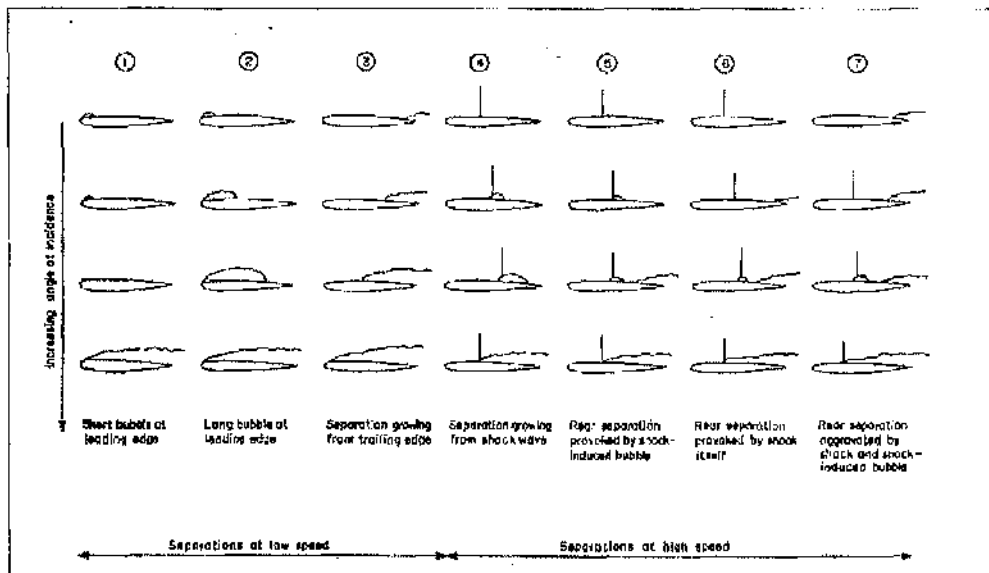


Figure 1.8: Possible types of flow separation on aerofoils [60]

In general at higher speed (Cases 4 to 7) as discussed earlier, a region of supersonic flow will develop on the upper surface of the aerofoil, terminated by a shock. With increasing incidence and/or Mach number the shock wave moves rearwards until the pressure rise through the shock is sufficient to cause the boundary layer to separate at the foot of the shock. Initially, this shock induced separation will form a closed bubble with a re-attachment a short distance downstream from the shock wave. At this stage there may be no trailing edge separation (Case 4); or a trailing-edge separation may be

present prior to the shock-induced separation onset fluctuations.

1.3.3 Shock wave location

The factors that affect the shock wave location are the incidence, freestream Mach number and the aerofoil configuration.

Increasing incidence

With the freestream Mach number held constant, an increase in incidence increases the local Mach number at fixed points upstream of the shock wave. For a small bubble at the shock, the disturbance dies out before reaching the trailing edge where the pressure is practically unaffected by the change in incidence. As the bubble grows in size, it will affect the trailing edge pressure causing divergence when the separation bubble reaches the trailing edge. A further increase in incidence results in a greater decrease in the trailing edge pressure and a stronger disturbance at the wake. Pearcy [60] showed that for a 6% thick RAE 104 aerofoil at Mach numbers between 0.7 and 0.95, the shock initially moves downstream with incidence until a value is reached where any further increase will cause the shock to move forward.

Increasing Mach number

The behaviour in the shock position with increasing Mach number is quite similar to that for increasing incidence. In this case, the freestream pressure falls as the Mach number increases, and the separation becomes more severe due to the stronger local Mach number ahead of the shock wave. The

aerofoil shape determines the local Mach number ahead of the shock and hence controls the onset of separation as well as the rate at which the shock moves over the surface [36]. As Mach number increases the shock usually tends to move rearward. However, for thick aerofoil sections such as those found in supercritical aerofoil design, a forward moving shock may occur for sufficiently high freestream Mach numbers.

1.4 Experimental work on aerofoil buffet

1.4.1 18% thick circular arc

Levy [46] has conducted extensive experiments on the 18% thick circular arc aerofoil to investigate its buffet properties. This aerofoil is characterised by a constant radius of curvature. The experiments were conducted in the NASA Ames high Reynolds number wind tunnel. This wind tunnel is designed for operation at Reynolds numbers per foot up to 40×10^6 for subsonic flows and to 200×10^6 for supersonic flows. To eliminate upper and lower wall interference effects, and to prevent choking of the tunnel, these walls were contoured to follow the aerofoil free-air streamlines for the chosen test condition.

The test data included surface-pressure measurements on the aerofoil and channel walls, oil-film studies to display surface streamlines and locate lines of flow separation and flow field shadowgraphs. The tests were conducted at freestream Reynolds numbers, based on aerofoil chord length, ranging from 1×10^6 to 17×10^6 . The test Mach number was varied from near the critical value ($M=0.71$) to the highest possible without choking the channel. Pres-

sure measurements were made along the centerline on both upper and lower aerofoil surfaces and at spanwise stations on one surface. The results indicated two-dimensional flow over most of the aerofoil.

During the course of the investigation it was discovered (from viewing high-speed shadowgraph movies of the flow field) that unsteady oscillatory occurred for certain combinations of Reynolds numbers and Mach numbers. To provide detailed information in this unsteady flow regime, four miniature pressure sensors were located directly in the aerofoil.

A shadowgraph of the flow field taken through the test section windows at $M=0.79$ and $Re=11 \times 10^6$ is shown in Figure 1.9. At these test conditions shock-induced separation occurs near the foot of the shock wave and extend downstream beyond the shock wave and Mach waves appears to emanate from the interface between the turbulent shear layer and the outer flow. Superimposed on the shadowgraph are mean axial velocity profile data obtained with a laser velocimeter.

The values of the surface pressure and skin friction were also investigated by Levy [46], see Figure 1.10. The data show a small pressure recovery aft of the shock-induced separation point. The magnitude of the pressure coefficient downstream of the separation is slightly lower than the critical pressure and the flow may be slightly supersonic. This interpretation is consistent with the shadowgraph observation (Figure 1.9) which revealed an oblique shock near the separation point.

A portion of the experimental surface pressure time histories taken during a Mach number sweep through the unsteady flow region for two positions on the aerofoil are shown in Figure 1.11. Examination of these data shows

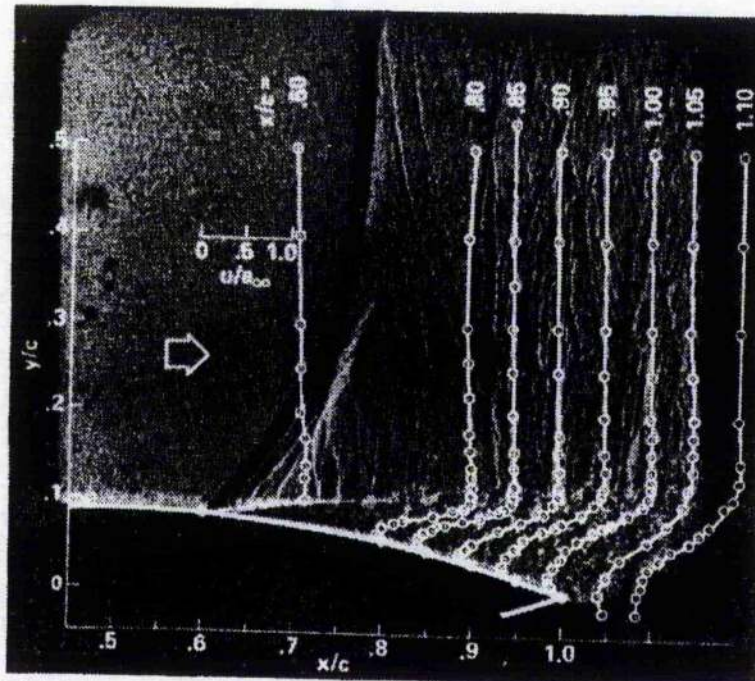


Figure 1.9: Shadowgraph of steady shock-induced separation with an overlay showing mean velocity profiles, $M=0.79$ and $Re=11$ million [46]

that the unsteady pressure are periodic and that the pressures on the upper and lower surfaces are 180° out of phase. The frequency of oscillation was found to be independent of the position with a value of 188 Hz. A series of weak shock waves form near the trailing edge where they build strength and coalesce into a single wave that moves toward the midchord. As the shock approaches the midchord it weakens appreciably and the cycle repeats itself periodically. A similar situation occurs in the lower surface 180° out of phase.

A vortex is seen to form near the trailing edge and sheds alternately

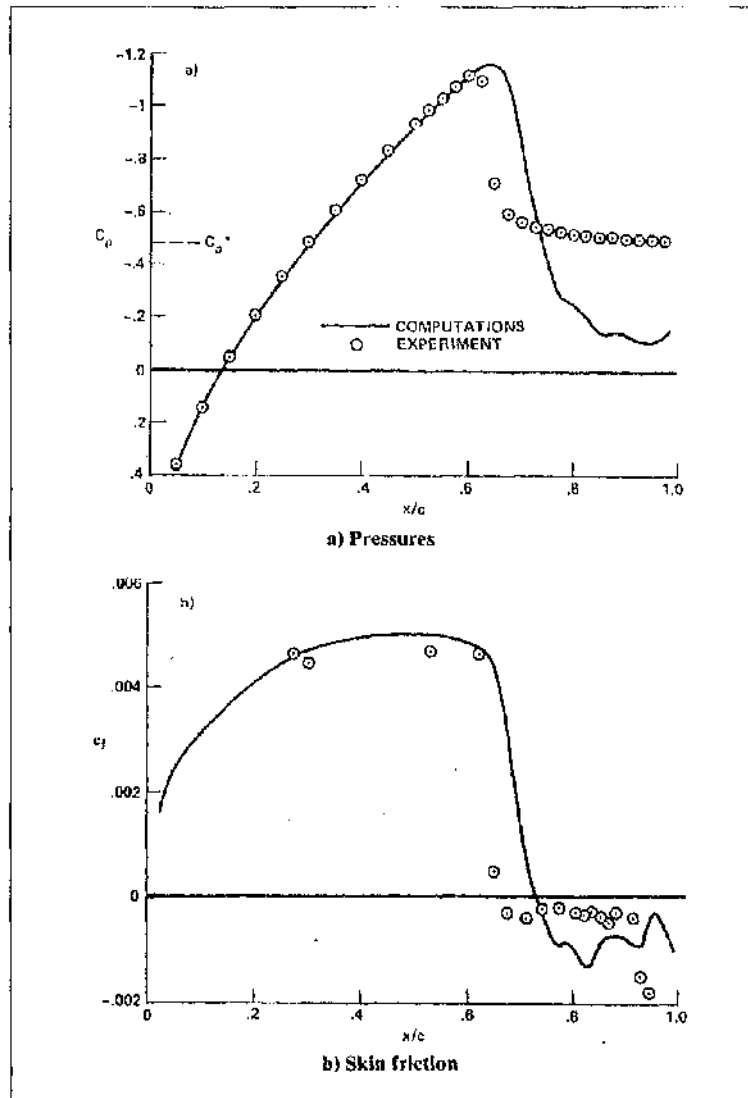


Figure 1.10: Experimental and computed pressures and skin friction on the aerofoil surface, $M=0.79$ and $Re=11$ million [46]

upwards and downwards, depending on the direction of the asymmetry of the periodic flow.

Levy [46] used laser velocimetry to determine the velocity field during

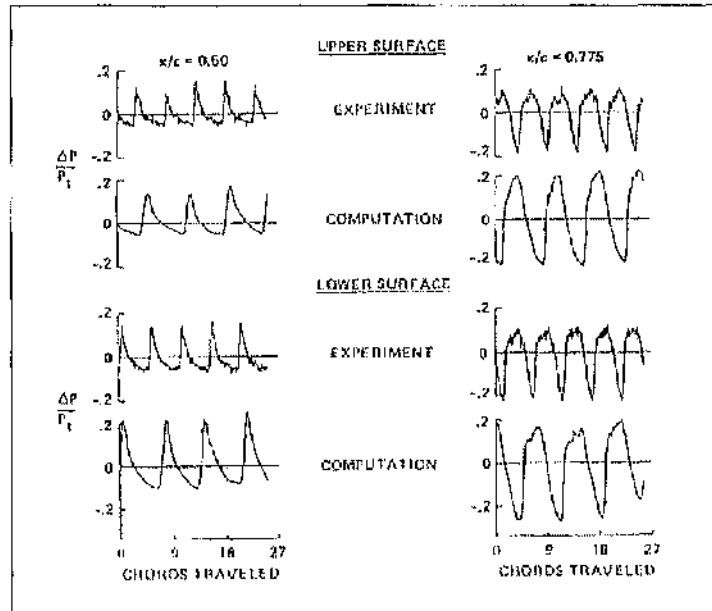


Figure 1.11: Surface pressure time histories on the aerofoil with unsteady flow, $M=0.76$ and $Re=11$ million [46]

the flow oscillations. Instantaneous velocity components were recorded and plotted against dimensionless fraction of time for one cycle of the oscillation, Figure 1.12. The velocity increases with time initially and then shows a marked decrease as the shock wave passes upstream. Examination of the velocity field data and the shadowgraphs revealed a complete picture of the flow field. As the shock wave begins to form near the rear of the aerofoil, it strengthens and moves upstream. Separation occurs at the foot of the shock with subsequent re-attachment on the aerofoil surface. Downstream at the trailing edge a small vortex is formed and circulation occurs from the aerofoil surface with attached flow, around the trailing edge to the surface with shock separated flow.

Levy observed both trailing edge separation as well as separation at the

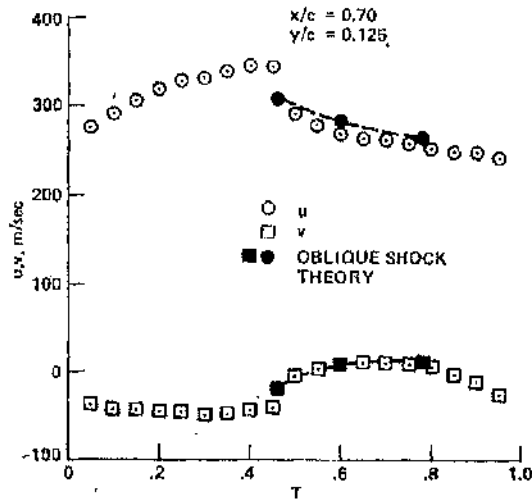


Figure 1.12: Time history of mean velocity components from conditionally sampled data for one cycle of flow oscillation, $M=0.76$ and $Re=11$ million; $x/c=0.7$ and $y/c=0.125$ [46]

foot of the shock. At $M=0.75$ the pressure recovery over the aft portion of the aerofoil is weak and the shock-induced separation occurs. The flow field is directly affected by the displacement effect of the boundary layer and the effect of changes in Reynolds number on peak pressure coefficient, shock strength, shock location, and aft pressure recovery are appreciable, particularly at low Reynolds numbers. In general, the Reynolds number effect is small for numbers above 10 million.

Levy also concluded that as test Mach number is increased above the critical value ($M=0.71$), steady flow with strong aft pressure recovery, and with boundary layer separation located near the trailing edge ($x/c=0.9$), persists for the test Reynolds number range (1×10^6 to 17×10^6) until approximately $M=0.76$. As the freestream Mach number is increased from about 0.76 to

0.78, the flow is unsteady. About $M=0.78$ the flow is again steady (except for the lowest Reynolds number of 1 million), with separation now fixed at the base of the shock wave.

McDevitt et al [52] also conducted tests on an 18% thick circular-arc aerofoil at Reynolds number between 1 and 17×10^6 . By varying the peak Mach number just ahead of the shock from about 1 to 1.4, weak and strong shock boundary layer interactions were observed. Unsteady pressure measurements were taken at $x/c=0.5$ and 0.775, and these measurements show periodic motion of the flow to be asymmetric and the shock movement on the upper and lower surfaces is exactly 180° out of phase. This is consistent with the results obtained by Levy. Shadowgraph movies were taken of the flow over the aft portion of the aerofoil as Mach number was varied from 0.74 to 0.785 at a rate $dM/dt=0.001$, and the results show that on the aerofoil surfaces, alternate shock-induced and trailing edge separation occur.

McDevitt suggested that during a particular phase of the oscillation cycle when the peak in pressure is ahead of the shock on the upper surface is above the the critical value, shock-induced separation will occur. The shock on the lower surface, being closer to the trailing edge, will induced rear separation. The effective aerofoil profile is no longer symmetrical and the effect of the negative camber is to slow down the flow over the upper surface. This tends to suppress the shock-induced separation phenomenon but at the same time induces higher velocities over the lower surface, and the flow fields reverse. When the freestream Mach number is increased to a value sufficiently above the critical, the oscillatory behaviour ceases and both surfaces experience steady, shock-induced separation.

Figure 1.13 shows the regions where periodic shock oscillations occur for increasing and decreasing Mach number at a rate of $dM/dt = \pm 0.001$. This figure was documented by McDevitt after further works on the circular-arc aerofoil. The right-hand boundaries are essentially the same but the left-hand boundaries are consistently different. The first appearance of the shock-induced separation on the onset of periodic flow occurs at peak Mach number ahead of the shock to be approximately 1.25.

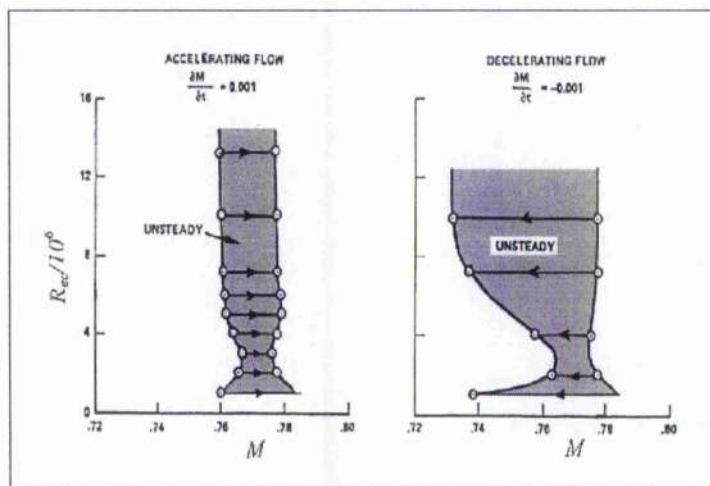


Figure 1.13: Unsteady flow domain [52]

1.4.2 12% thick NACA 16 series aerofoil

Extensive measurements of pressure fluctuations caused by two-dimensional shock/boundary layer interactions on a 12% thick NACA series aerofoil were conducted by Mundell and Mabey[58]. The measurements illustrated some interesting features of shock/boundary layer interactions not well established previously.

A NACA 16 series aerofoil had a thickness/chord ratio of 11.7%, a chord of 152 mm and a span (2b) of 606 mm was used in the experiments. This model was mounted in the RAE 2ft x 1.5ft transonic tunnel. The Mach number range for this investigation was from $M=0.7$ to 0.86 , Reynolds number was relatively low; 1.4 million for $\alpha = 0^\circ$ and 3.6° and 1 million for $\alpha = 6.7^\circ$. Transition was free for $\alpha = 0^\circ$ but fixed for $\alpha = 3.6^\circ$ and 6.7° by roughness bands at $x/c=0.07$ and 0.1 on the upper and lower surfaces respectively. Mabey did a classification of the shock/boundary layer interactions from results obtained in these experiments. This is illustrated in Figure 1.14 for constant Mach numbers as the angle of incidence increases. Type 1 indicates the weak shock with a turbulent boundary layer. In the time-mean flow the main effect of the shock is to thicken the turbulent boundary layer. The three regions of excitation may be identified:

1. upstream of the shock, a low level rms pressure at all frequencies.
2. close to the shock a low level, low frequency, small scale excitation, and
3. a short distance downstream of the shock, the pressure fluctuations revert to the tunnel-empty level. The low frequency excitation close to the shock could be integrated to give a small net force at low frequencies. However this force would be masked generally by the net force due to unsteadiness in most transonic tunnels.

Type 2 is a complicated interaction of a shock sufficiently strong to separate the turbulent boundary layer locally, this separation being followed by

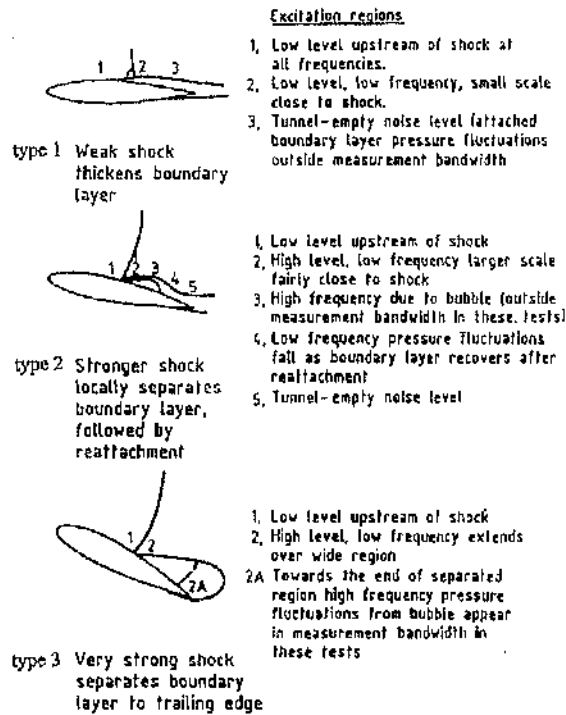


Figure 1.14: Classification of shock/boundary layer interactions and excitation on the aerofoil [58]

re-attachment. In the time-mean flow the main effect is a rapid increase in the boundary thickness at the trailing edge, and the divergence of the trailing edge pressure. Five regions of excitations may be identified:

1. upstream of the shock there is a low level rms pressure. Quite similar to type 1.
2. fairly close to the shock a high level, low frequency large scale excitation,
3. along the bubble the low frequency excitation due to the shock atten-

uates and the high frequency excitation due to the bubble increases.

4. as the boundary layer recovers downstream of the re-attachment the low frequency excitation falls rapidly, and
5. towards the trailing edge the excitation due to the shock reverts to the tunnel-empty level.

Type 3 is the final stage of the shock induced separation. The strong shock now separates the turbulent boundary layer and this does not re-attach to the aerofoil. In the time-mean flow the main change is the thick separated shear layer at the trailing edge. Three regions of excitation may be identified:

1. upstream of the shock there is low level rms pressure,
2. downstream of the shock a high level, low frequency large scale excitation extends from over the wide separated flow region, and
3. towards the end of this separated flow region, some high frequency excitation from the bubble, formed by the closure of the wake appears.

However, the results from these experiments were greatly influenced by the wall effects from the tunnel. When the shock from the model intersects the boundary layer on the roof of the tunnel, shock disturbances can propagate upstream through the subsonic portion of the plenum chamber of a slotted tunnel.

Mabey also kept the angle of incidence constant at 3.6° while the Mach number was varied. A weak shock with attached flow was observed for $M=0.74$. The steady pressure distribution shows that close to the leading edge there

is a small region of supersonic, terminated by a weak double shock. The rms pressure fluctuations have a maximum at the shock (upstream of the measurement position for this condition) and then decrease steadily as x/c increases, reaching the tunnel level.

The Mach number was increased to $M=0.8$, at this Mach number the shock was sufficiently strong to cause separation which is followed by re-attachment. The Schlieren images showed that the shock now oscillates about a mean position. The average Mach number at the shock derived from the mean pressure distribution is only 1.18 and it is therefore not surprising that attached flow is predicted for this condition. The rms pressure fluctuations have two maxima, the first in the vicinity of the shock and the second in the vicinity of the re-attachment point. Downstream of the re-attachment the rms pressure fluctuations fall rapidly towards the tunnel level. The spectra of the pressure showed some interesting features. For $x/c=0.45$, upstream of the mean shock position, there is peak at very low frequency. This is caused probably by the intermittent separation associated with shock oscillations. In the vicinity of the shock ($x/c=0.5$ and 0.55) this low frequency peak is present, together with higher peak characteristics of shock-induced separation with turbulent boundary layers.

When the Mach number was increased to 0.82 a shock-induced separation without re-attachment was noticed. The shock was sufficiently strong to provoke separation without re-attachment. Steady pressure distribution gives no indication of a bubble, and oil flow photographs showed that separation extends from the shock to the trailing edge. The average Mach number at the shock has increased to 1.25. The rms fluctuations are extremely low up-

stream of the shock, have a maximum in the vicinity of the shock and then fall rapidly. Between $x/c=0.7$ and 1.00 other experiments by Lee [39] suggested that the pressure fluctuations should increase steadily as the separation bubble increases in depth towards the trailing edge. The spectra of the pressure fluctuations show that the level of excitation is extremely low upstream of the shock. At the shock the excitation is dominated by the peak characteristic of the shock boundary layer interaction. The tunnel Schlieren system shows that the amplitude of the shock oscillation is larger at $M=0.82$ than at $M=0.80$. At $M=0.84$, measurements showed a shock sufficiently strong to extend to the roof of the tunnel, as well as to provoke shock-induced separation without re-attachment. The steady pressure distribution resembles closely that at $M=0.82$ but now the shock is a little further downstream (although weaker) and the separation is not two-dimensional in the vicinity of the trailing edge. The rms pressure fluctuations are low up to the shock, have an exceptionally high maximum at the shock (about $p/q=0.08$) and then fall rapidly to $p/q=0.02$ at $x/c=0.7$, where q is the dynamic pressure. The spectra of the pressure fluctuations are particularly interesting. At the shock the level of pressure fluctuations is about three times higher than at $M=0.82$, although the shock in time-averaged flow is a little weaker. This large increase in pressure fluctuations is due probably to the propagation of disturbances from the boundary layer of the tunnel.

1.4.3 14% Thick Biconvex Wing

Mabey [48] conducted experiments on the 14% thick biconvex aerofoil section. The tests were made on small models ($c=300\text{mm}$). Periodic flow occurred with both laminar and turbulent shock wave boundary layer interactions. The flow involves the periodic movement of the shocks between the trailing-edge and the maximum thickness position on alternative sides of the aerofoil (as sketched in Figure 1.15) and generates large unsteady pitching moments. The model was tested over the Mach number range from the criti-

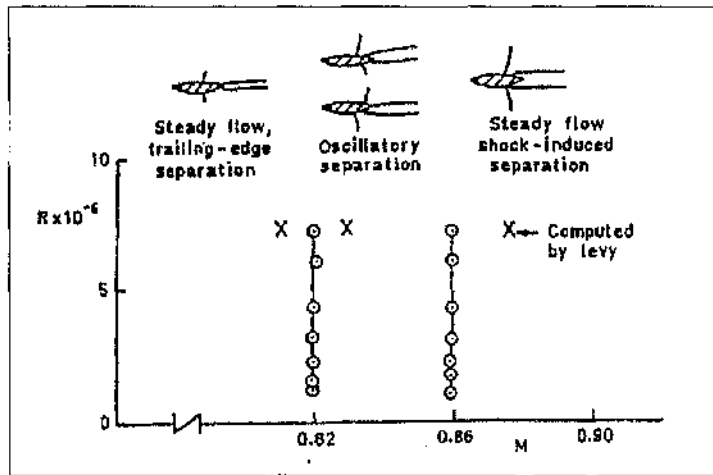


Figure 1.15: Flow domains for a 14% thick biconvex aerofoil $\alpha = 0^\circ$, fixed transition domains [48]

cal value, $M=0.74$ to $M=0.9$ at a total temperature of about 290 K and over the Reynolds number range from $Re=1 \times 10^6$ to 7×10^6 .

Mabey [48] noticed that just below the onset of periodic flow, for a Mach number $M=0.81$, there is a shock between $x/c=0.65$ and 0.7. This shock does not cause significant flow separation because the trailing-edge pressure does not diverge. However high speed shadowgraph pictures show a small area

of separation at $x/c=0.87$, well downstream of the shock. With an increase in Mach number to $M=0.85$, in the region of the periodic flow shows that the mean shock weakens a little and moves forward to about $x/c=0.6$. High speed shadowgraph pictures show that there is no steady shock position. Instead a periodic motion develops, with shock moving upstream from about $x/c=0.75$ to 0.55 , alternating between the upper and lower surfaces (ie the shocks move in anti-phase). The mean separation position of $x/c=0.83$ was observed by surface oil flow test at $Re=2 \times 10^6$.

With an increase in Mach number to $M=0.88$, just above the region of periodic flow, the mean shock position moves back to between $x/c=0.65$ and 0.70 . The small Mach number gradient behind the shock indicates that the flow is completely separated from the shock to the trailing edge.

Mabey also observed that the steady pressures indicate no unusual features in the transonic flow. The classic Mach number freeze develops upstream of the shock, and trailing edge pressure divergence clearly indicates the onset of significant flow separation. For the critical Mach number, $M=0.74$, the pressure fluctuations are nearly symmetric about the midchord of the wing, with a maximum of $p/q=0.04$. This peak is attributed primarily to the influence of wake fluctuations and flow unsteadiness on the development of the region of the sonic flow about maximum thickness.

When the Mach number increases to $M=0.81$ a small peak ($p/q=0.04$) develops near the shock. Upstream of the shock the pressure fluctuations are at a common, low level of $p/q=0.01$, because the shock partially inhibits forward movement of disturbances from the trailing edge or the diffuser of the wind tunnel. In contrast, downstream of the shock the pressure fluctuations are

at a higher common level of $p/q=0.02$ because disturbances can propagate upstream into this region from the wake and diffuser.

When the Mach number increases to $M=0.85$ there is a radical change. Over the region where the upstream shock motion occurs (from $x/c=0.75$ to 0.55) the pressure fluctuations increase substantially, peaking at $p/q=0.34$. These pressure fluctuations are an inevitable result of rapid periodic changes from supersonic to subsonic flow. Upstream of the shock, at $x/c=0.5$ the flow is always attached, but the pressure fluctuations are at the relatively high level of $p/q=0.02$ with an additional increase close to the leading edge. Forward of the shock, weak pressure wave propagate obliquely over the top of the shock as the region of supersonic flow collapses.

When the Mach number is increased to $M=0.88$ the periodic flow is suppressed and the mean shock position starts to move downstream again. The pressure fluctuations peak at the shock with $p/q=0.1$. Upstream of the shock the pressure fluctuations are around 0.03 , consistent with the low level of pressure fluctuations known to propagate downstream from the settling chamber of the RAE 3ft tunnel. Downstream of the shock the pressure fluctuations are random in character, with p/q about 0.03 . Thus these pressure fluctuation measurements for $M=0.88$ are fairly typical of the normal excitation encountered at transonic speeds. The high speed shadowgraph pictures show that the shock waves remain at about $x/c=0.67$ on both surfaces, but alternate in height, and presumably in strength, between the top and bottom surfaces. The large pressure fluctuations are developed by the periodic flow because of the large chordwise movements of the shocks on opposite surfaces of the wing. Shadowgraph pictures suggested that the shock moves forward

from $x/c=0.78$ to 0.55 and remains stationary there for about half a period, gradually becoming weaker until the flow suddenly reattaches and the shock disappears.

1.4.4 CAST 7/DOA1

Stanewsky carried out experimental investigation on a supercritical aerofoil CAST 7/DOA1 to determine the effects of Mach number, angle of attack and Reynolds number on the buffet phenomena and especially the effects on shock oscillation frequency and amplitude [79].

It is vital that the effects of Reynolds number on the flow development is known when developing a transonic aerofoil. The state and condition of the boundary layer upstream of the upper surface plays an important part in the development of shock waves and regions of separation. The aerofoil model has a chord length of 100 mm. The experimental setup is shown in Figure 1.16. Surface pressure orifices were installed to measure and to determine the average pressure distribution, surface flush-mounted dynamic pressure transducers recorded the pressure fluctuations at various chord locations and surface hot-film sensors mainly to detect transition and separation locations. Density distributions in the unsteady flow field and flow visualization were obtained by a holographic high-speed, real-time interferometer.

Figure 1.17 shows the surface time-averaged pressure distribution at a constant Mach number of $M=0.775$ and Reynolds number of $Re = 8 \times 10^6$, with increasing angle of attack going from a pre-buffet state to a condition beyond buffet onset. The upper surface pressure distribution is character-

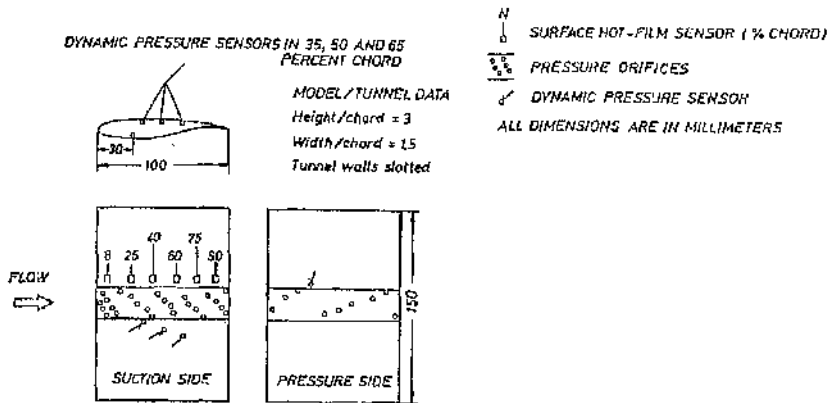


Figure 1.16: The CAST 7/DOA1 model and instrumentation [79]

ized by a strong expansion near the leading edge followed by a plateau-type pressure distribution over the mid-section of the aerofoil and followed by a relatively strong shock wave and fairly large rear adverse pressure gradients making the aerofoil susceptible to trailing edge separation[79]. It can be seen that the shock wave moves upstream with increasing angle of attack and at the same time there is a rapid drop in trailing edge pressure. Decreasing trailing edge pressure indicates a strong thickening of the boundary layer at the trailing edge and it is likely that either separation starts to develop at the trailing edge or the shock-induced separation bubble has reached this position. At an angles of attack of 3° and 4° shock oscillations were observed.

Stanewsky and Basler[79] suggested that the thickening of the boundary layer at the trailing edge and the corresponding drop in the trailing edge pressure are the driving mechanism for the periodic shock motion. Figure 1.18 shows the variation in shock strength represented by the height of the

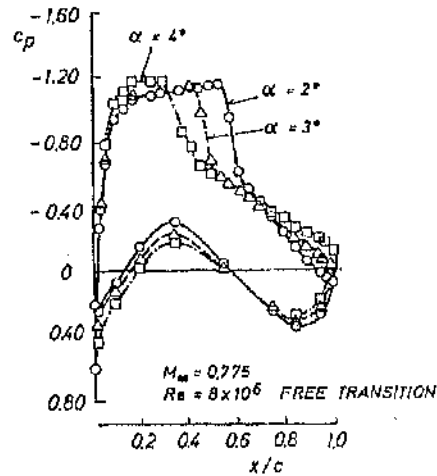


Figure 1.17: Averaged pressure distributions at pre and post-buffet onset conditions [79]

shock wave in a cycle of shock oscillation. It is indicated that during the latter stages in the downstream movement of the shock, the strength of the shock increases, a process that continues during the subsequent forward movement until a certain position on the aerofoil is reached. During the remainder of the forward movement, the shock strength decreases[79]. The bottom plot shows that during the whole process of the upstream movement the boundary layer thickness at the trailing edge increases. It is believed that the thickening of the boundary layer at the trailing edge and the corresponding drop in trailing edge pressure is driving the shock upstream since the shock must adjust its position according to the trailing edge pressure.

The amplitude and frequency of the shock oscillation are likely to be dependent on the Reynolds number or some characteristic boundary layer pa-

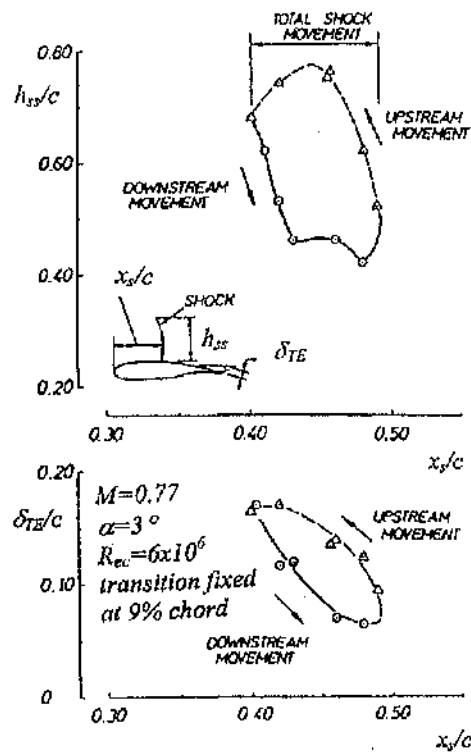


Figure 1.18: Relation between shock movement, shock strength and trailing edge boundary thickness [79]

parameter since this process is closely related to the development of separation. Consider the dependence of the reduced frequency on the Reynolds number for angles of attack well within the buffet domain, Stanewsky observed that the reduced frequency, based on the chord length, generally decreases with Reynolds number, Figure 1.19. This holds for the two angles of attack considered, $\alpha = 4^\circ$ and 5° , as well as for the three Mach numbers depicted, $M = 0.74, 0.76$ and 0.78 . Note that the shock oscillation frequency increases with Mach number.

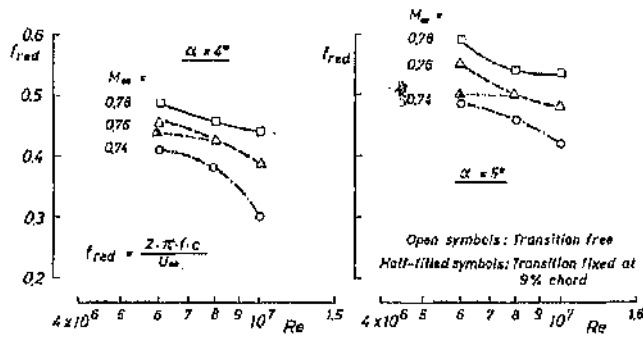


Figure 1.19: Dependence of the reduced shock oscillation frequency on Reynolds number [79]

1.5 Computational work on aerofoil buffet

1.5.1 18% Circular Arc Aerofoil computations by Levy

Computational set-up

Levy[46,50,72] from NASA Ames Research Center has done extensive work on the 18% circular arc using both experimental and computational fluid dynamics for testing and guiding the development of turbulence modelling within regions of separated flows. The transonic flow field about the aerofoil was simulated numerically using a program that utilizes an explicit finite-difference method to solve the time-dependent, two-dimensional, Reynolds averaged form of the Navier-Stokes equations applicable to compressible turbulent flows. The turbulence is modelled using an algebraically expressed eddy viscosity model.

The control volume, -12 and +8 chords in the x direction and ± 6 chords in the y direction, is divided into a 78 x 35 mesh. The flow field development within this volume is followed in time until it attains a steady state. At the far upstream and transverse boundaries, the flow is assumed uniform and at freestream conditions. At the downstream boundary, all gradients in the flow direction are assumed negligible. The aerofoil is assumed impermeable (no-slip boundary condition) and adiabatic, and the pressure gradient normal to the surface is assumed zero.

Results

Experimental pressure distributions and computed results are shown for three sets of freestream conditions, Figure 1.20. The steady flow field at $M=0.720$ is characterized by a weak shock wave and trailing-edge separation. The computed results are in good agreement with experiments over most of the aerofoil. Failure of these results to better predict the pressures in the separated region near the trailing edge is attributed to inadequate turbulence modelling in the region. The steady flow field at $M=0.783$ is characterised by a strong shock wave and shock-induced separation. The computed results are in excellent agreement with experiment ahead of the shock wave. The large differences between the computed and experimental results in the region of the shock wave and aft in the region of shock-induced separation again are attributed to inadequate turbulence modelling. The unsteady flow field at $M=0.754$ is characterised by periodic shock-wave oscillations and boundary layer separation between the trailing-edge and shock-induced separation. The calculated and experimental mean pressures agree well over the forward half of the aerofoil. The similarity in the trends of the variation of the magnitude of the pressure fluctuations about the mean value strongly suggests the possibility that the wave form of the experimental pressure fluctuations also may be reproduced by the calculations. The qualitative agreement between the different wave forms is surprisingly good considering that the computed unsteady results were obtained using a simple algebraic eddy viscosity to model turbulence. The 180° phase difference between the dynamic pressures on the upper and lower aerofoil at identical chord stations demonstrate that

the oscillatory unsteadiness is an asymmetric phenomenon, both in the experiment and in the computations. The reduced frequency of the surface pressure oscillations determined from the numerical solution differs by only 20% from data.

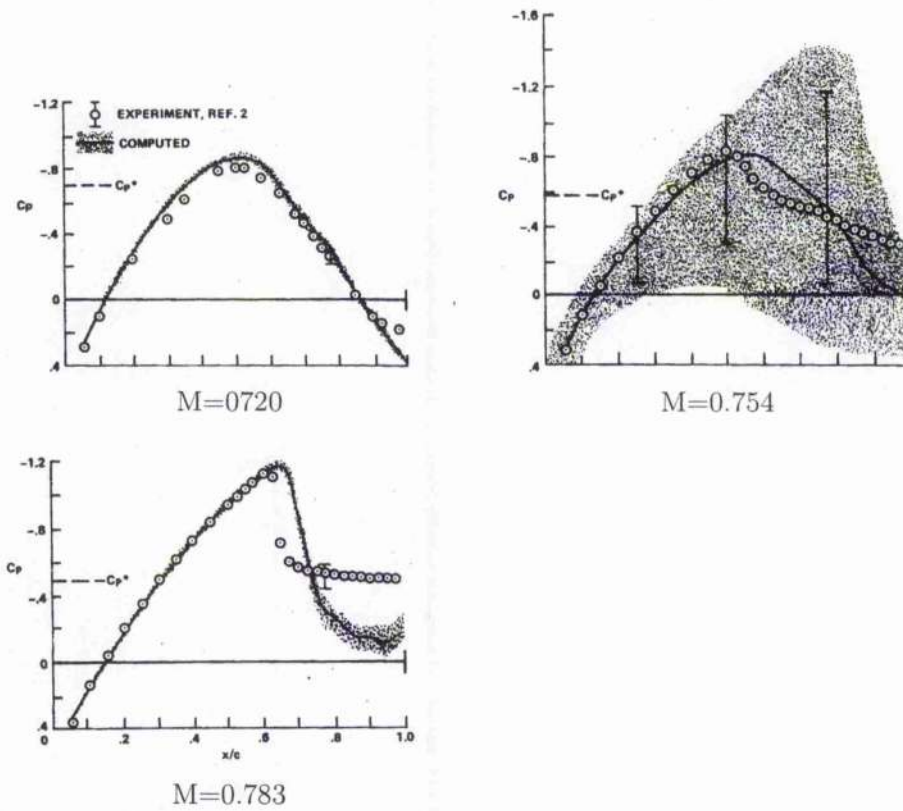


Figure 1.20: Computed and experimental pressure distributions on the circular arc aerofoil, $Re = 11 \times 10^6$ [46].

Computed and experimental skin-friction distribution can be seen in Figure 1.21, as in the case of the pressure distribution the agreement between

the computed and measured values is good ahead of the shock wave. The poor agreement in defining the shock-wave location and aft in the separated flow region is again attributed to deficiencies in the turbulence model.

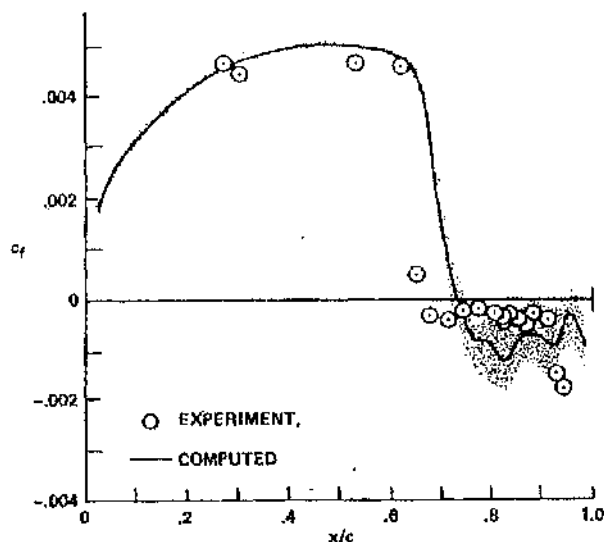


Figure 1.21: Computed and experimental skin-friction distributions on the circular arc aerofoil, $Re = 11$ million, $M = 0.783$ [72]

A comparison of the computation with the velocity and eddy diffusivity deduced from the experiments at two chord-wise locations on the aerofoil is presented in Figure 1.22. The predicted separation height is smaller than that determined experimentally. The maximum eddy diffusivities compare, but their relative position in the boundary layer differ because the computed shear layer is too thin. The main deficiency of the computation is that of underpredicting both the separation region and the outer shear layer thickness relative to the experiment.

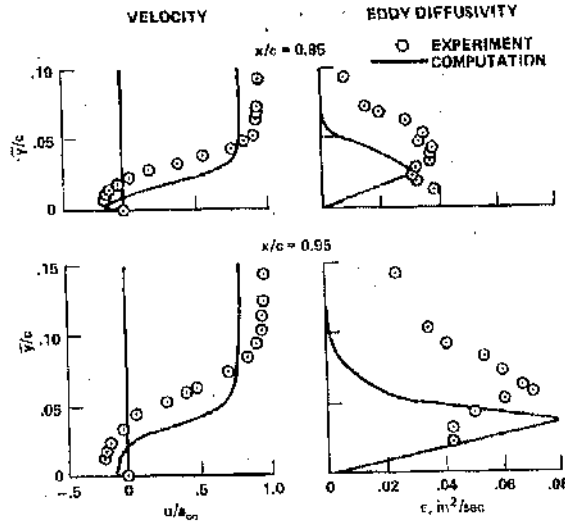


Figure 1.22: Computed and experimental velocity and eddy diffusivity profiles on the circular arc aerofoil, $Re = 11$ million, $M = 0.79$ [46]

1.5.2 NACA0012 Aerofoil computations by Raghunathan

Computational Set-up

A two dimensional thin layer Navier Stokes code capable of computing flows over an aerofoil with a moving grid was used by Raghunathan[63,65] to investigate the mechanism of the origin of shock oscillations on a NACA0012 aerofoil. The code developed for these investigations included heat transfer effects and a moving grid option in order to investigate the effect on periodic flow of a trailing edge splitter plate motion, a flap motion or a pitching aerofoil.

The implicit code solves the mass-weighted thin-layer Navier-Stokes equations using an upwind implicit predictor/corrector cell-centred finite-volume

scheme. A modified version of the simple algebraic Baldwin-Lomax model turbulence model was employed. The minimum normal grid spacing was reduced to 5 milli chords, ensuring a value of y^+ less than 5 everywhere on the aerofoil surface which ensured adequate resolution of the viscous shear layer. Transition to turbulence was fixed on both the upper and lower surface at 3% chord.

Results

The prediction of shock motion on the NACA0012 aerofoil at a Mach number of 0.7, Reynolds number of 10×10^6 and incidence of 6° can be seen in Figure 1.23. This type of periodic motion has also been computed by Edwards[19]. The predictions for both unsteady lift and shock motion agrees favourably with the prediction of Edwards and experimental data available. The non-dimensional frequency predicted by Raghunathan is 0.21 compared with 0.235 by Edwards.

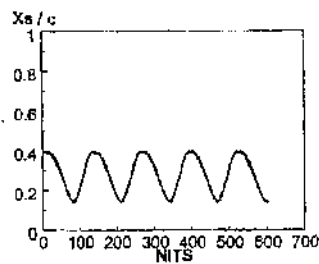


Figure 1.23: Periodic shock motion on the NACA 0012 aerofoil, $M=0.7$, $Re=10$ million and $\alpha = 6^\circ$ [65]

Raghunathan computed the flow field for a Mach number of 0.7, Reynolds number of 10×10^6 and at incidence of 5° . This condition is just outside the periodic regime and solutions for lift converge to a finite limit, Figure 1.24. It was observed from the pressure contours and skin friction values that the boundary layer downstream of the shock is separated.

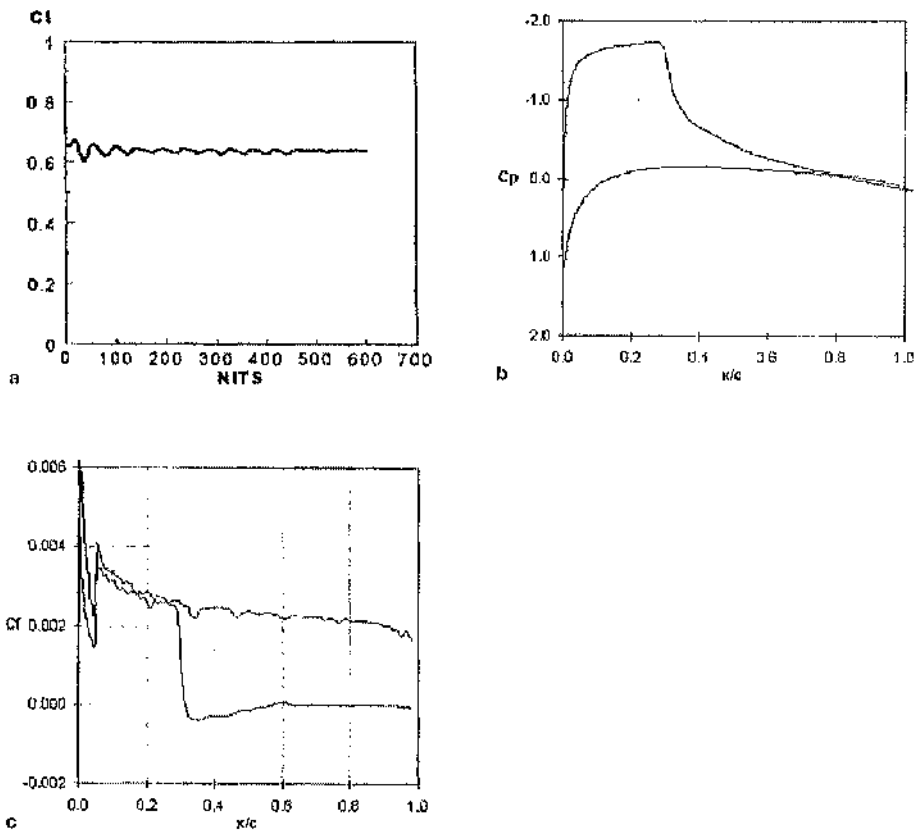


Figure 1.24: NACA0012 airfoil at $M=0.7$, $Re = 10$ million and $\alpha = 5^\circ$ [65].

1.5.3 NACA0012 Aerofoil computations by Barakos and Drikakis

Computational set-up

Computations on the NACA0012 have also been carried out by Barakos and Drikakis[6]. The computations were carried out for the experimental cases of McDevitt and Okuno [54]. Their experiments were performed for the NACA0012 aerofoil at Mach numbers between 0.7 and 0.8, angles of incidence less than 5° and Reynolds number between 1 and 14 million.

The numerical simulations have been carried out using an implicit CFD solver developed for unsteady and turbulent aerodynamic flows. The main feature of the method is the coupling of the turbulence model with the Navier-Stokes equations, via an implicit unfactored scheme and a Riemann solver. The Riemann solver is used in conjunction with a third-order upwind interpolation scheme. This scheme in conjunction with a characteristic-based flux averaging is used to calculate the inviscid fluxes at the cell faces. At each time step the final system of algebraic equations is solved by a point Gauss-Seidel relaxation scheme. According to the present method, the transport equations for turbulence model are solved coupled with the fluid flow equations. The following turbulence models were employed in this investigation: Baldwin and Lomax model, the one-equation model of Spalart and Allmaras, the Launder and Sharma and Nagano and Kim linear $k-\epsilon$ models, as well as the $k-\omega$ version and the non-linear eddy-viscosity model (NLEVM)[6].

Results

The pressure coefficient distributions for $M = 0.775$ and $\alpha = 4^\circ$ using various closures and different grids are compared with the experimental results, see Figure 1.25. For this Mach number and incidence angle, the flow has been found to be steady and all turbulence models predicted steady flow as well. As can be seen, none of the models was able to capture the exact experimental shock position.

Figure 1.26 is a comparison of numerical and experimental results for the buffet onset. There is a well-defined region of Mach number and incidence angle where buffet occurs. Initially, four computations were performed at conditions below the experimentally reported buffet onset and a steady-state solution were achieved (labelled no SIO: no shock-induced oscillation). Afterwards, the incidence angle was slowly increased to obtain unsteadiness and it was found that after the initial peak of the lift coefficient curve the computations resulted either in periodic loads, thus indicating buffet (labelled SIO), or in steady-state flow.

For combinations of Mach number and incidence angle considered here, the linear $k-\epsilon$ models led to a steady solution, thus failing to predict buffet. The computations predict the buffet onset boundary slightly shifted to higher incidence angles and Mach number.

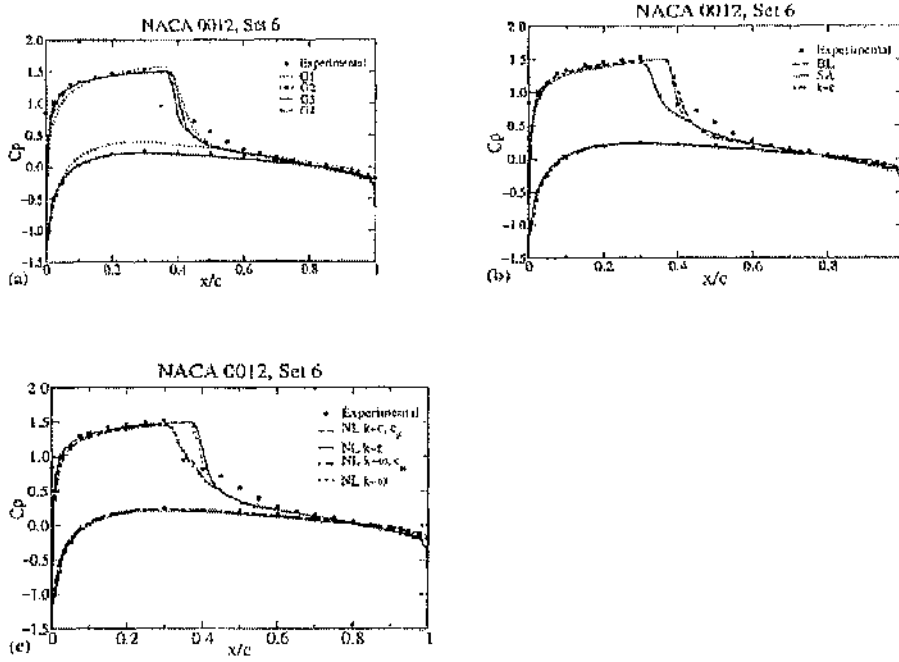


Figure 1.25: Pressure coefficient distribution around the NACA0012 aerofoil:(a)grid size effects, (b)comparisons between linear turbulence models (c)comparison between non-linear turbulence models [6].

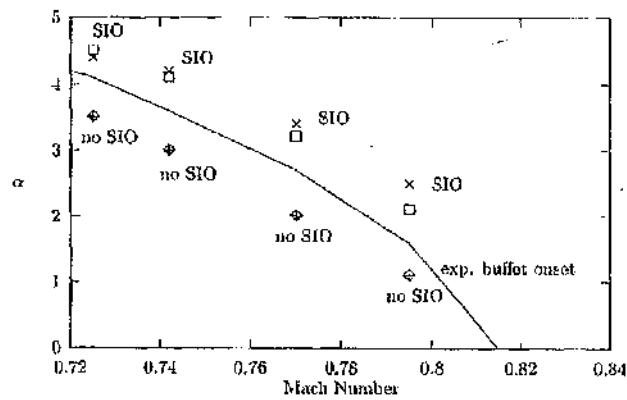


Figure 1.26: Buffet onset for the NACA0012 aerofoil ($Re=10$ million, $M=0.775$, $\alpha=4^\circ$). Solution obtained using the Spalart Allmaras model (crosses) and the non-linear $k-\omega$ model (squares) [6].

Chapter 2

Description of test cases

2.1 Previous work on test cases

2.1.1 Test Case 1 : BGK No.1 Aerofoil

Lee [32,34,36,37] has done extensive work on the BGK No.1 aerofoil. Skin friction and pressures were measured by Lee in some of his experiments to study the characteristics of separated flows. He also considered the fluctuating normal forces of the unsteady loads experienced by the BGK No.1 aerofoil. The BGK No.1 supercritical aerofoil has a design Mach number and lift coefficient of 0.75 and 0.63 respectively. The thickness to chord of the aerofoil is 11.8 %. Figure 2.1 shows a schematic of the aerofoil. There are 50 pressure orifices on the upper surface and 20 on the lower surface for steady pressure measurements. For the unsteady pressure measurements sixteen fast response miniature transducers were used, all positions are shown in Figure 2.2.

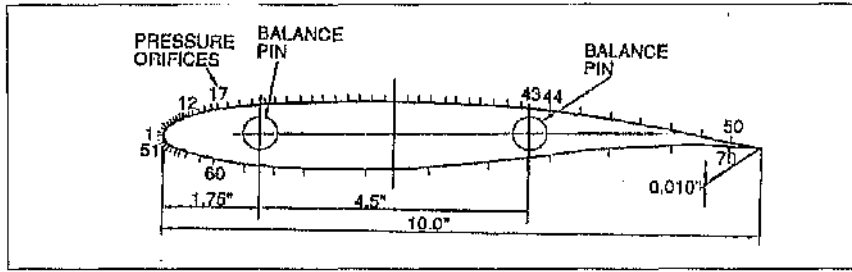


Figure 2.1: Schematic of the BGK No.1 aerofoil showing pressure orifice locations[37]

Lee experimented using several flow conditions, however only the flow conditions of $M=0.71$, and $Re_c = 20 \times 10^6$ will be discussed. Various angles of attack were measured from -0.136° to 6.97° .

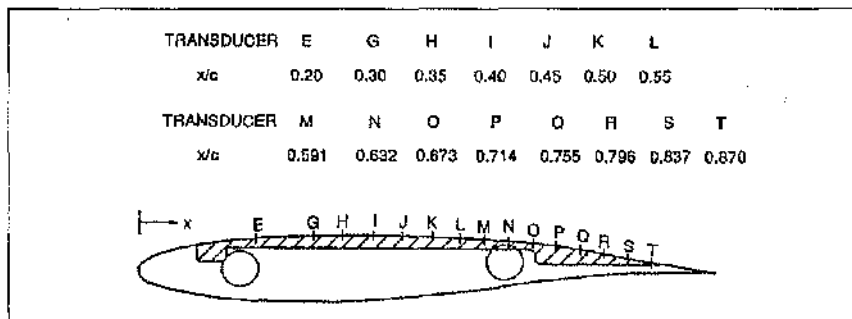


Figure 2.2: Location of the fast response transducers[37]

Lee observed shock/boundary classifications similar to those previously proposed by Mundell and Mabey [58]. The first one was a weak shock which interacts with the turbulent boundary layer resulting in a low level excitation close to the shock. A short distance from the shock, the pressure fluctuations revert to the empty tunnel level. The average surface pressure coefficient, C_p , from these experiments are shown in Figure 2.3. At $\alpha = -0.316^\circ$ the flow on the upper surface was found to be sub-critical. At $\alpha = 1.396^\circ$, a weak shock

is formed and the turbulent boundary layer thickens near the interaction region without separating. Figure 2.4 shows that there is a small increase in the fluctuating pressure intensity, Cp' behind the shock. Increasing to 3.017° results in a large rise in the pressure intensity behind the shock at $x/c=0.4$. The fluctuating pressure is limited to a small region near the shock. For the three values considered so far, the fluctuating pressure intensity at the last measuring position is very close to the tunnel level. This indicates that trailing edge separation has not occurred, or has not reached the position of the last pressure transducer at $x/c=0.87$. Cp' [37] is expressed as:

$$Cp' = \frac{P_{rms}}{q_\infty}$$

At $\alpha = 4.905^\circ$, the steady pressure results show the formation of a stronger shock which caused the flow to separate and reattach to form a bubble. The intensities of the pressure are practically constant in the reattached region, which starts at approximately $x/c = 0.6$ and continues to the last transducer location at $x/c = 0.87$. The pressure intensity plot shows a small hump between $x/c = 0.45$ to $x/c = 0.6$. This hump is usually attributed to a separation bubble.

When α is increased to 6.97° , the flow becomes fully separated. The pressure levels are large behind the shock but decrease rapidly and reach a constant value of about 0.1 from the shock to $x/c = 0.87$. This value of pressure intensity is significantly higher than the tunnel level of 0.004, which is an average value at $M = 0.71$ from α between -0.316° to 6.97° . The ensemble-averaged pressure coefficient, \bar{C}_p time histories are shown for

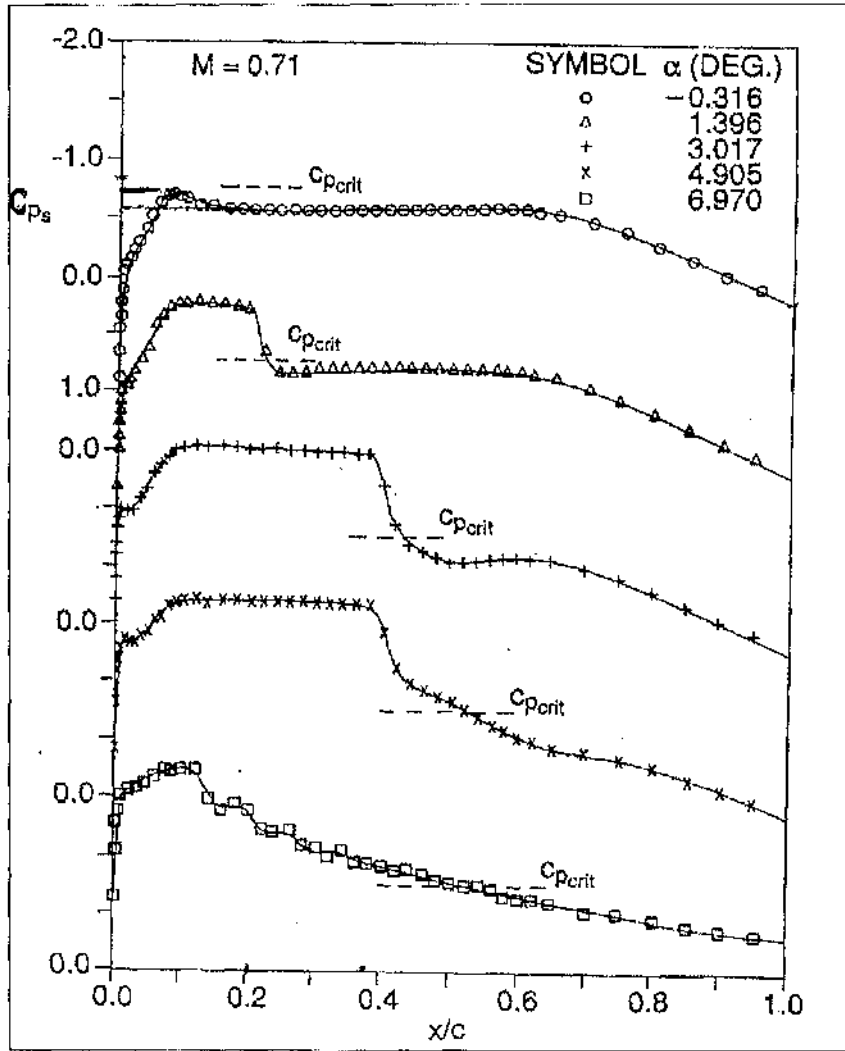


Figure 2.3: Steady pressure distributions on the upper surface of BGK No.1 aerofoil at various α [37]

$M = 0.71$ and several angles of attack in Figure 2.5. The pressure coefficient for the first two values of α indicate lines of constant magnitude. At $\alpha = 3.017^\circ$, small pressure oscillations are observed at transducer I. The pressure field decays rapidly and fluctuations are hardly noticeable at transducer

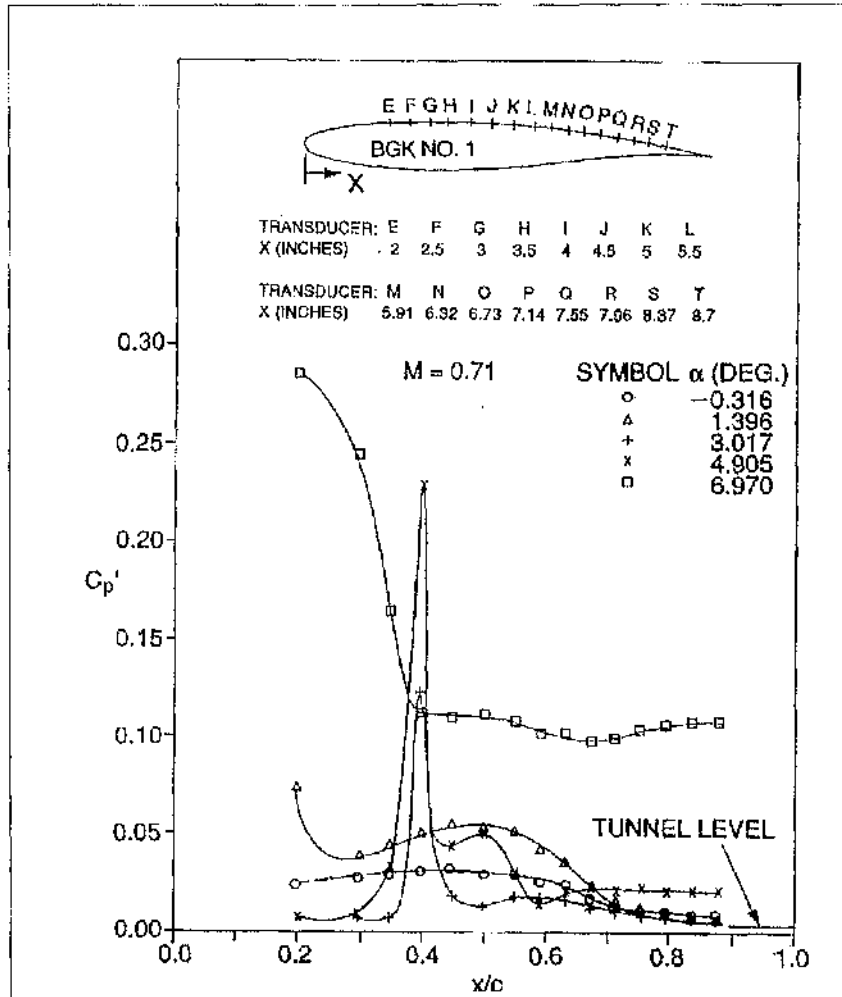


Figure 2.4: Variations of pressure intensities on the upper surface of BGK No.1 aerofoil at various angles of attack [37]

J[36]. As α is increased to 4.905° , large pressure oscillations at transducer I are detected. Pressure fluctuations are quite uniform inside the separation bubble. Pressure fluctuations are quite small downstream of the bubble. The ensemble-averaged pressure coefficient, \bar{C}_p [37] was calculated using:

$$\bar{C}_p = C_{p_s} + \tilde{C}_p$$

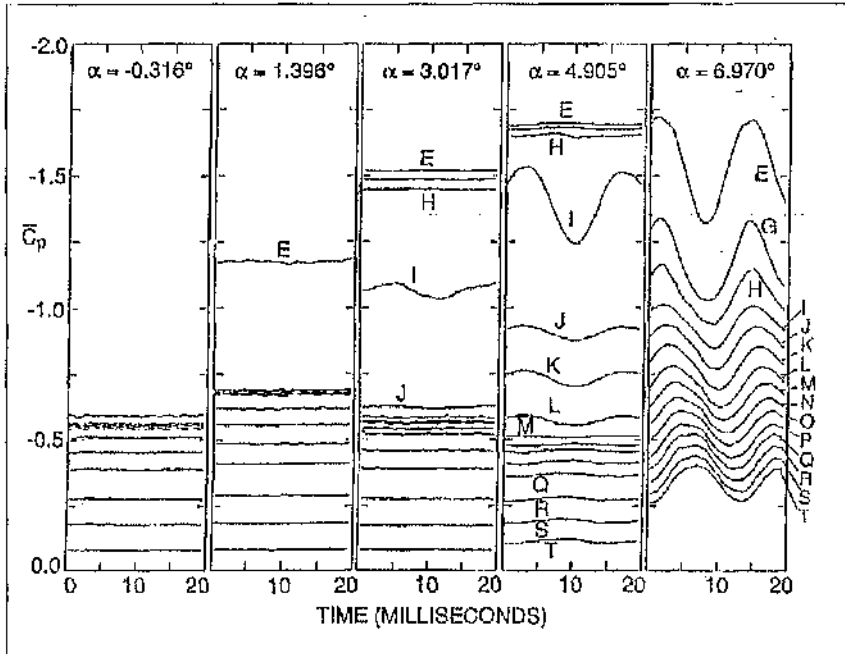


Figure 2.5: Ensemble-averaged pressure coefficient at various angles of attack[37]

2.1.2 Test Case 2 : OAT15A aerofoil

Both experimental and computational work has been conducted on the above aerofoil. Experimental work has been done in the S3 wind tunnel of the ONERA Chalais-Meudon centre. OAT15A is a supercritical aerofoil with a thickness-to-chord ratio of 12.3%, a chord length equal to 230 mm and a thick trailing edge of 0.5% of the chord. Flow conditions were the following: $M = 0.73$, $P_i = 10^5 \text{ bar}$, $T_i = 300 \text{ K}$ and $Re_c = 3 \times 10^6$. Tests were done from

$\alpha=2.5^\circ$ to $\alpha=3.91^\circ$. Computations were conducted using the elsA code developed at ONERA which solves the three dimensional compressible Reynolds Averaged Navier-Stokes equations. It is based on a cell-centred finite volume discretization[12]. Three turbulence models were used to model the buffet phenomenon. The first one is the one transport equation Spalart-Allmaras turbulence model. The second one is the two transport equations $k-\omega/k-\epsilon$ Menter model with SST corrector. The last one is an ASM model. The mesh used in ONERA is shown in Figure 2.6. The total number of nodes used is 65,234. The far-field conditions are imposed 50 times the chord length.

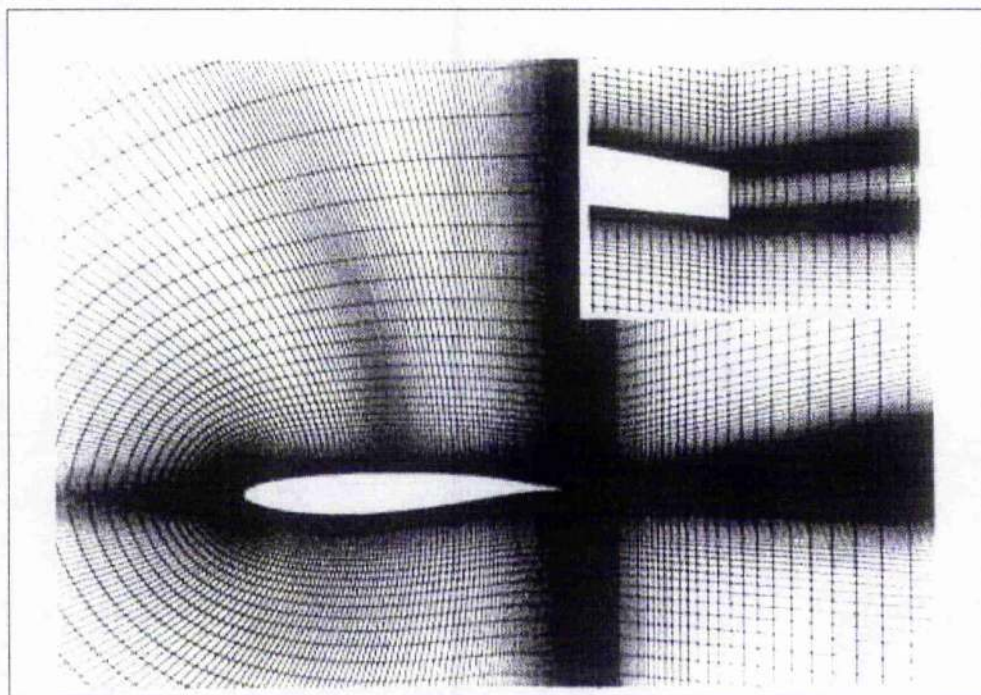


Figure 2.6: Mesh around the OAT15A aerofoil [12]

Figure 2.7 shows the steady pressure distribution at $\alpha = 2.5^\circ$. At this angle of attack, a separated zone exists at the foot of the shock and in the

trailing edge region. Pressure levels are very well predicted on the lower side of the aerofoil, and in the supersonic and the trailing edge regions on the upper side. All turbulence models fail to predict the correct shock position. The Menter SST turbulence model predicts closest the location of the shock in comparison with measurements but pressure levels are much too high at the foot of the shock, showing an under-estimation of the size of the separated area located in this region. The Spalart-Allmaras turbulence model computes the most aft position of the shock[12].

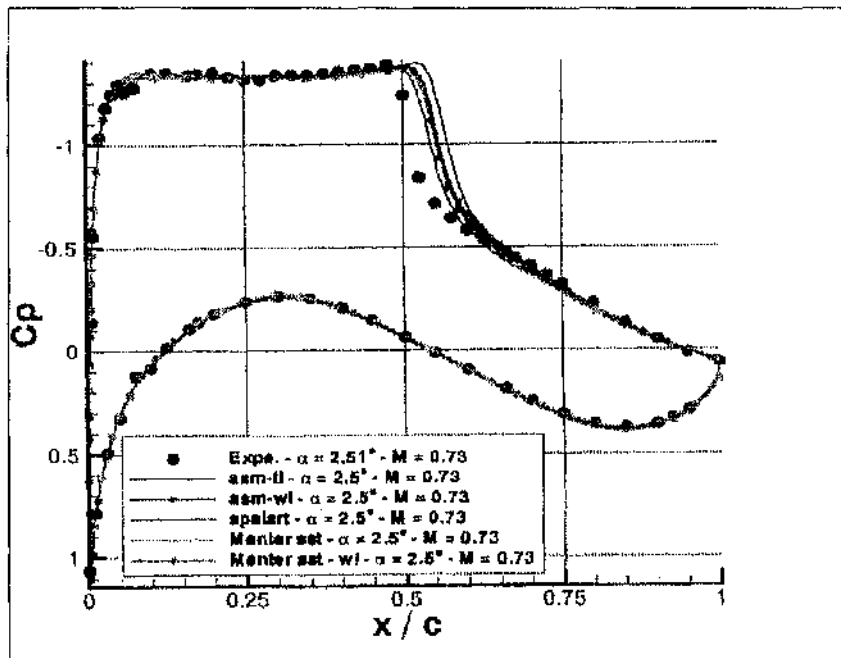


Figure 2.7: Steady pressure distribution at $M=0.73$ and $\alpha = 2.5^\circ$ [12]

In Figure 2.8, the temporal evolution of the shock location is plotted at the angle of attack of 4.5° and 5° . Concerning the ASM model, two angles of attack 4.5° and 5° are presented because the behaviour of this model at 5°

is different in comparison with the other models. At 5° (and higher values), the oscillating movement of the shock is not perfectly sinusoidal because of the different separated areas. On the other hand, at an angle of attack equal to 4.5° (and lower values) the movement is sinusoidal as computed with the other turbulence models. All models predict approximately the same frequency for the buffet phenomenon around 78 Hz and the mean location of the shock is about $x/c=0.4$.

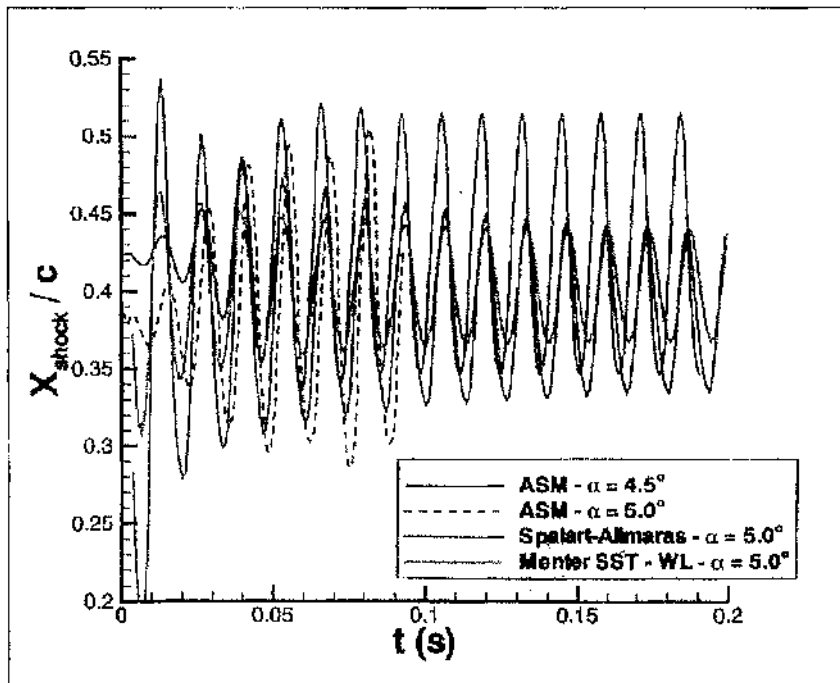


Figure 2.8: Temporal evolution of the shock location [12]

Figure 2.9 represents the mean pressure fluctuations. This figure shows that the computations carried out with the ASM model at the angle of attack equal to 4.5° is in very good agreement with experimental measurements performed at an angle of attack equal to 3.5° . One must note that exper-

iments showed that the buffet phenomenon first appeared at an angle of attack equal to 3.25° and the main frequency of the phenomenon was about 70 Hz whatever the angle of attack.

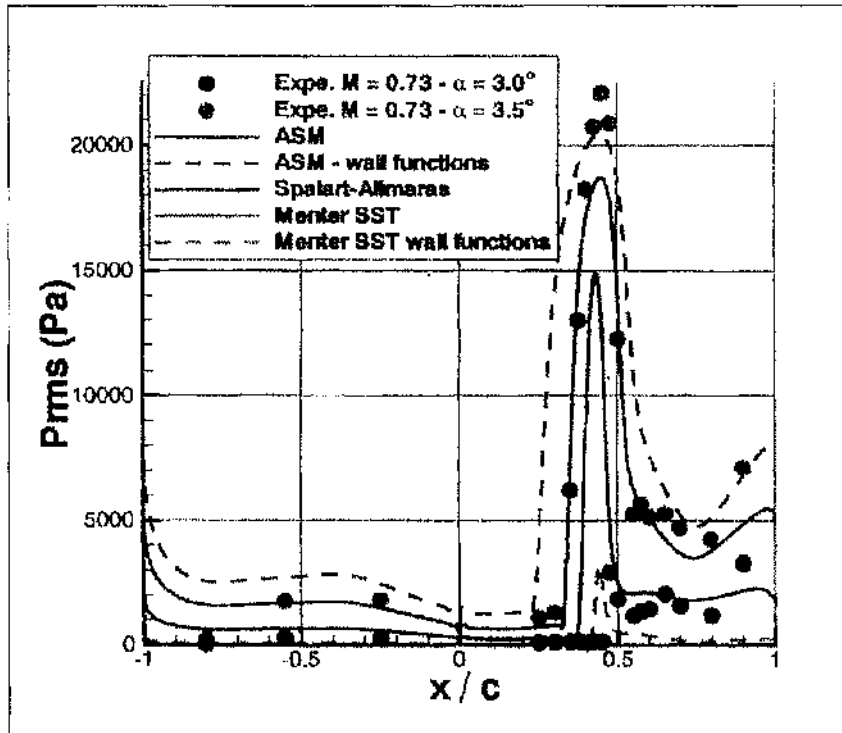


Figure 2.9: Mean pressure fluctuations, computational results at $\alpha = 4.5^\circ$ and experimental results at $\alpha = 3^\circ$ and 3.5° [12]

2.2 Computational set-up for test cases

2.2.1 Test Case 1- BGK No.1 Aerofoil

Computations were performed using the pmb3D code developed at University of Glasgow which solves the three dimensional compressible RANS equations

for multi-domain structured meshes. Further discussion of the code and turbulence models implemented is given in Appendix B. This solver is based on cell-centred finite volume discretization. Several turbulence models can be implemented in the pmb3D solver. The parameters used in the computations are summarised in Table 2.1.

	Steady parameters	Unsteady parameters	Turbulence models
Steady computations	Explicit CFL: 0.4		SST
	Explicit steps: 1000		k- ω
	Implicit CFL: 20		
	Implicit step: 5000		Baseline
	Convergence: 1×10^{-8}		
Unsteady computations	Explicit CFL: 0.4	Final time: 600	k- ω
	Explicit steps: 100	No. of steps: 6000	SST
	Implicit CFL: 20	dt: 0.1	Baseline
	Implicit step: 100	Tolerance: 0.01	
	Convergence: 1×10^{-8}	Pseudo step: 50	

Table 2.1: Numerical parameters used for test case 1

Three grid levels were employed in the computations, a coarse, fine and finer grid, see Figures 2.10, 2.11 and 2.12 respectively. The computational domain was extended from 11 chord lengths upstream to 10 chord lengths

downstream of the leading edge of the aerofoil. Table 2.2 lists details of finite volume grids used. All dimensions have been non-dimensionalized using the aerofoil chord, c .

	Total number of nodes	Minimum and maximum x coordinates	Minimum and maximum y coordinates	Wall distance of the first node
Coarse grid	14, 760	-10/11	-10/10	5×10^{-5}
Fine grid	57, 316	-10/11	-10/10	5×10^{-5}
Finer grid	208, 380	-10/11	-10/10	5×10^{-5}

Table 2.2: Details of the finite volume grids used for test case 1

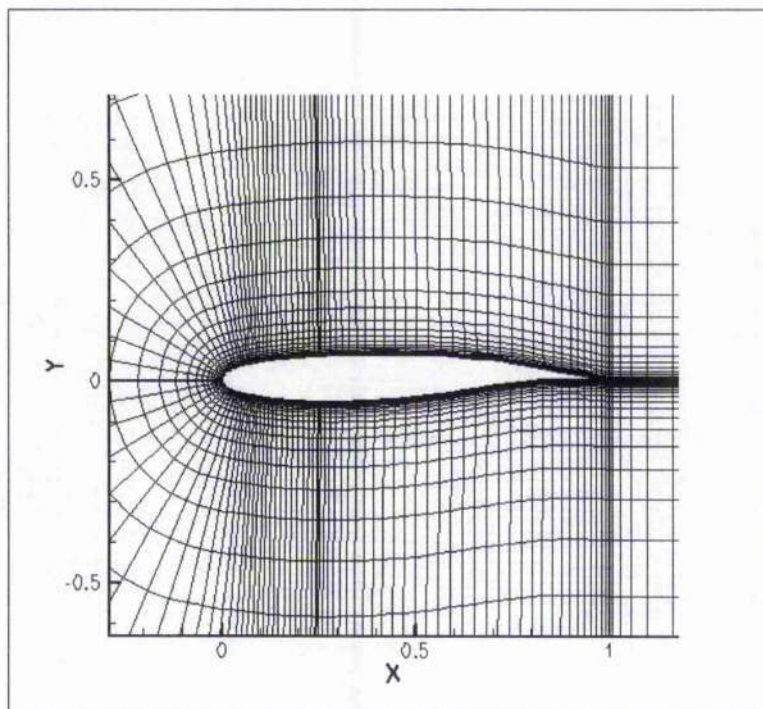


Figure 2.10: BGK No.1 aerofoil - coarse grid

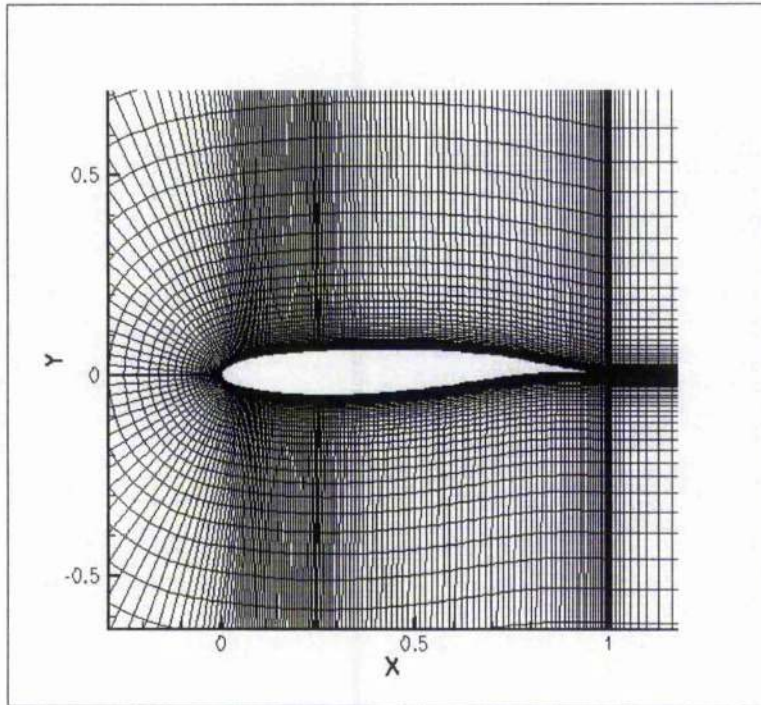


Figure 2.11: BGK No.1 aerofoil - fine grid

2.2.2 Test Case 2 - OAT15A Aerofoil

Computations were conducted using the pmb3D code developed at University of Glasgow. Only the two equation Baseline turbulence model was used for both steady and unsteady computations for this test case. Table 2.3 lists other CFD parameters given to the solver for this test case.

Two grid levels were employed in the computations, a coarse and fine grid, see Figures 2.13, and 2.14 respectively. The computational domain was extended from 54 chord lengths upstream to 60 chord lengths downstream of the leading edge of the aerofoil. Table 2.4 lists detail of finite volume grids used for this test case. All dimensions have been non-dimensionalized using

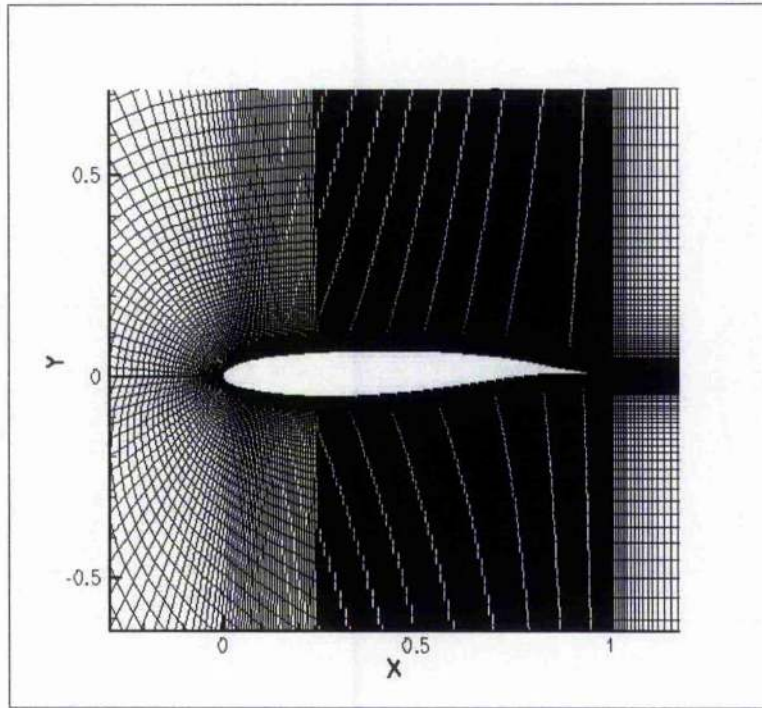


Figure 2.12: BGK No.1 aerofoil - finer grid

the aerofoil chord, c .

Grid points were clustered towards the aerofoil surfaces because of the large flow gradients that are expected in the boundary layer. Also, more points were allocated on the upper surface than on the lower surface because of the formation of shock that should occur on the upper surface. This aerofoil is truncated at the trailing edge hence a lot of points were clustered at the trailing edge in order to resolve the trailing edge boundary layer.

	Steady parameters	Unsteady parameters	Turbulence models
Steady computations	Explicit CFL: 0.4 Explicit steps: 1000 Implicit CFL: 20 Implicit step: 4000 Convergence: 1×10^{-8}		Baseline
Unsteady computations	Explicit CFL: 0.4 Explicit steps: 500 Implicit CFL: 20 Implicit step: 2000 Convergence: 1×10^{-5}	Final time: 200 No. of steps: 2000 dt: 0.1 Tolerance: 0.01 Pseudo step: 100	Baseline

Table 2.3: Numerical parameters used for test case 2

	Total number of nodes	Minimum and maximum x coordinates	Minimum and maximum y coordinates	Wall distance of the first node
Coarse grid	32, 948	-54/61	-55/55	1×10^{-5}
Fine grid	129, 300	-54/61	-55/55	1×10^{-5}

Table 2.4: Details of the finite volume grids used for test case 2

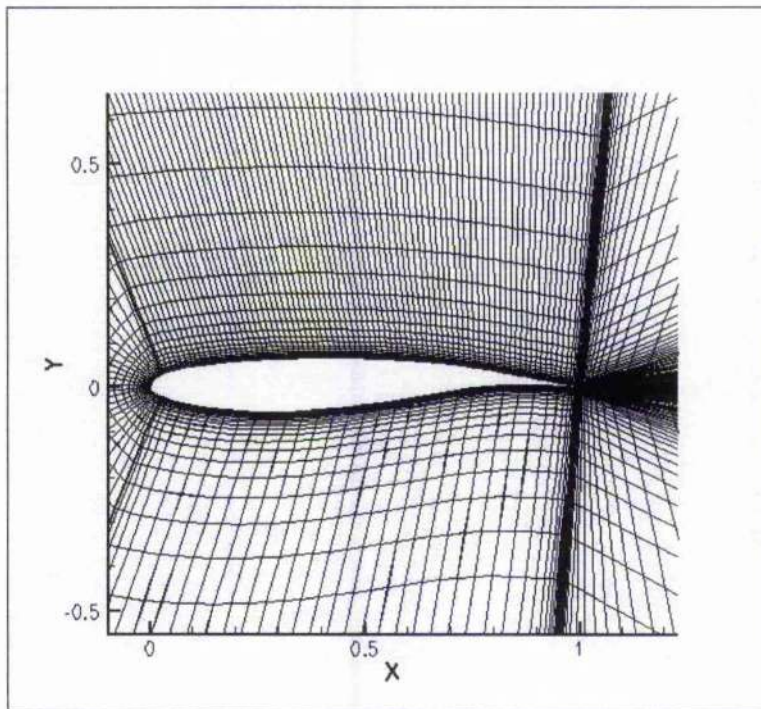


Figure 2.13: OAT15A aerofoil - coarse grid

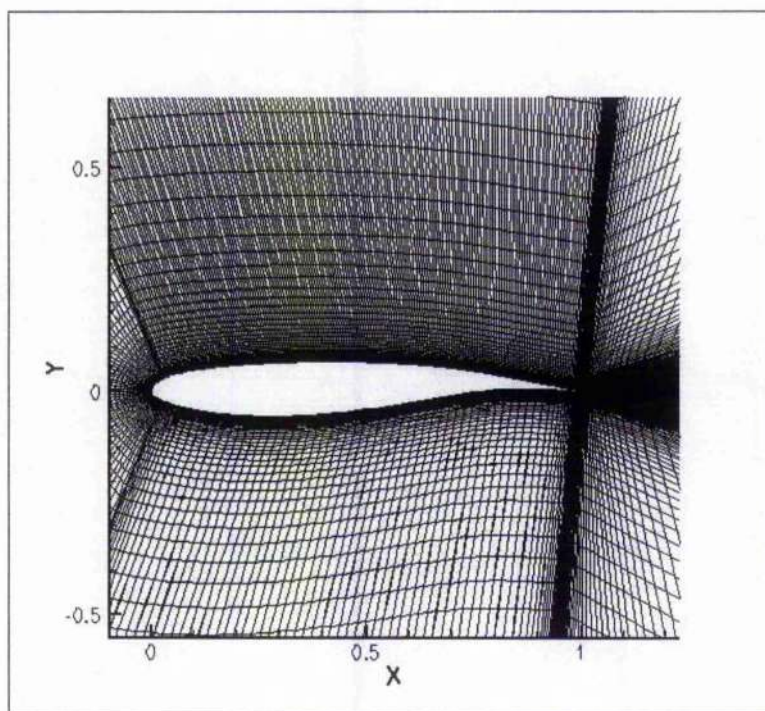


Figure 2.14: OAT15A aerofoil - Fine grid

Chapter 3

Validation and discussion of computational results

3.1 BGK No.1 Aerofoil

3.1.1 Shock/boundary layer flow field

The freestream conditions used by Lee in his experiments were simulated in the computations [33,34,35,37]. The freestream Mach number was held constant at 0.71, the Reynolds number at 20×10^6 and the angle of attack varied from -0.316° to 6.97° . At $\alpha = -0.316^\circ$, the flow on both surfaces was found to be sub-critical using the Baseline turbulence model and the coarse grid (see Figure 3.1). This finding is in agreement to Lee's experimental results. A sub-critical flow is a flow without a shock forming. Streamlines indicate that the flow is fully attached on both surfaces (see Figure 3.1).

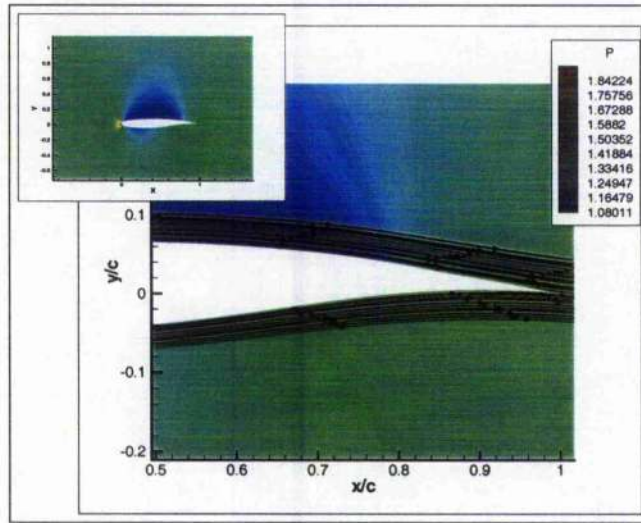


Figure 3.1: Pressure contours and streamlines plot at $M = 0.71$, $Re=20 \times 10^6$ and $\alpha = -0.316^\circ$

At $\alpha = 1.396^\circ$, a weak shock forms but the flow still remains fully attached, see Figures 3.2.

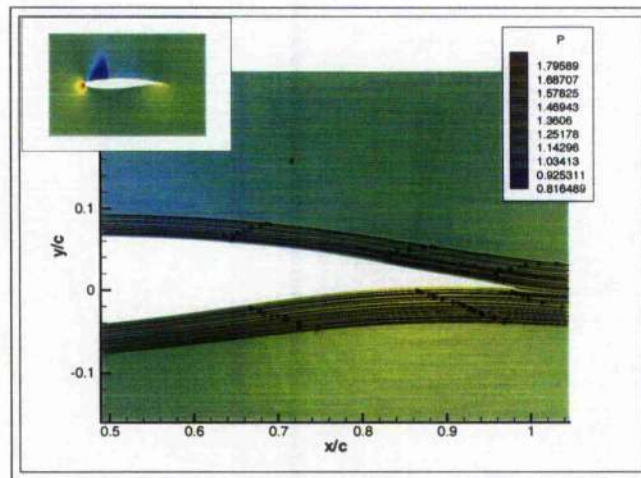


Figure 3.2: Pressure contours and streamlines plot at $M = 0.71$, $Re=20 \times 10^6$ and $\alpha = 1.396^\circ$

A stronger shock is noticeable when α is increased to 3.017° . Figure

3.3 shows pressure contours and streamlines plot at $\alpha = 3.017^\circ$. There is a thickening of the boundary layer after the now strengthened shock. Results indicate that the shock is strong enough to induce a small separation bubble at the foot of the shock, however there is still no evidence of trailing edge separation. This result is inconsistent with experimental findings by Lee[37], where the flow remains attached on both surfaces.

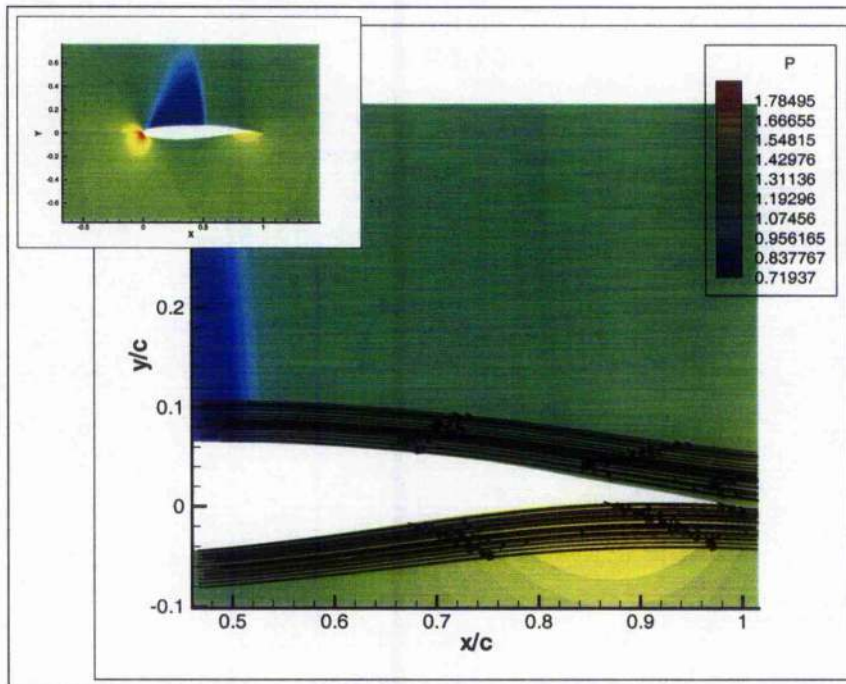


Figure 3.3: Pressure contours and streamlines plot at $M = 0.71$, $Re = 20 \times 10^6$ and $\alpha = 3.017^\circ$

Increasing α to 4.905° results in the formation of a stronger shock which causes the flow to separate and then reattach to form a separation bubble. The separation bubble has now increased in size. Trailing edge separation is also formed, see Figures 3.4 and 3.5. This result is in disagreement with Lee's

findings, which showed no trailing edge separation at this angle of attack.

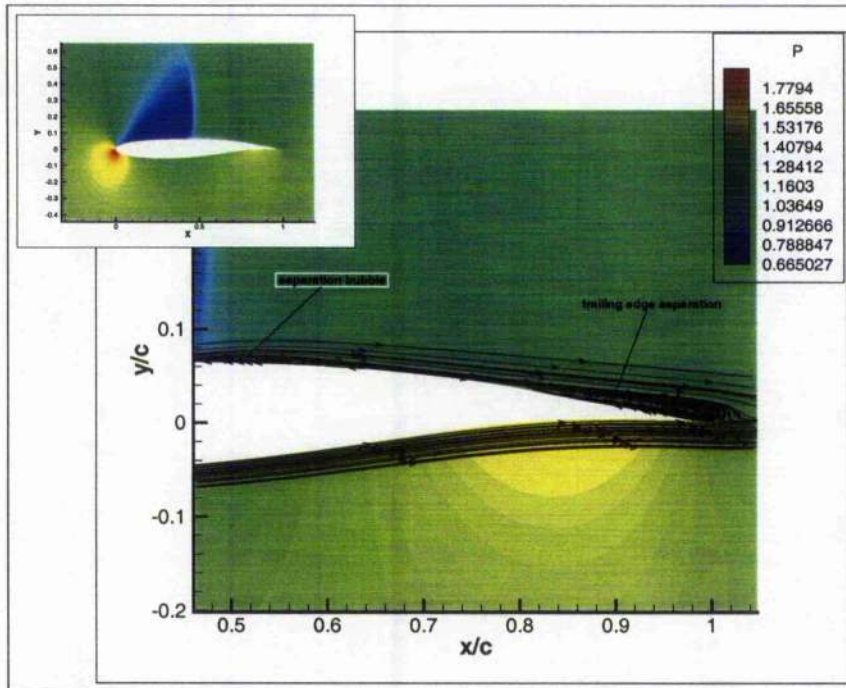


Figure 3.4: Pressure contours and streamlines plot at $M = 0.71$, $Re = 20 \times 10^6$ and $\alpha = 4.905^\circ$

When α is increased to 6.97° , the flow becomes fully separated. This is consistent with Lee's findings. Also the structure of the shock has now changed from a normal shock to an oblique shock, see Figure 3.6.

Turbulence models play a significant role in the validation of computational results. Figure 3.7 shows that prediction of the shock position varies depending on the turbulence model employed. It can be seen that the Baseline and SST models give the best shock locations at high angles of attack. However, at low angles of attack there are only small differences in the prediction of the shock location. All the turbulence models accurately predicted

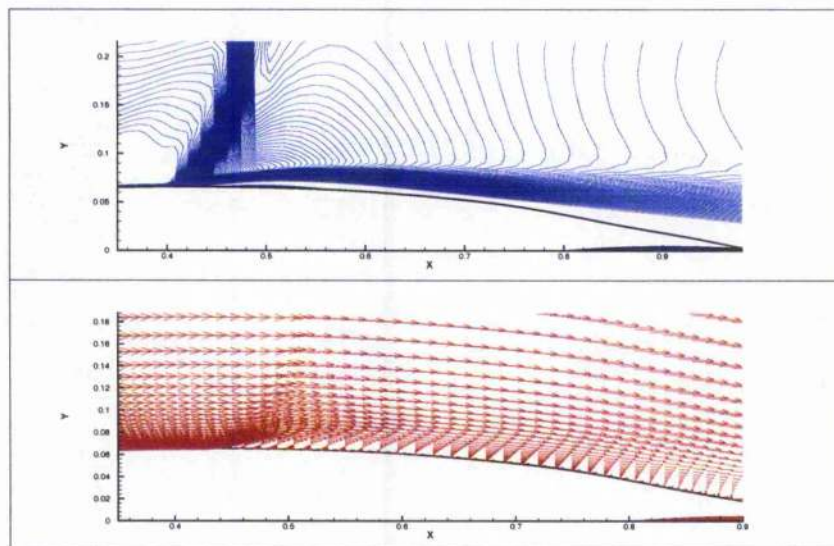


Figure 3.5: Mach number contours and velocity vector plots at $M = 0.71$, $Re=20 \times 10^6$ and $\alpha = 4.905^\circ$

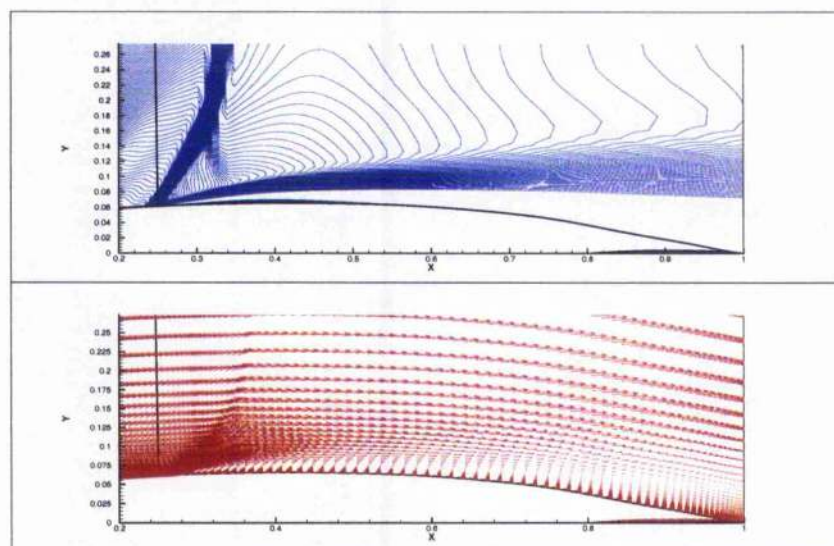


Figure 3.6: Mach number contours and velocity vector plot at $M = 0.71$, $Re=20 \times 10^6$ and $\alpha = 6.970^\circ$

the relationship between shock location and angle of attack, a downstream movement of the shock as angle of attack increases until a critical angle of attack is reached when then there is an upstream movement. However, this critical angle of attack depends on the turbulence model used.

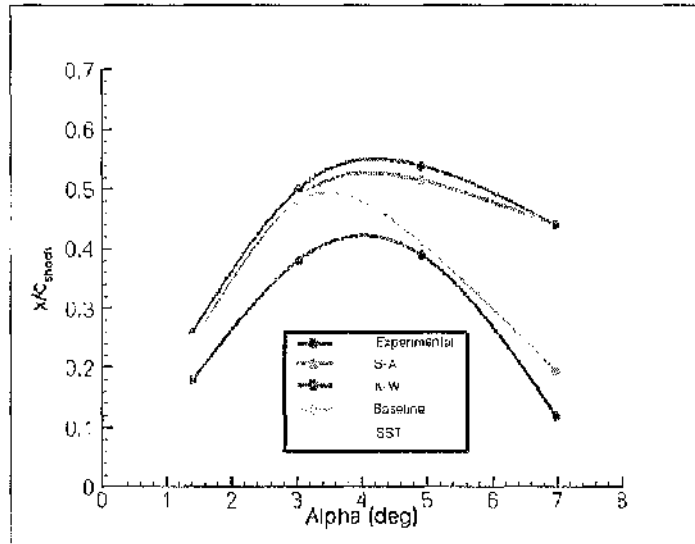


Figure 3.7: Shock location related to angle of attack for the different turbulence models

The prediction of separation regions is also heavily dependent on the turbulence models employed. Consider Figure 3.8, which shows that at angles of attack of -0.316° and 1.396° all the turbulence models predicted a fully attached flow on the upper surface of the aerofoil. This is in agreement with experimental results.

Discrepancies in the separation regions begin to appear when α is increased to 3.017° (see Figure 3.9). Both the Baseline and SST models predicted a very small separation bubble at the foot of the shock, inconsistent with experimental findings by Lee. The $k-\omega$ model gives the best agreement

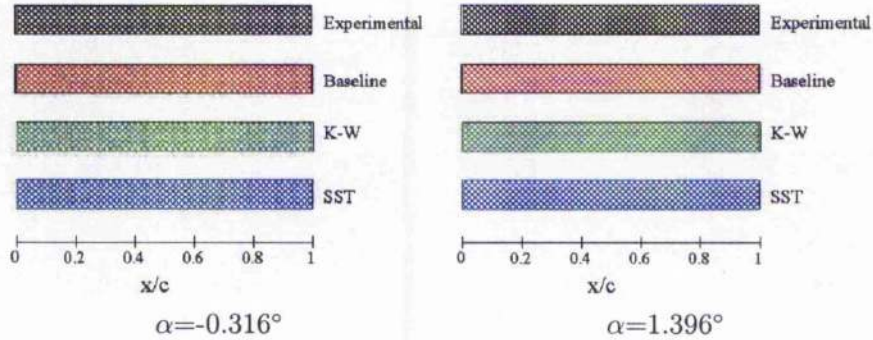


Figure 3.8: Attached flows at two different angles of attacks

with experimental results.

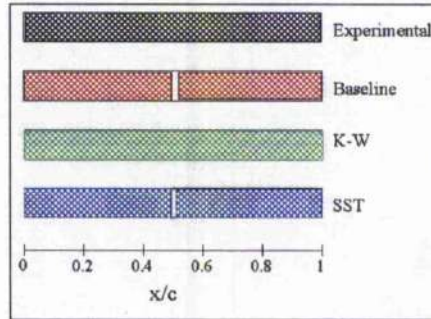


Figure 3.9: Attached and separated flow at $\alpha=3.017^\circ$

Differences in the separation regions are also noticeable when α is increased to 4.905° , see Figure 3.10. The $k-\omega$ model gives the best agreement with experimental results. Both the Baseline and SST models over-predicted the separation bubble and in addition predicted a trailing edge separation. The $k-\omega$ model predicted separation further downstream than experimental findings and the other two models.

When the angle of attack is increased to 6.970° Lee observed total separation at around $x/c=0.4$. Here the SST and Baseline models give the closest

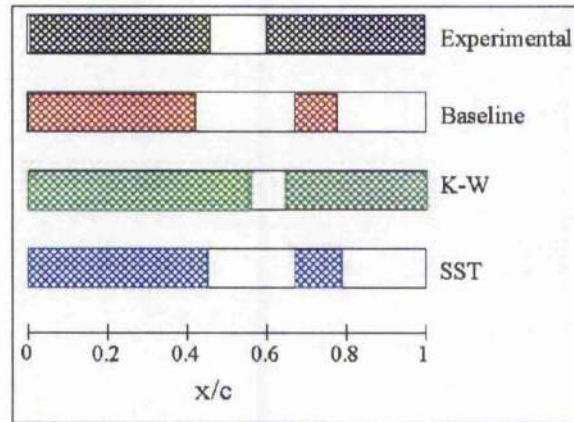


Figure 3.10: Attached and separated flow at $\alpha=4.905^\circ$

agreement to Lee's results (see Figure 3.11).

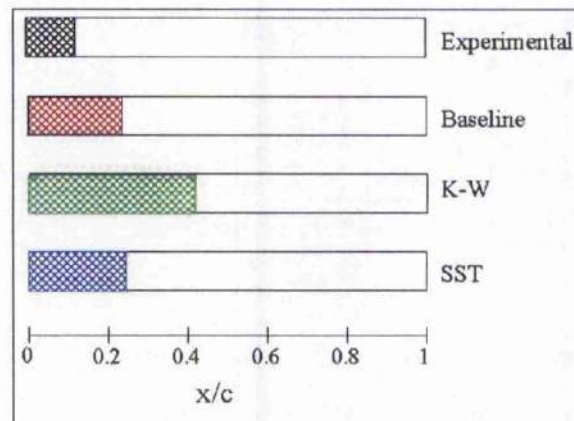


Figure 3.11: Attached and separated flow at $\alpha=6.970^\circ$

An investigation of different boundary layer properties might explain why the regions of separation vary with turbulence models. Figure 3.12 shows the turbulence Reynolds number profile for $\alpha=4.905^\circ$ before the shock, where,

$$Re_t = \frac{\rho k^2}{\mu \epsilon}$$

here k is the turbulent kinetic energy, ϵ is the dissipation rate of k and μ is the coefficient of molecular viscosity. It can be seen that the $k-\omega$ model has a thicker boundary layer than the SST and Baseline. The more turbulent flow before the shock for the $k-\omega$ model is responsible for the delayed separation.

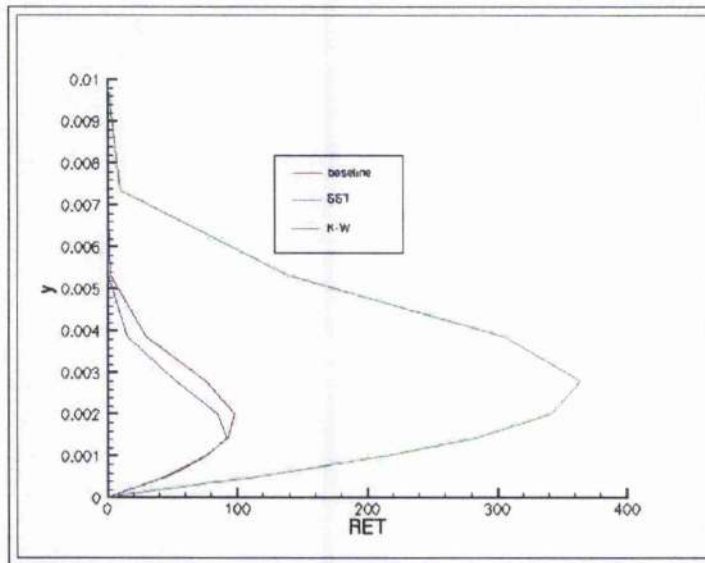


Figure 3.12: Turbulence Reynolds number profiles before the shock ($x/c=0.35$) for different turbulent models, $\alpha = 4.905^\circ$, $M = 0.71$ and $Re = 20 \times 10^6$

The Baseline and SST models have a thicker and more turbulent boundary layer after the shock (see Figure 3.13). This is because the centre of the separation bubble for the Baseline and SST is located at the $x/c=0.57$ vicinity whereas $x/c=0.57$ is at the start of the separation bubble for the $k-\omega$ model. There is a thicker boundary layer at the centre of the separation bubble than at the start.

The difference in convergence levels of the steady solution helps to give an understanding into why the different turbulence models produce different

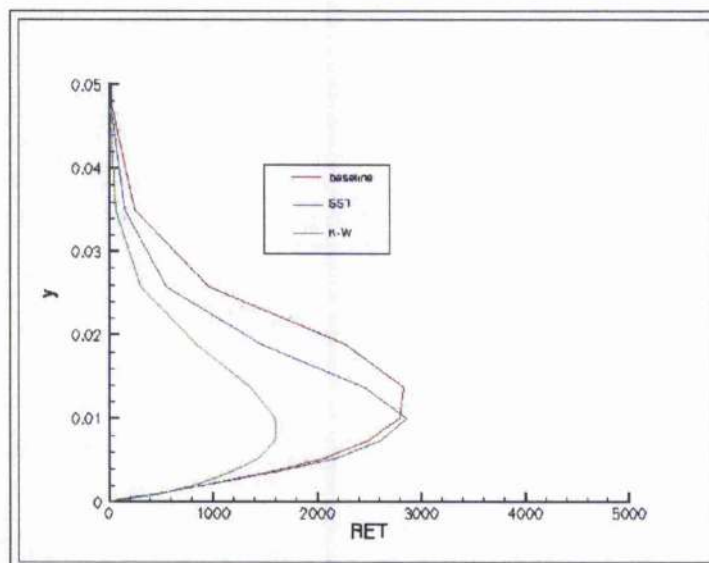


Figure 3.13: Turbulence Reynolds number profiles after the shock ($x/c=0.6$) for different turbulent models, $\alpha = 4.905^\circ$, $M = 0.71$ and $Re = 20 \times 10^6$

separation regions and to an extent give an indication of which models will produce a buffet flow field at the various angles of attack when an unsteady calculation is ran. Figure 3.14 shows the convergence levels at $\alpha = -0.316^\circ$ for the three models. Attached flow was predicted for all turbulence models at this angle of attack and hence good convergence levels are deduced from the plots.

The residual plots for $\alpha = 3.017^\circ$ reveals small fluctuations in both the mean and turbulent residuals for the Baseline and SST models (see Figure 3.15). These fluctuations occur because there is an emergence of a separation bubble for these models. Fluctuations are of higher magnitude for the Baseline model than for the SST hence the Baseline model has a larger separation region. However, the $k-\omega$ model has reached a good convergence level and as

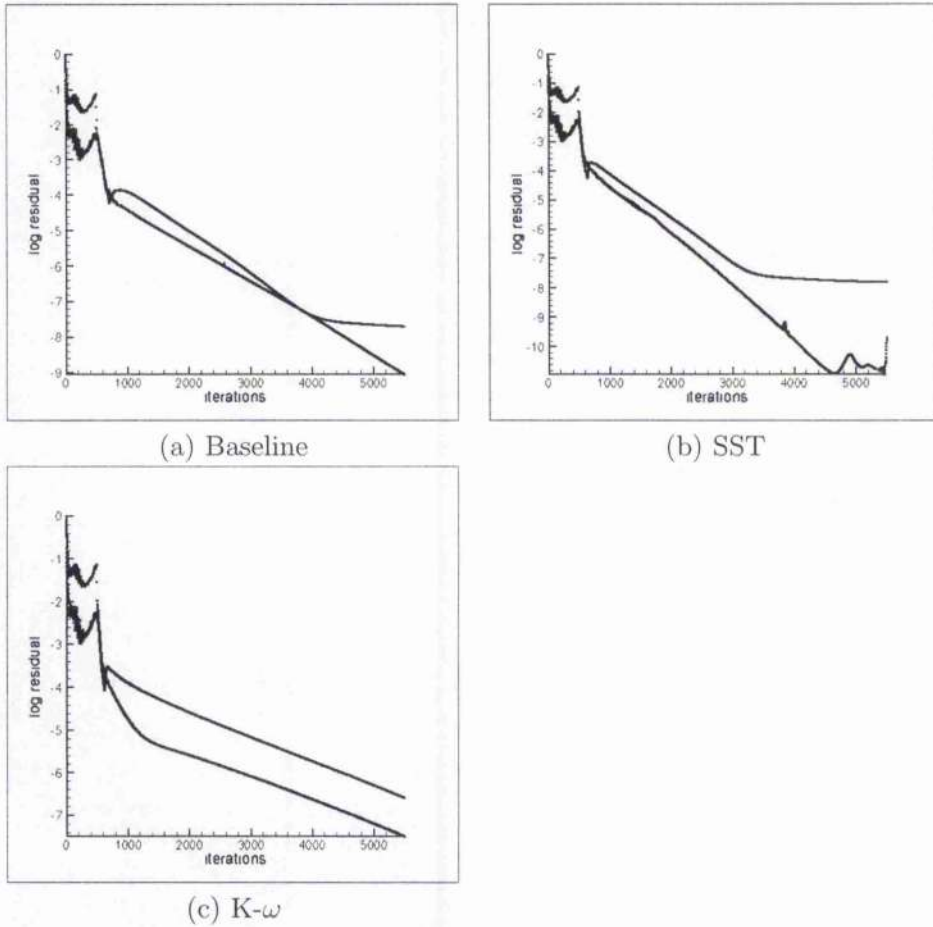


Figure 3.14: Residual plots for $\alpha = -0.316^\circ$, $M = 0.71$ and $Re = 20 \times 10^6$

a result there is an attached flow field.

The residual plots for $\alpha = 4.905^\circ$ show fluctuations in both the mean and turbulent residuals for the Baseline and SST models, however fluctuations only occur in the turbulent residual for the k- ω model (see Figure 3.16). The convergence levels are poor for all models indicating the occurrence of separation for all models. One should expect larger regions of separation for

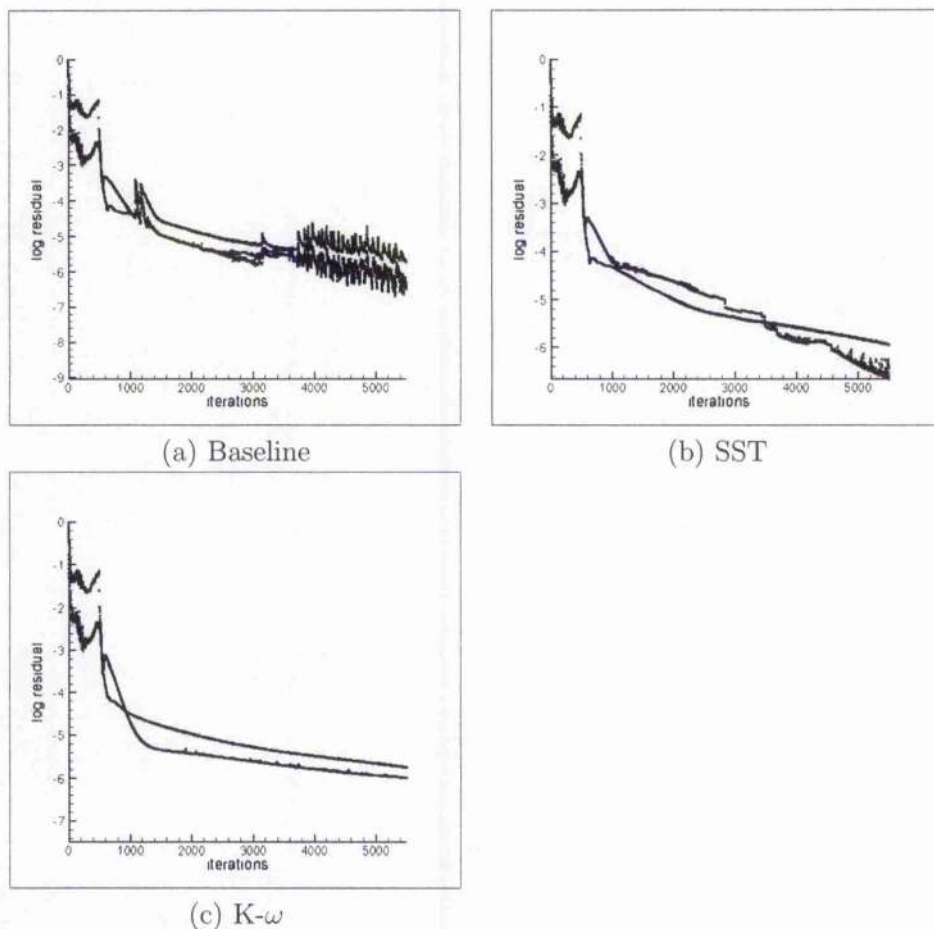


Figure 3.15: Residual plots for $\alpha = 3.017^\circ$, $M=0.71$ and $Re = 20 \times 10^6$

the SST and Baseline models.

The residual plots for $\alpha = 6.970^\circ$ follow the same trend as for $\alpha = 4.905^\circ$. However the fluctuations are of higher magnitude for all models. The fluctuations are of greater magnitude for the Baseline models than for the SST model (see Figure 3.17).

The residual plots for the steady solutions have established that the Base-

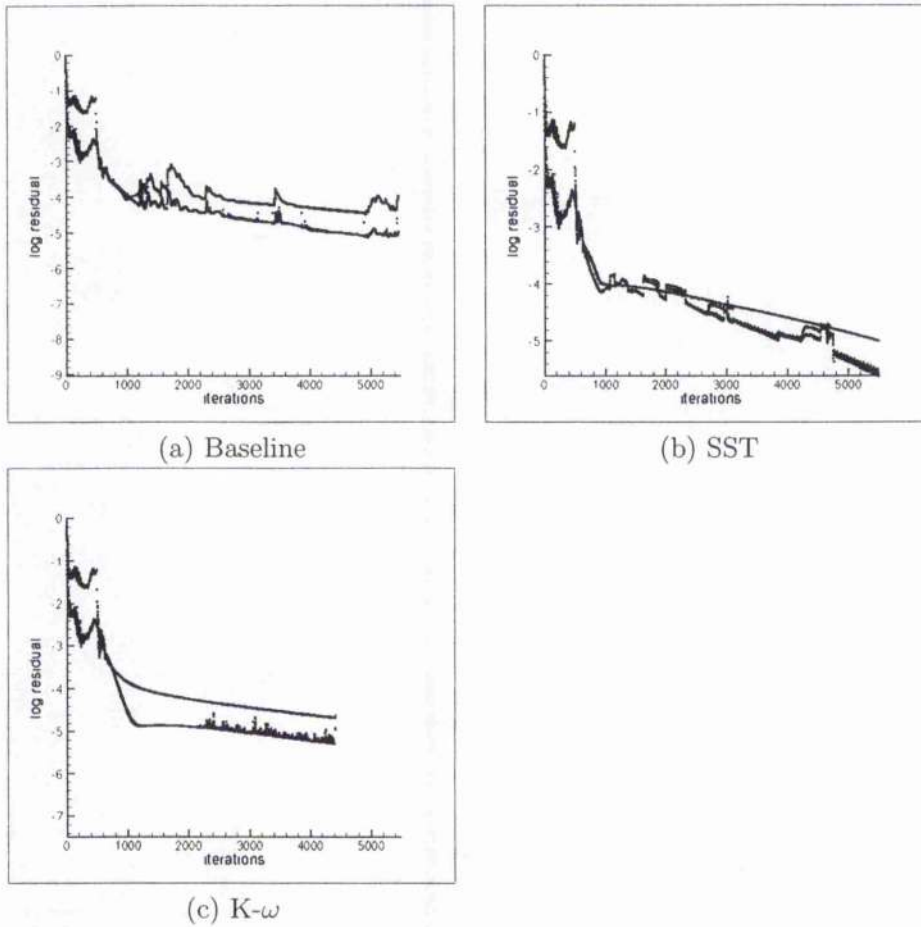


Figure 3.16: Residual plots for $\alpha = 4.905^\circ$, $M = 0.71$ and $Re = 20 \times 10^6$

line and SST models are most likely to produce a buffet flow field and that buffet will occur between $\alpha = 3.017^\circ$ and $\alpha = 4.905^\circ$.

A validation of steady surface pressure was also carried out. Figure 3.18 shows that the agreement between experimental and computational results is relatively very good for an angle of attack of -0.316° , this is because there is no evidence of large pressure gradient in the flow field. The ripples on the

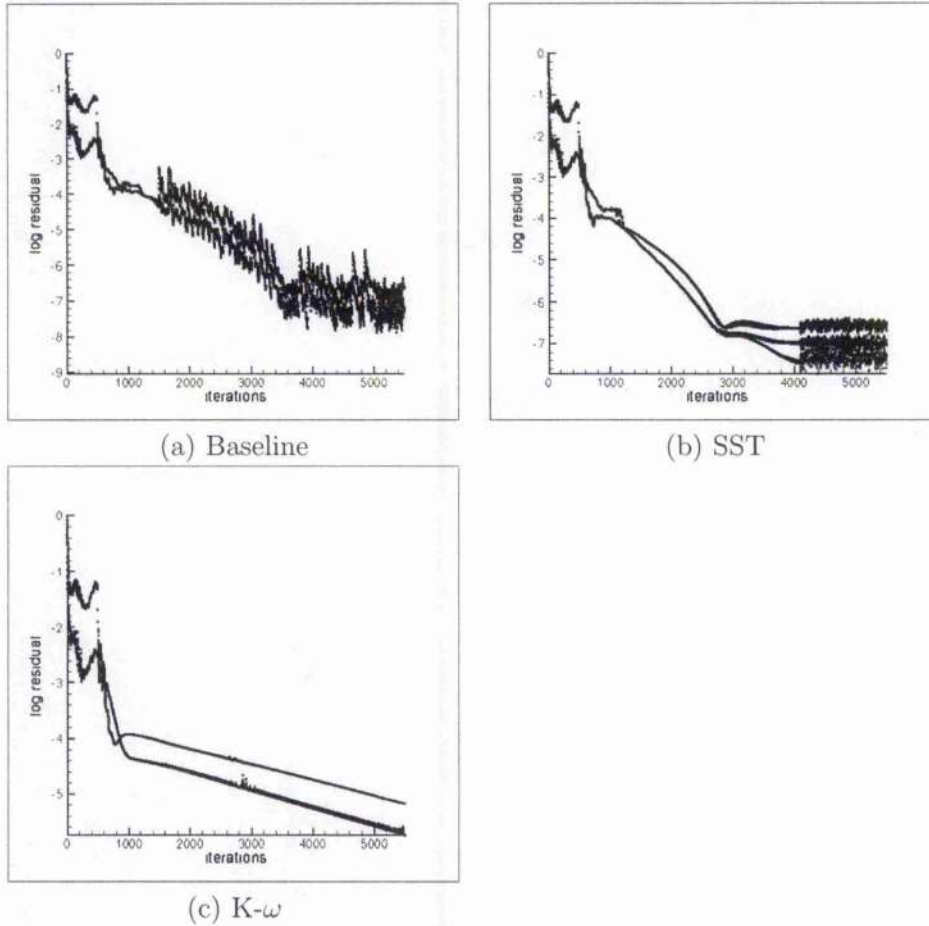


Figure 3.17: Residual plots for $\alpha = 6.970^\circ$ $M = 0.71$ and $Re = 20 \times 10^6$

computational surface plots are due to the fact that the geometry published for this aerofoil isn't very smooth.

Figure 3.19 shows the surface pressures for an angle of attack of 1.396° . At this angle of attack there is a formation of a shock on the upper surface and all turbulence models fail to correctly predict the position of the shock. All turbulence models slightly over-predict the pressure plateau in the supersonic

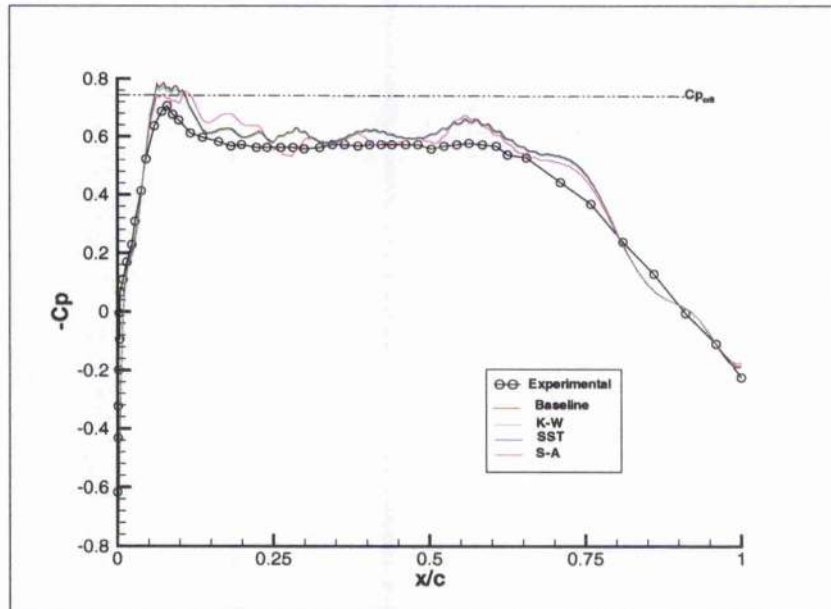


Figure 3.18: Steady surface pressure plots on the upper surface of the BGK No.1 aerofoil at $\alpha = -0.316^\circ$

region. However, there is a relatively good agreement in the trailing edge pressures, this is because all turbulence models predicted attached flow at the trailing edge.

Figure 3.20 shows the surface pressures for an angle of attack of 4.905° . At this angle of attack there is a formation of a stronger shock on the upper surface and all turbulence models fail to correctly predict the position of the shock. The strength of the shock is reasonably predicted by all models. The $k-\omega$ model predicts the trailing edge pressure better than the other models, this is because only the $k-\omega$ model predicted an attached flow at the trailing edge as observed in experiments and the other models predicted separated flows.

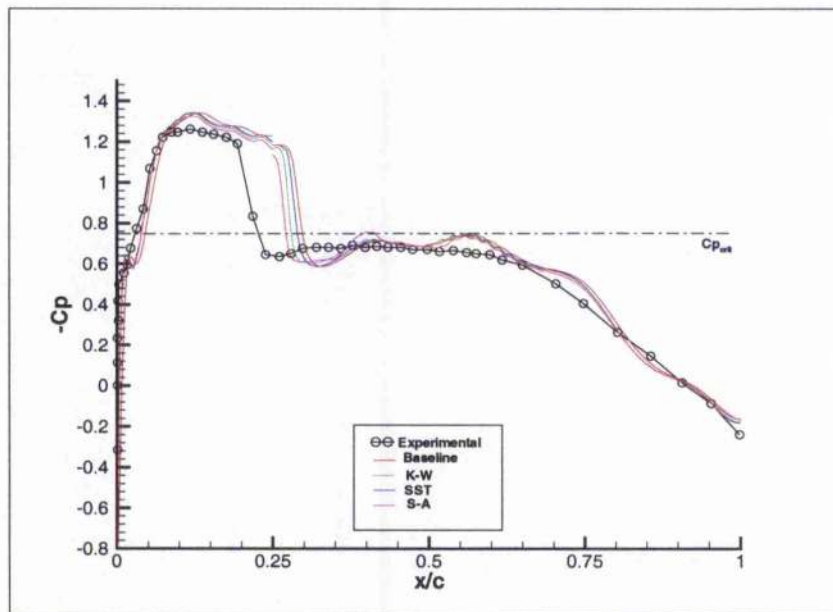


Figure 3.19: Steady surface pressure plots on the upper surface of the BGK No.1 aerofoil at $\alpha=1.396^\circ$

3.1.2 Unsteady mechanism of buffet

Unsteady computations for the BGK No.1 aerofoil were done for three angles of attack using the Baseline turbulence model, at 3.017° , 4.905° and 6.970° . All other computational parameters were kept constant and the influence of angle of attack was investigated. The variation of lift coefficient with time can be used to indicate the differences in the flow field as the angle of attack is increased. Figure 3.21 shows the variation of lift coefficient with time as the flow passes over the aerofoil quarter chord position. At 3.017° there is a steady decay of lift at that point as time increases and this eventually comes to a constant value. However at $\alpha=4.905^\circ$ and 6.970° , the lift coefficient oscillates almost at constant amplitude. It can be concluded that at the two

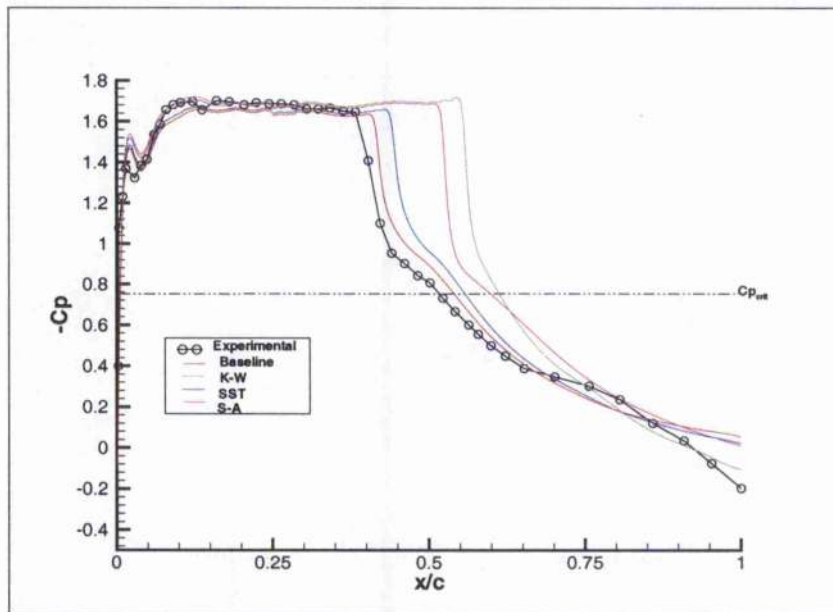


Figure 3.20: Steady surface pressure plots on the upper surface of the BGK No.1 aerofoil at $\alpha=4.905^\circ$

latter angles of attack there is an unsteady flow field, whilst the flow at 3.017° is steady.

It can also be concluded that the level of unsteadiness is of a higher magnitude for $\alpha = 6.970^\circ$ than for $\alpha = 4.905^\circ$. This result is consistent with the experimental results of Lee.

The unsteady mechanism of buffet can be understood by considering the behaviour of the shock movement. The variation of shock strength and boundary layer thickness can be used to explain the driving-mechanism behind the self-sustained shock movement. Figure 3.22 shows the shock movement on the upper surface of the aerofoil at angle of attack of 4.905° . This figure shows an upstream and downstream shock movement as time changes.

The frequency of shock oscillation is under-predicted; Lee found the fre-

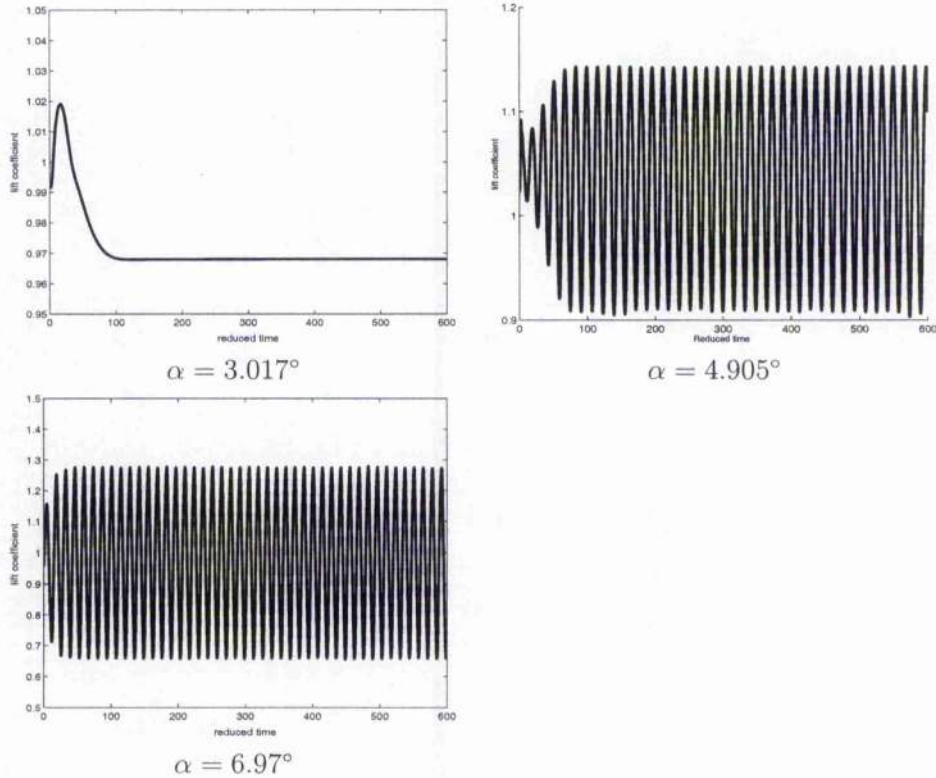


Figure 3.21: Lift coefficient plots using the Baseline model for various angles of attack using the coarse grid, $M = 0.71$ and $Re = 20 \times 10^6$

quency of oscillation to be around 75 Hz in his experiments whilst the computational shock oscillation is only around 60 Hz. This frequency was calculated by taking the reciprocal of the time the shock takes to complete a full cycle of movement. The magnitude of shock movement on the upper surface of the aerofoil is over-predicted using the Baseline turbulence model. Lee found the magnitude of shock movement to be around $x/c = 0.05$.

Figure 3.23 shows the changes in shock height as the shock moves both

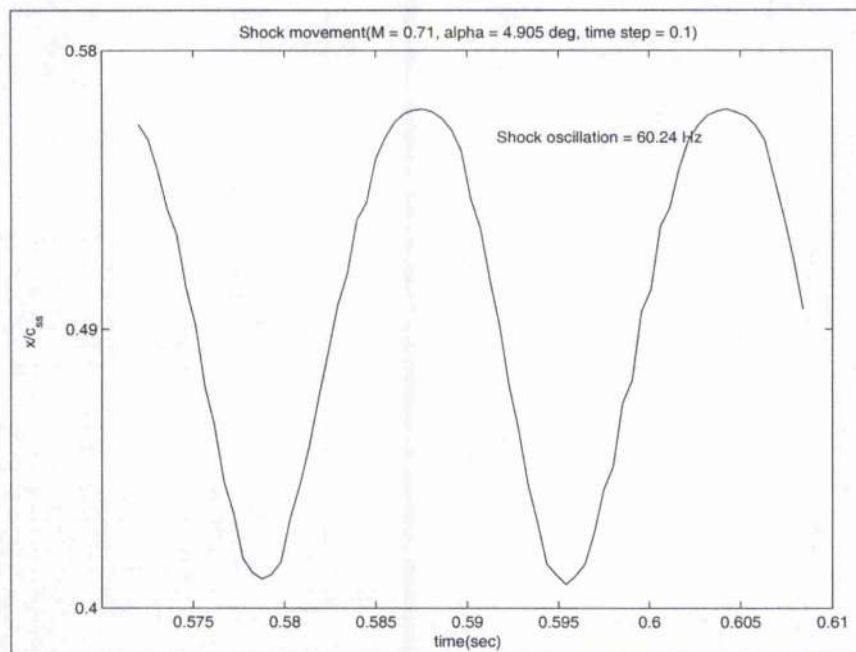


Figure 3.22: Shock movement with the Baseline model

upstream and downstream on the aerofoil. The shock height is defined as the maximum distance of the shock normal to the aerofoil surface. The shock height is also a way of representing the shock strength, a stronger shock will have a higher shock height. It can be seen that the shock strength increases as the shock moves downstream of the aerofoil. This should be expected because the shock naturally increases speed as it moves downstream due to the curvature of the aerofoil. The higher speeds lead to a stronger shock.

The reverse occurs for an upstream movement of the shock. Figure 3.24 shows the changes in trailing edge displacement thickness as the shock moves either upstream or downstream of the aerofoil. The trailing edge displac-

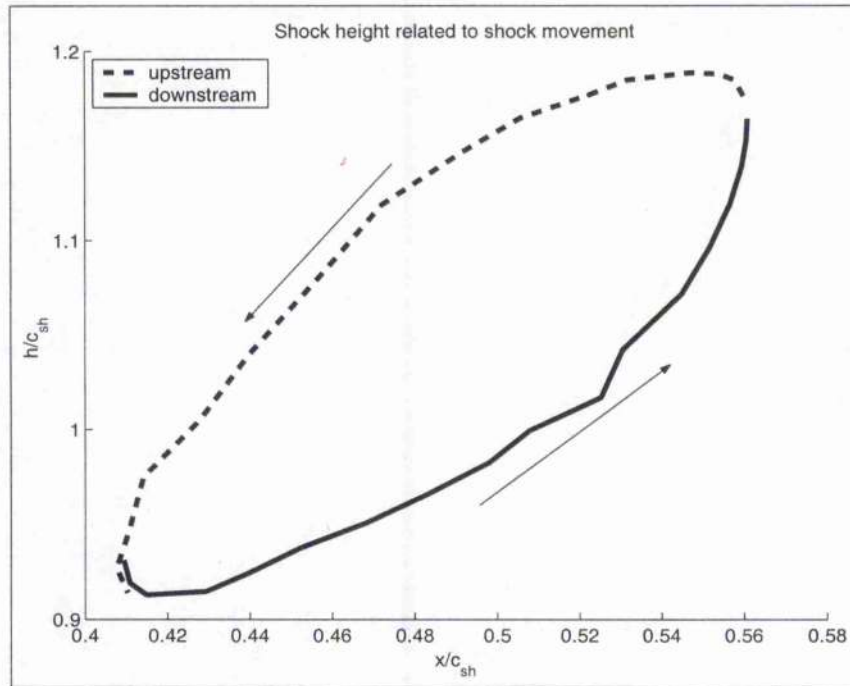


Figure 3.23: One cycle of shock movement at $\alpha=4.905^\circ$, Baseline and coarse grid

ment thickness, σ^* was calculated using the following relationship:

$$\sigma^* = \int_0^\infty \left(1 - \frac{\rho U}{\rho_e U_e} \right) dy$$

where ρ and U are density and velocity respectively, ρ_e and U_e are density and velocity at the edge of the boundary layer respectively.

During the upstream movement the displacement thickness at the trailing edge increases. The communication between the shock strength and the trailing edge displacement thickness and the coupling between the shock movement and the changes in the trailing edge pressure is responsible for the self-sustained shock movement.

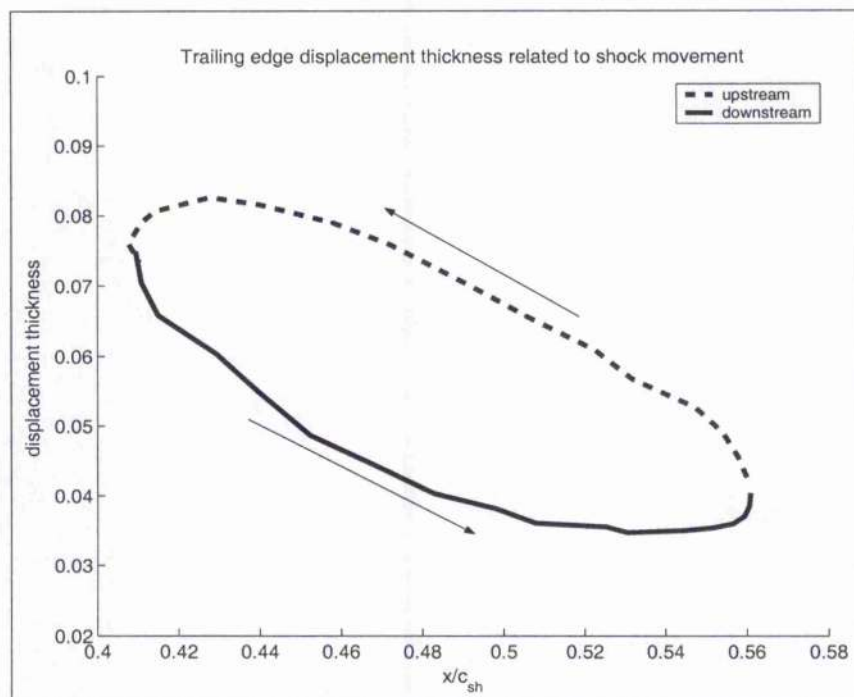


Figure 3.24: One cycle of shock movement at $\alpha=4.905^\circ$, Baseline and coarse grid

The close relation between shock location and the boundary layer thickness at the trailing edge and the separation bubble is illustrated in Figure 3.25. It can be seen that the most forward shock location corresponds closely to a state in time where the boundary layer at the trailing edge and the bubble reaches maximum thickness, while the most aft location of the shock is associated to a nearly attached boundary layer at the trailing edge or the bubble.

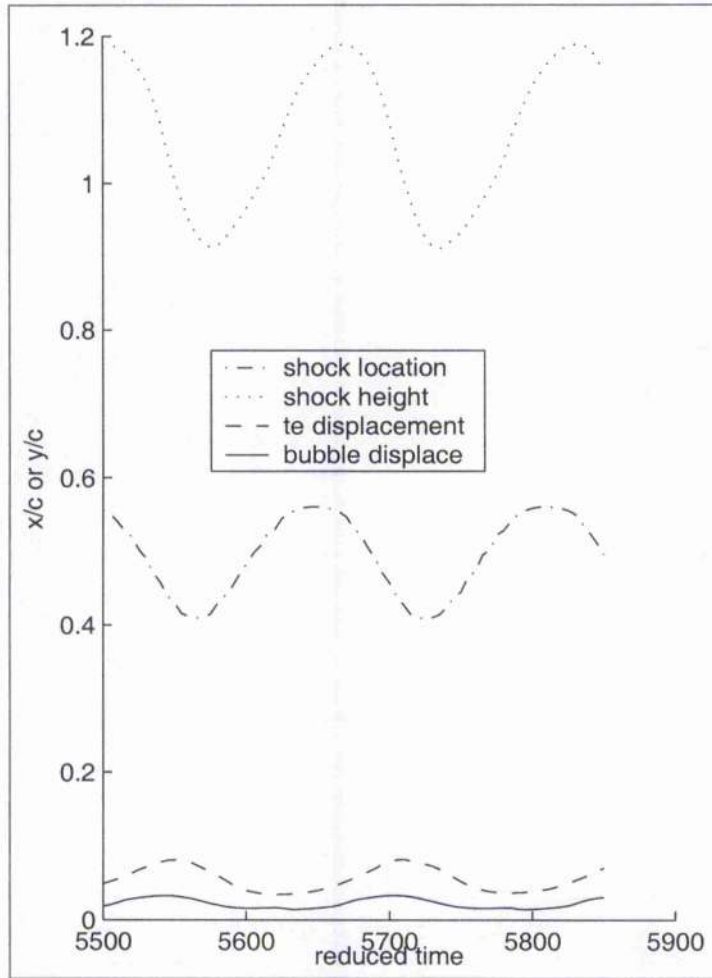


Figure 3.25: Variations in shock movement, shock height and boundary layer thickness through time for $\alpha=4.905^\circ$

A validation of the unsteady pressure coefficient, \bar{C}_p was also carried out. \bar{C}_p was calculated using the following equation:

$$\bar{C}_p = C_{p_s} + \tilde{C}_p$$

where C_{p_s} is the steady surface pressure coefficient and \tilde{C}_p is the fluctuating

pressure coefficient.

Figure 3.26 shows the unsteady pressure coefficients at different probe points along the upper surface, experimental results are on the left and the computational results using the Baseline model are on the right. These probe points correspond to the location of the transducers discussed in section 2.1.1. Lee detected large pressure oscillations at transducer I; pressure fluctuations were quite uniform inside the separation bubble and pressure fluctuations were quite small downstream of the bubble. Computational results show large pressure oscillations at transducers I, J and K. This indicates a stronger shock was predicted computationally. The magnitude of the computational pressure fluctuations are relatively large compared to the experimental pressures downstream of the bubble; this may be because a trailing edge separation was predicted by the Baseline model whilst Lee observed attached flow in his experiments.

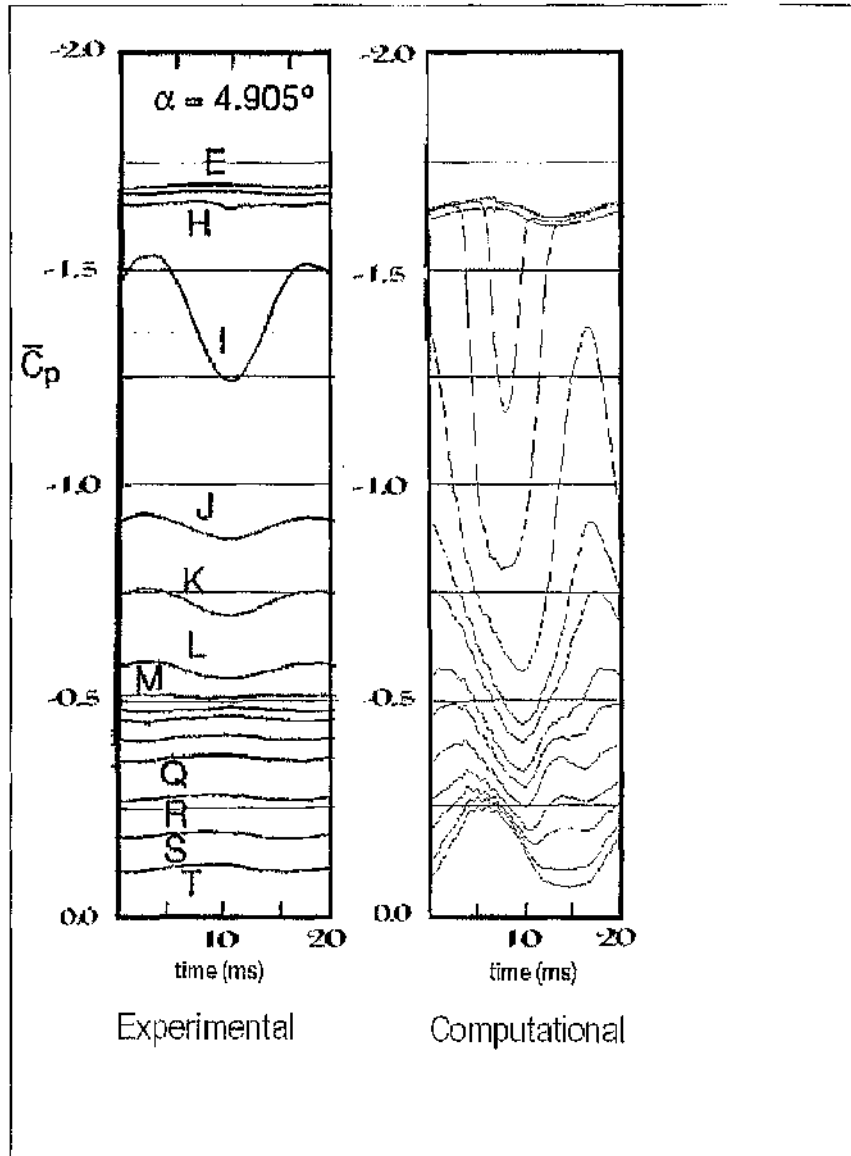


Figure 3.26: Experimental unsteady pressures compared with computational unsteady pressures using the Baseline model, $\alpha = 4.905^\circ$, $M = 0.71$ and $Re = 20 \times 10^6$

Figure 3.27 presents a closer look at the experimental and computational unsteady pressure coefficients at transducers I and J. It can be clearly seen

that the pressure fluctuations are larger computationally than experimentally, indicating that a more unsteady flow was predicted by the Baseline model.

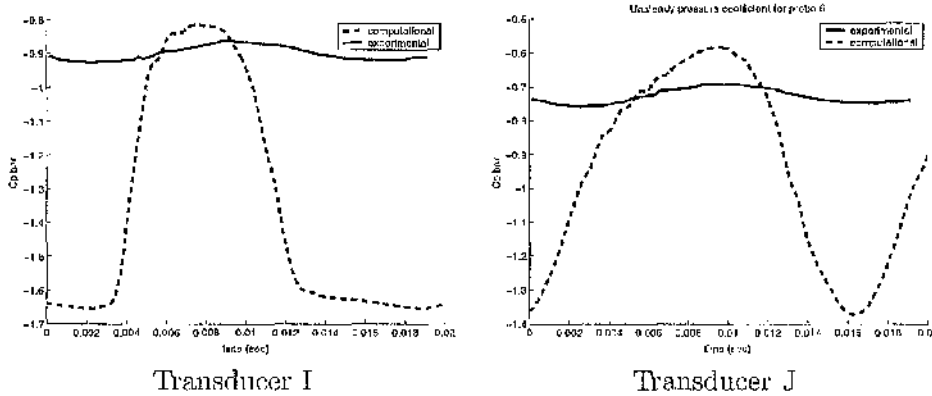


Figure 3.27: A closer comparison between experimental and computational unsteady pressures using the Baseline, model $\alpha = 4.905^\circ$, $M = 0.71$ and $Re=20 \times 10^6$

Figure 3.28 shows the variations of pressure spectra at various probe locations for the baseline model using the coarse grid. The probe locations on the aerofoil upper surface where the spectra are computed are shown in section 2.1.1. A single dominant frequency at around 60 Hz can be seen at all probe locations, this dominant frequency is due to the discrete shock movement. This frequency is consistent with the frequency calculated in Figure 3.22. Note that a linear scale is used here only to demonstrate the dominant frequency and it's corresponding pressure peak, as this frequency and pressure peaks are due to the unsteady shock oscillations. The pressure at this dominant frequency is considerably higher for the probes immediately after the shock location. Probe K is located very close to the bubble and

trailing edge separation interaction zone hence have higher pressures than probe T which is located at the trailing edge separation, further away from the interaction zone. Also visible on this plot are the harmonics for the dominant frequency.

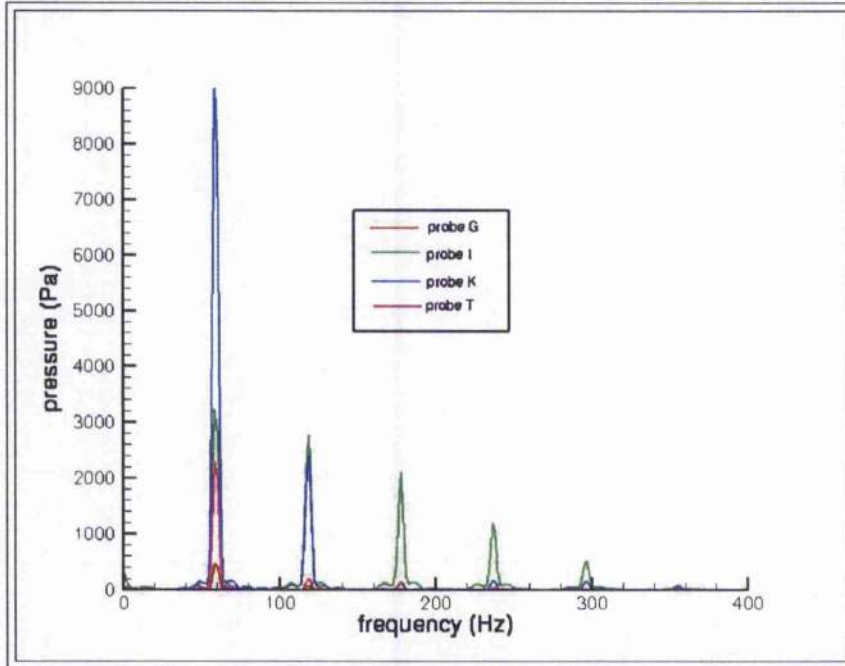


Figure 3.28: Variations of pressure spectra at various probe locations at $M = 0.71$, $Re=20 \times 10^6$ and $\alpha = 4.905^\circ$ using the Baseline model and coarse grid.

One should note that all the results so far were obtained using the coarse grid.

3.1.3 Grid and time step refinement

Steady flow field

The influence of grid refinement on the steady solution was also investigated. Figures 3.29 and 3.30 show that the surface pressures are independent of grid resolution. Only the Baseline model was used in this investigation. This clearly indicates that the three grids generated are of good quality for steady flows. However, the very fine grid does show some oscillatory behaviour which may suggest that the steady flow field may be grid dependent. This oscillatory behaviour may be due to the fact that the geometry published for the aerofoil is not very smooth. This can only be proven by doing further grid refinement studies.

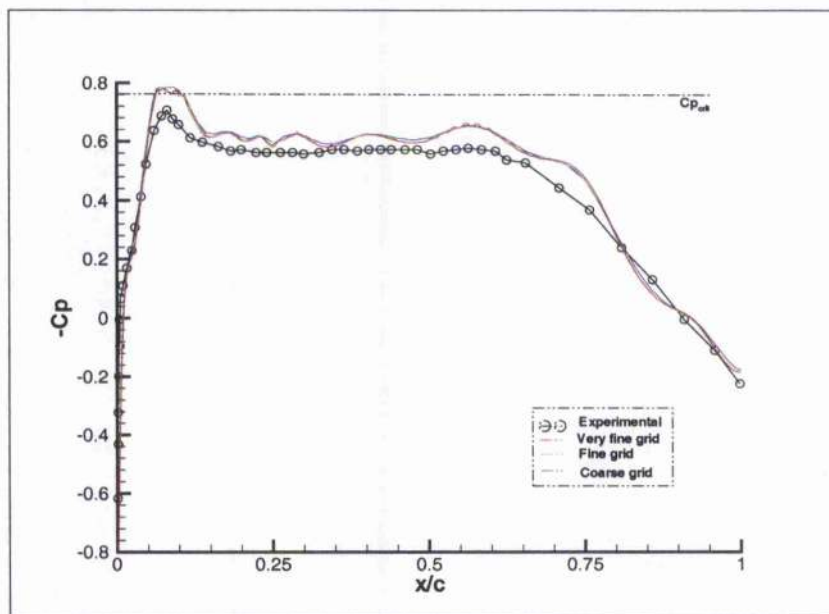


Figure 3.29: Effects of grids on surface pressures at $\alpha = -0.316^\circ$

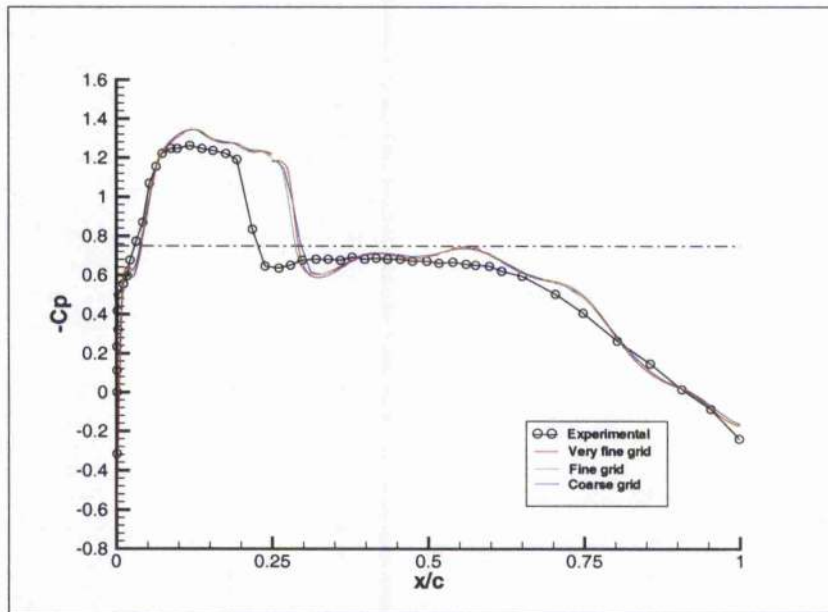


Figure 3.30: Effects of grids on surface pressure at $\alpha = 1.396^\circ$

Unsteady flow field

Next, all the computational parameters were kept constant and the effect of turbulence models on the computational results was investigated at an angle of attack of 4.905° . The coarse grid was used in this part of the study. Figure 3.31 shows the lift coefficient plots for three different turbulence models. The results of the unsteady computations are heavily dependent on turbulence models employed. Both the $k-\omega$ and SST models produced a steady flow field. Only the Baseline model produced an unsteady result.

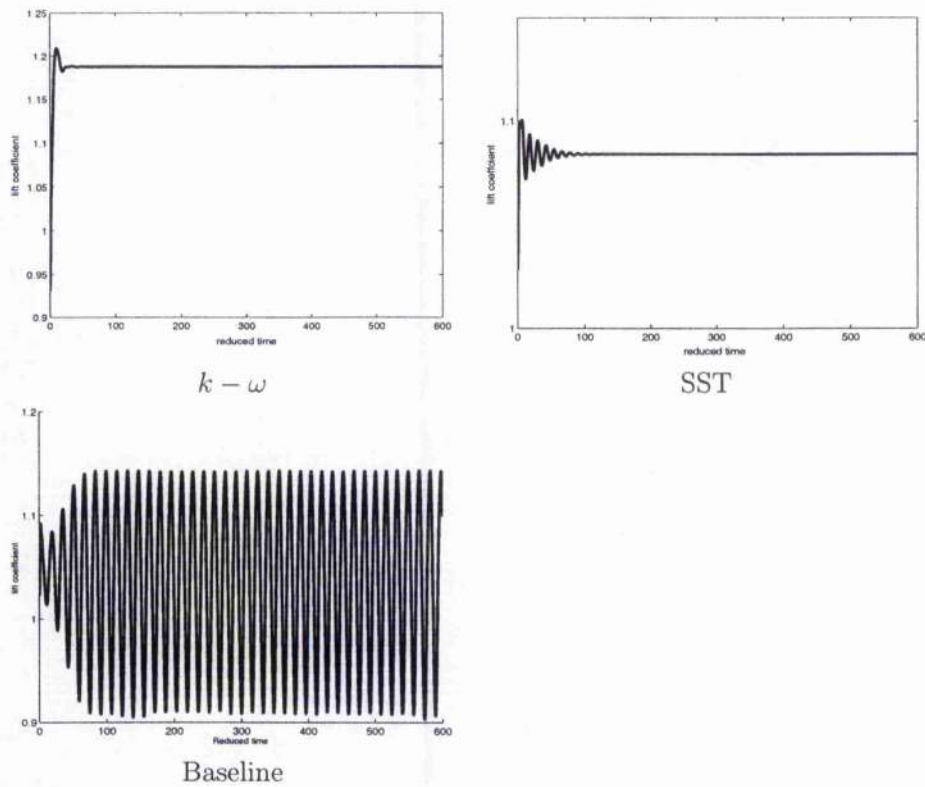


Figure 3.31: Lift coefficient plots using the Baseline model for various angles of attack using the coarse grid, $M = 0.71$ and $Re = 20 \times 10^6$

A time step refinement study was carried out using the coarse grid and the Baseline model. Figure 3.32 shows results obtained using two different time steps. A time step of 0.5 gives a steady result and a time step of 0.1 gives an unsteady result. The refinement study also revealed unsteady results for all time steps ≤ 0.1 .

Figure 3.33 revealed that both the frequency of oscillation and magnitude of shock movement is independent of the time step. The slight phase

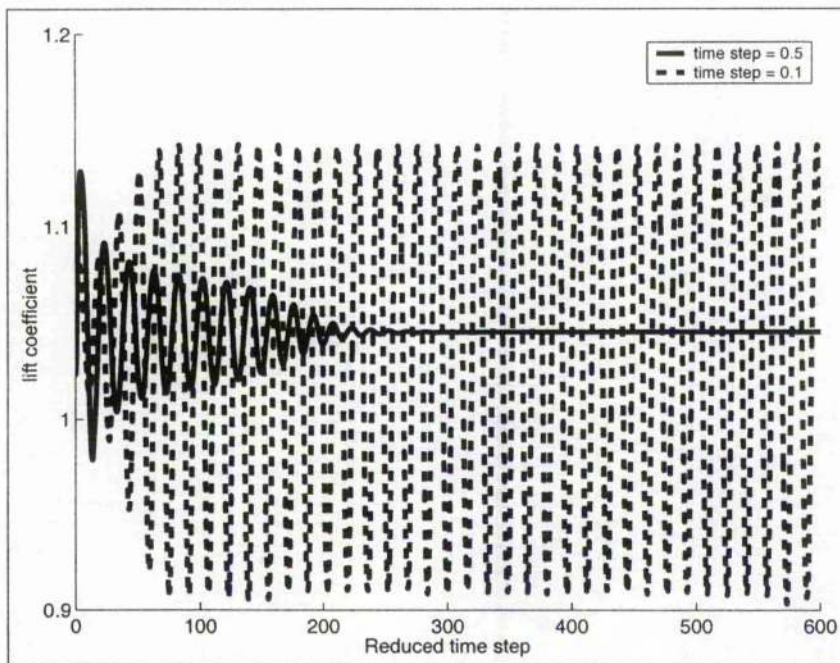


Figure 3.32: Lift coefficient plots using time steps of 0.1 and 0.5

difference in the lift is maybe due to slight difference in the steady solution upon entering the unsteady calculation.

The pressure intensity plots for different time steps can be seen in Figure 3.34. The shock position is correctly predicted for both time steps, the shock position is located at the maximum in the pressure intensity. It can be seen however that there is a difference in the prediction of the peak pressure intensity; computational results show a higher pressure intensity peak than experimental results. This higher pressure intensity peak may be due to a stronger shock and larger separation regions. Also notice that the experimental pressure intensity is almost constant at the trailing edge but it gradually increases in the computational results for both time steps; this is

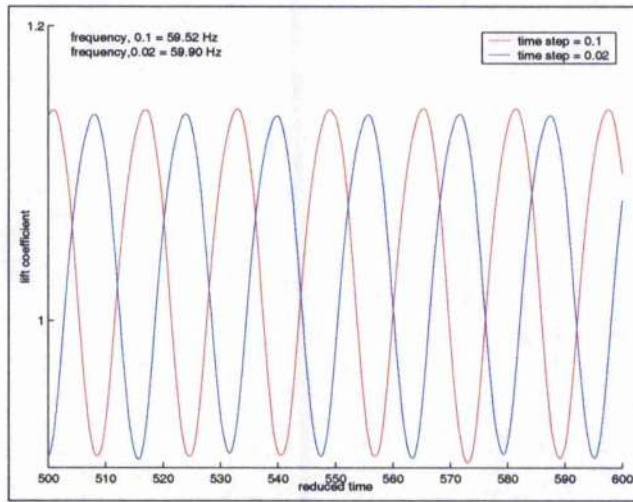


Figure 3.33: Lift coefficient plots using time steps of 0.1 and 0.02

because Lee observed attached flow at the trailing edge but calculations with the Baseline model give a separated flow.

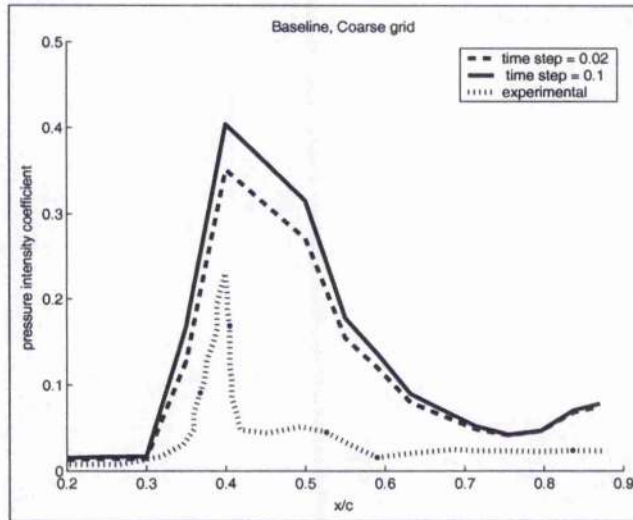


Figure 3.34: Pressure intensity plots using time steps of 0.1 and 0.02

A grid refinement study revealed that the characteristics of the shock

movement are heavily dependent on the grids employed. Figure 3.35 shows the shock movement for the three different grids used in this study. All the grid levels predicted the upstream and downstream shock movement that is expected, however the frequency of the shock oscillation decreases as the density of grid increases. Furthermore, a clear trend could not be seen between the magnitude of the shock movement and the grid density. The fine grid predicted larger shock movement than both the other grids. This may suggest that the magnitude of shock movement increases with grid density until a critical number of grid points is reached and then there is decrease in shock movement when grid points exceed this critical number of grid points. However, finer grids are needed in order to confirm this hypothesis.

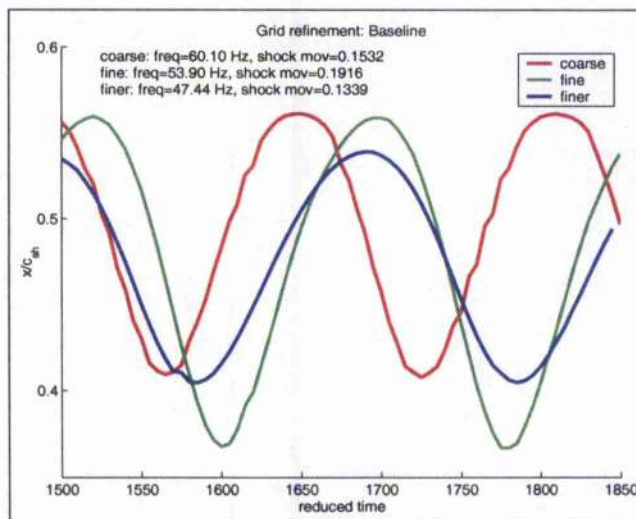


Figure 3.35: Shock movement using the three different grids at $\alpha = 4.905^\circ$

The temporal behaviour of the separation regions using the coarse and fine grids can be seen in Figures 3.36, 3.37 and Figures 3.39, 3.40. Figures

3.36 and 3.39 show an increase in the separation regions during the upstream movement of the shock and decrease during the downstream movement of the shock as illustrated in Figures 3.37 and 3.40. However, the fine grid seems to produce larger separation regions than the coarse grid. Both grids generate an interaction between the separation bubble and the trailing edge separation, hence producing an unsteady flow field.

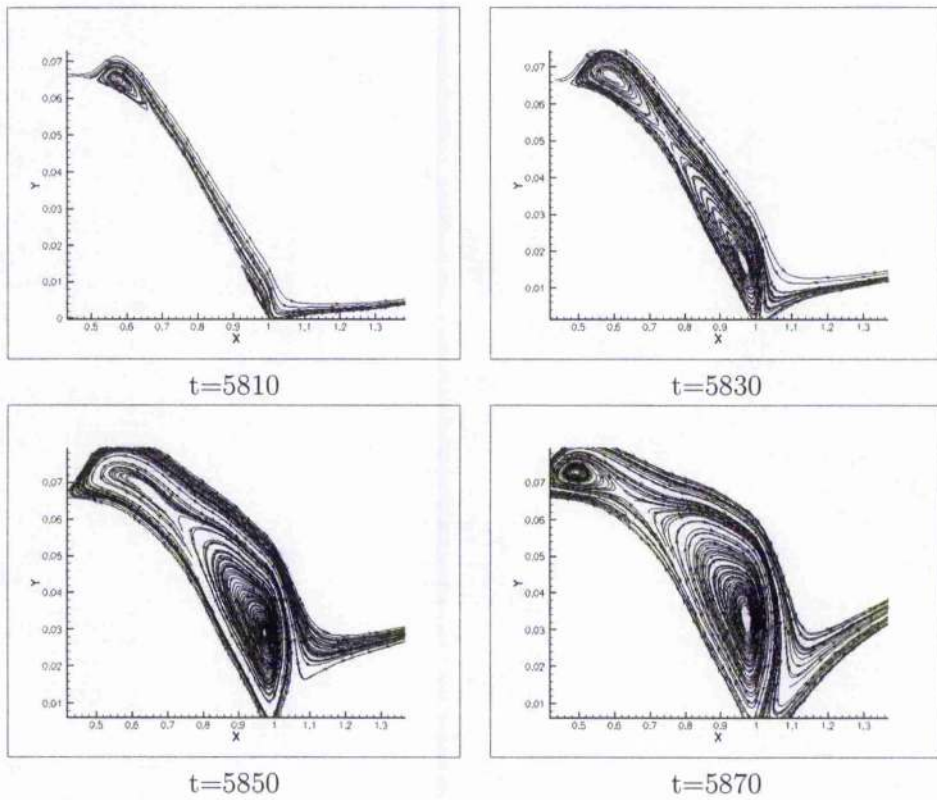


Figure 3.36: Temporal variation in separation regions during an upstream shock movement at $\alpha = 4.905^\circ$ using the Baseline model and the coarse grid.

Figure 3.38 shows the variations of pressure spectra at various probe lo-

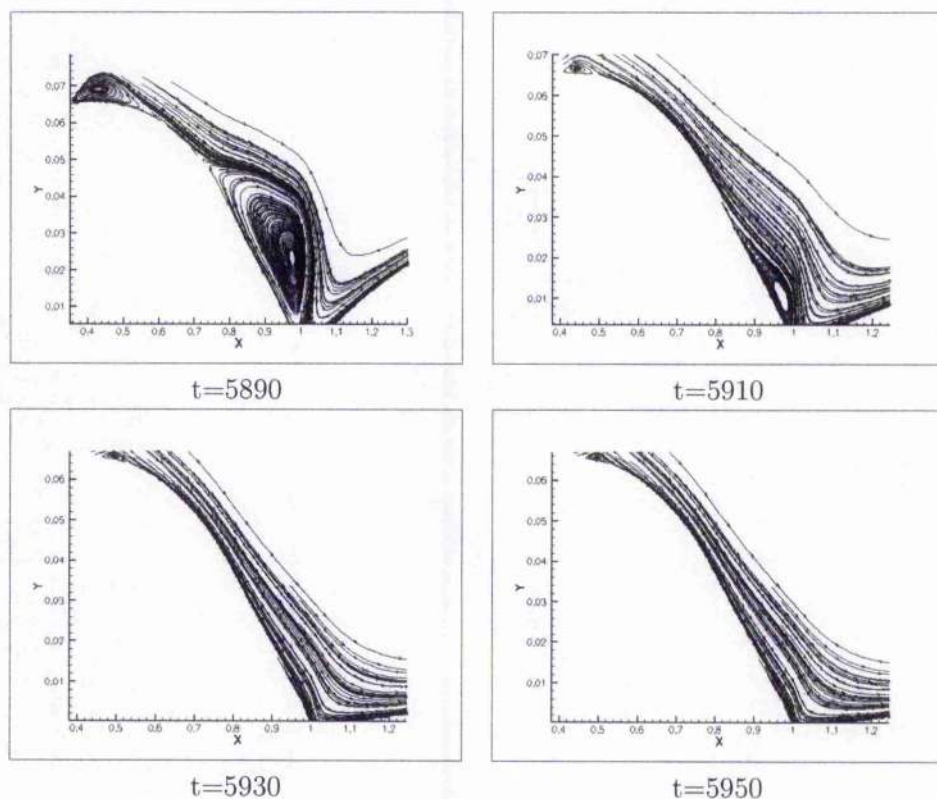


Figure 3.37: Temporal variation in separation regions during a downstream shock movement at $\alpha = 4.905^\circ$ using the Baseline model and the coarse grid.

cations for the Baseline model using the fine grid. This figure shows some significant differences from the pressure spectra for the coarse grid. A dominant frequency can now be seen at around 53 Hz at all probe locations. Only probe G is located before the shock and hence has lower pressures than the other probes. The fine grid produces a larger range of shock movement and a larger interaction zone than the coarse grid, this explains the higher levels in the pressure peaks for both probes I and K.

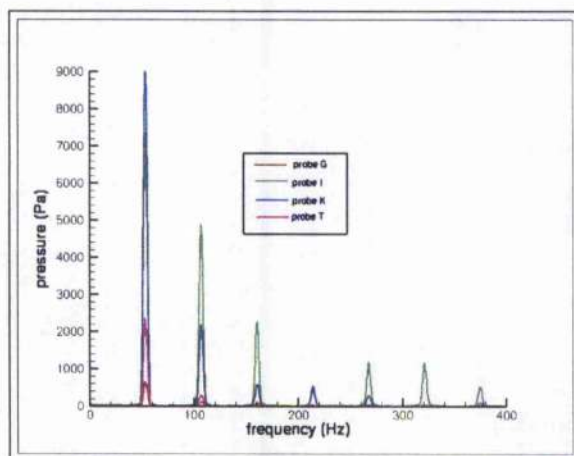


Figure 3.38: Pressure spectra plots at different probe locations for $\alpha = 4.905^\circ$ using the Baseline model and the fine grid

Another significant result obtained from the grid refinement study is the change in the flow field for the SST turbulence model as the grid point density is increased. However a further grid refinement study is needed to fully justify this hypothesis. The SST model produced a steady flow field with the coarse grid but produced unsteady results when the grid becomes finer. Figure 3.41 shows the shock movement for both the SST and Baseline models with time. The results were obtained using the fine grid. There is only a slight difference in the frequency of shock oscillation but a significant difference in the magnitude of shock movement. The magnitude of shock movement using the SST model is closer to Lee's experimental results than that of the Baseline model.

Figure 3.42 shows the variations of pressure spectra at various probe locations for the SST model using the fine grid. This figure shows some significant differences from the spectra for the baseline model. A dominant frequency

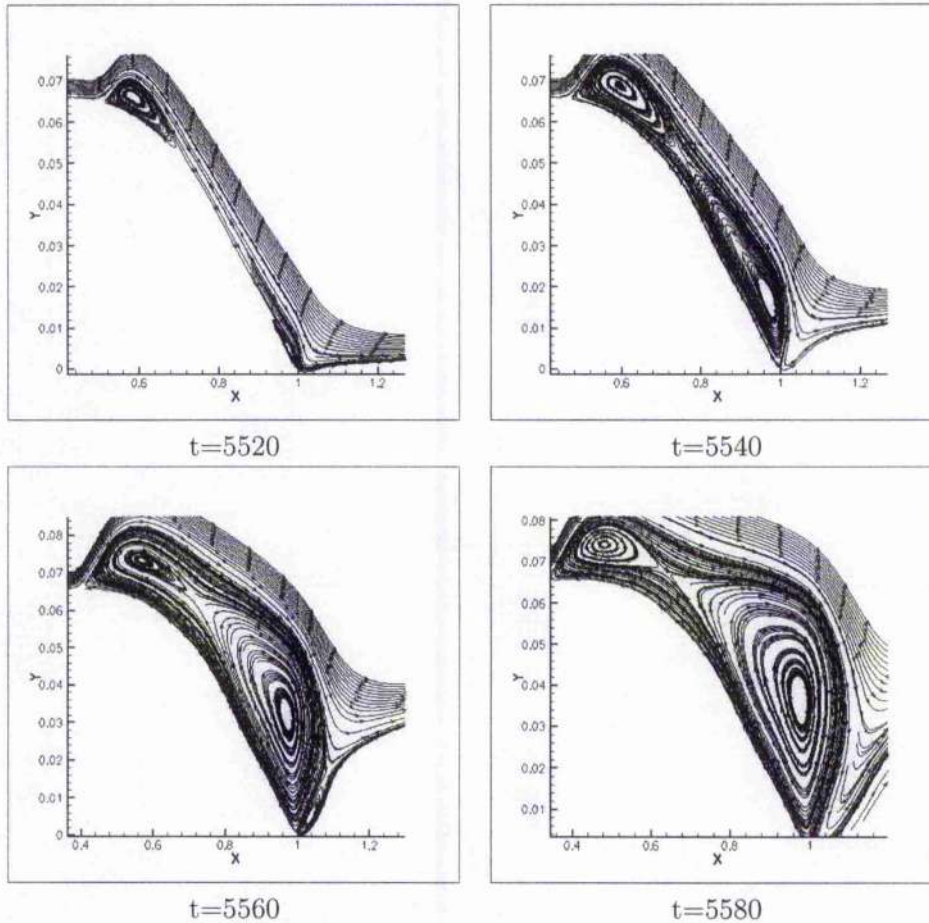


Figure 3.39: Temporal variation in separation regions during an upstream shock movement at $\alpha = 4.905^\circ$ using the Baseline model and the fine grid.

can now be seen at around 56 Hz. Both probes G and I are located before the shock hence have very low pressure peaks.

The temporal behaviour of the separation regions using the SST model and the fine grid can be seen in Figures 3.43 and 3.44. Similar to the Baseline model this figure shows an increase in the separation regions during the

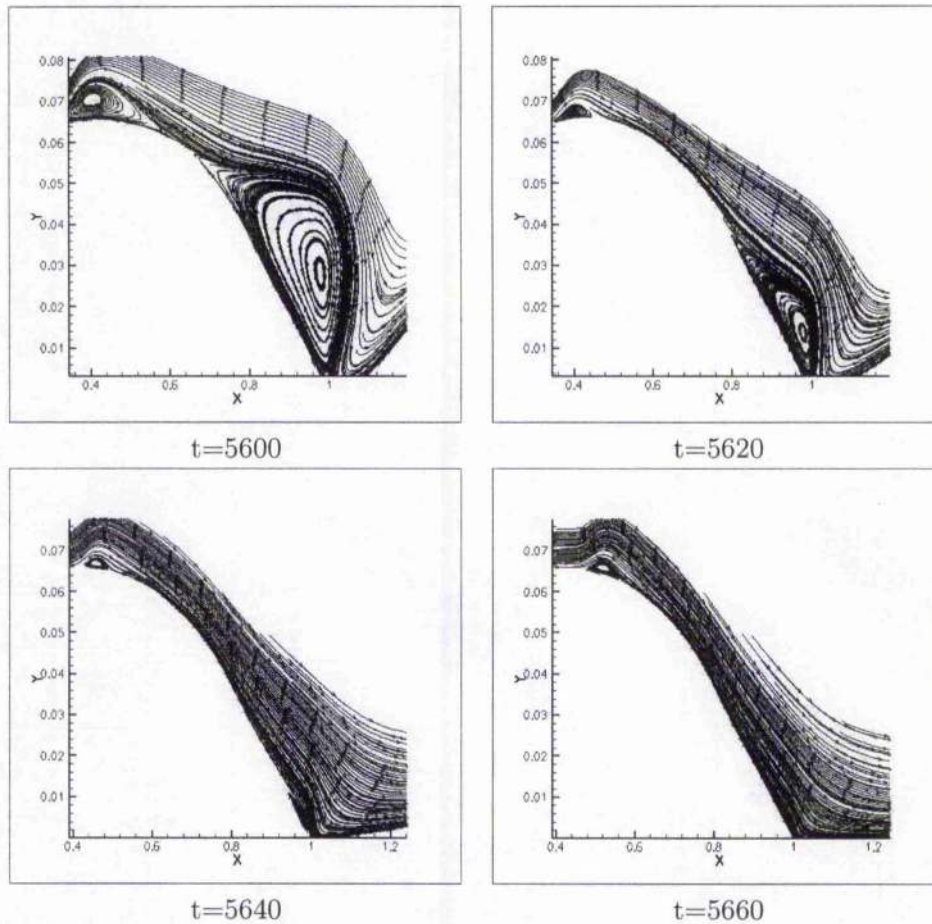


Figure 3.40: Temporal variation in separation regions during a downstream shock movement at $\alpha = 4.905^\circ$ using the Baseline model and the fine grid.

upstream movement of the shock and decrease during the downstream movement of the shock. However, notice that the separation regions are much smaller for the SST model than for the Baseline.

The frequency of shock oscillation is under-predicted for both models using the finer grid. The magnitude of shock movement is still over-predicted

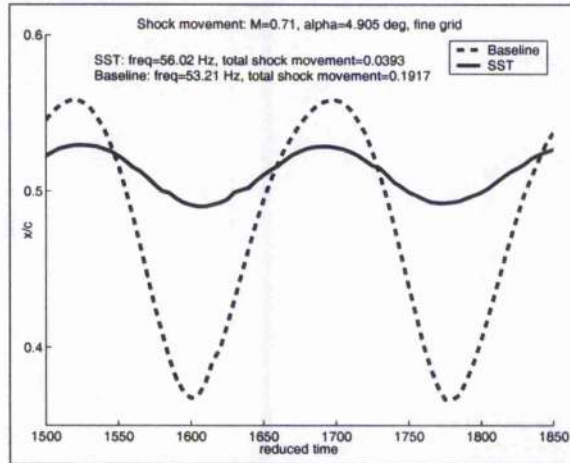


Figure 3.41: Shock movement using the SST and the Baseline models with the fine grid at $\alpha = 4.905^\circ$

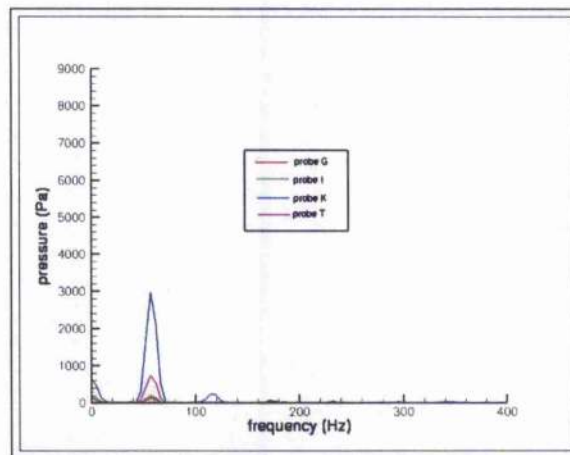


Figure 3.42: Pressure spectra plots at different probe locations for $\alpha = 4.905^\circ$ using the SST model and the fine grid

by the Baseline model but under-predicted by the SST model, see Figure 3.45.

The behaviour of the shock movement using the fine grid was compared with that of the finer grid, (see Figure 3.46) using the SST model. The fine grid produced a larger shock movement than the finer grid; the frequency

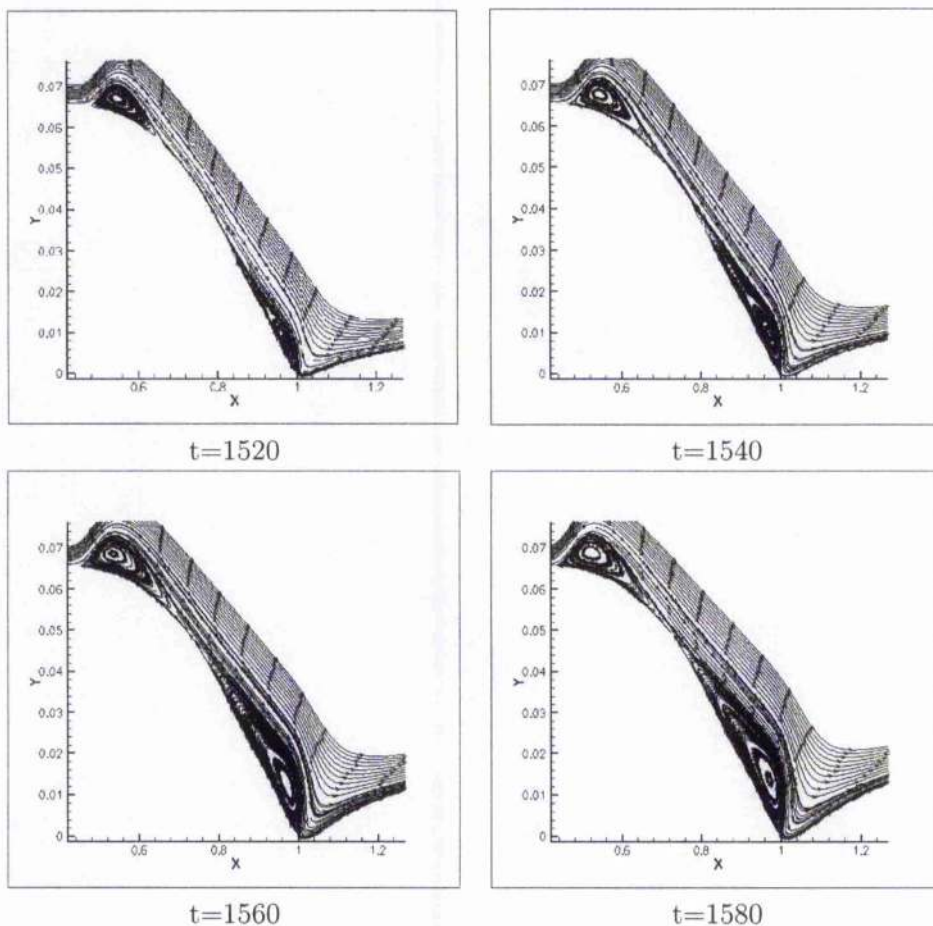


Figure 3.43: Temporal variation in separation regions during an upstream shock movement at $\alpha = 4.905^\circ$ using the SST model and the fine grid.

of the shock oscillation decreases with grid point density. The results are similar to those obtained using the Baseline model.

Shock height and trailing edge displacement thickness are also effected by grid resolution. Figure 3.47 shows that the fine grid produced a larger range of shock height than the other two grid levels. There is also larger shock

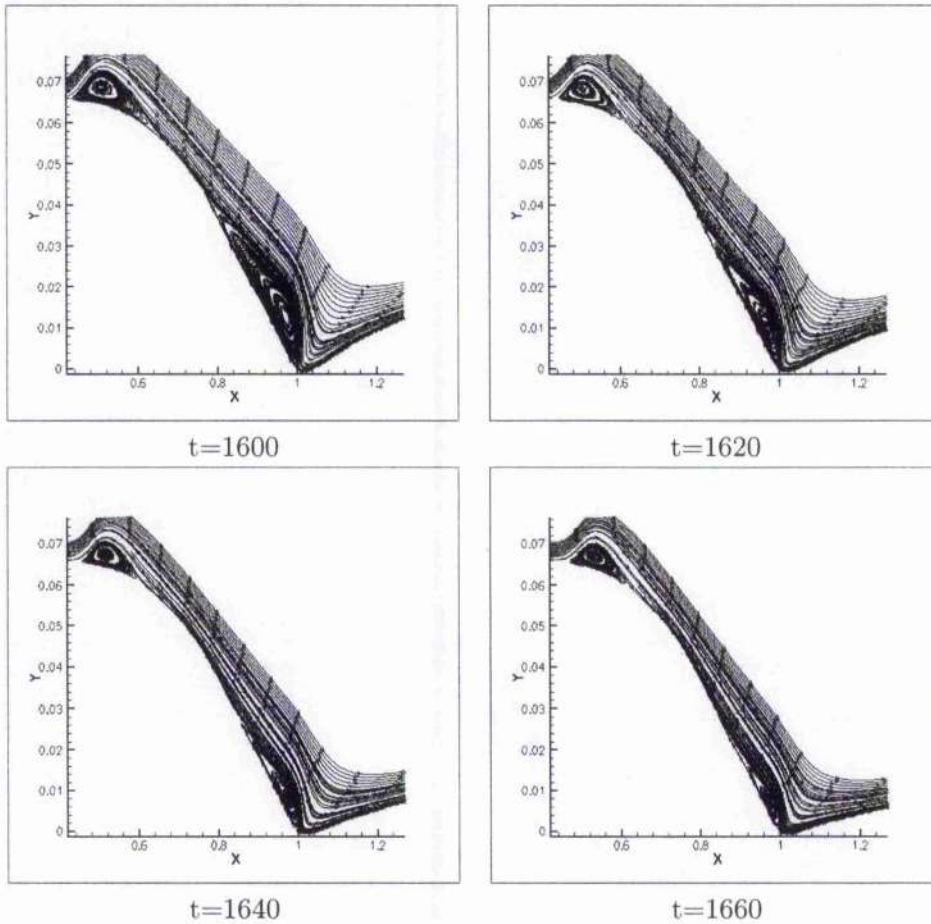


Figure 3.44: Temporal variation in separation regions during a downstream shock movement at $\alpha = 4.905^\circ$ using the SST model and the fine grid.

movement as discussed earlier.

The effect of grid resolution on the trailing edge displacement thickness can also be seen in Figure 3.48. The fine grid generated the thickest boundary layer.

The differences between the Baseline and the SST models can be further

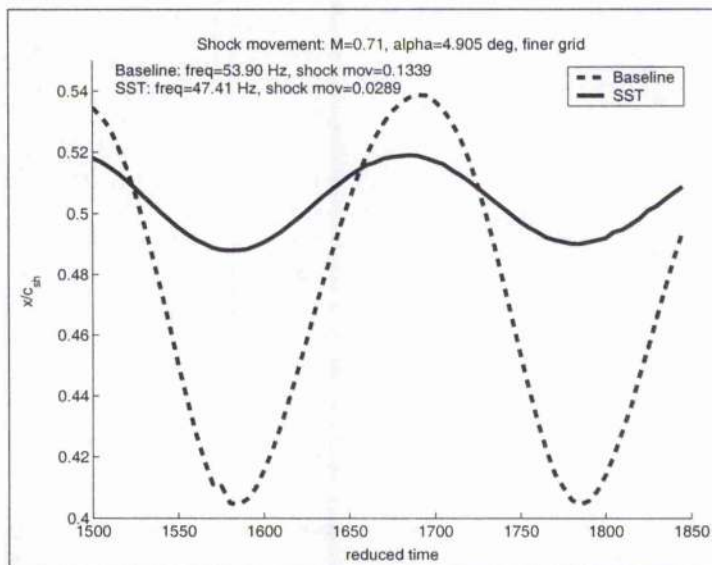


Figure 3.45: Shock movement using the SST and the Baseline models with the finer grid at $\alpha = 4.905^\circ$

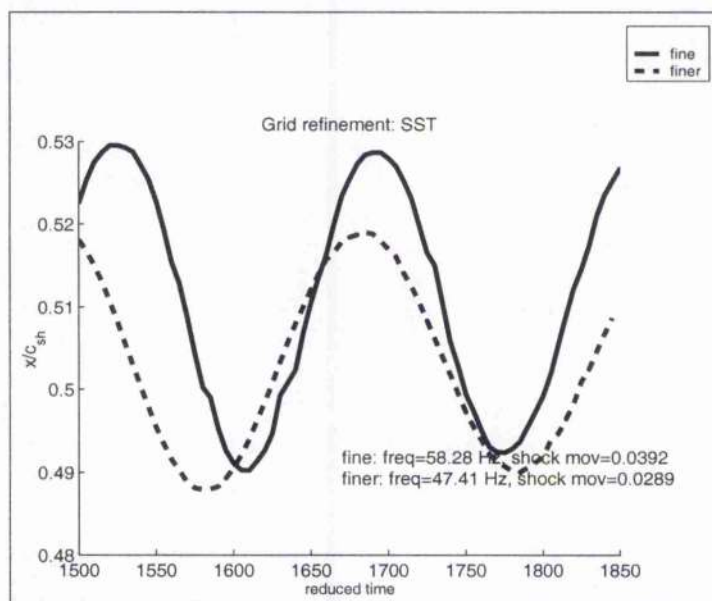


Figure 3.46: Shock movement using the SST model at $\alpha = 4.905^\circ$

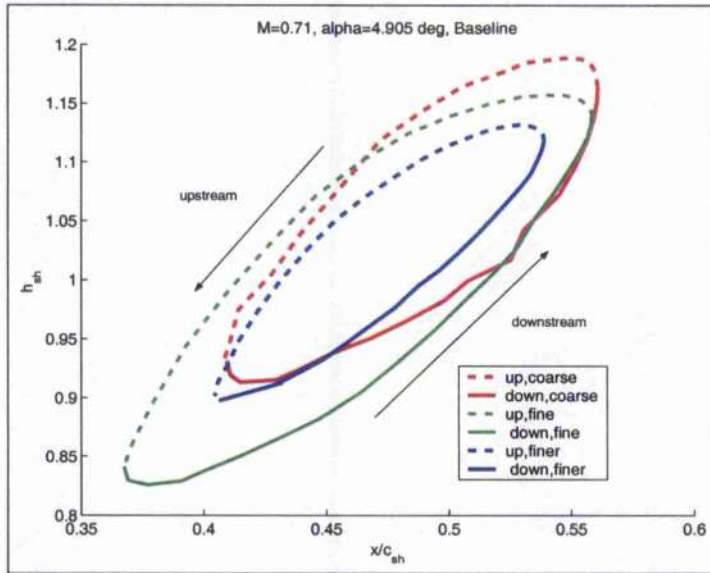


Figure 3.47: Shock height using different grids

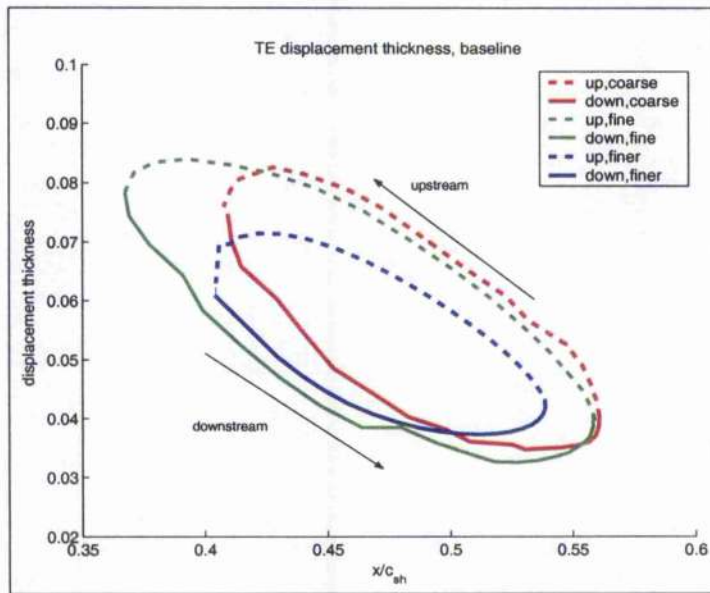


Figure 3.48: Trailing edge displacement thickness with different grids at $\alpha = 4.905^\circ$

discussed by considering the shock height and trailing edge displacement thickness plots using the fine grids. Figure 3.49 shows the shock strength plots for both models. It can be clearly seen that the Baseline model produces a larger range of shock height and also a larger range of shock movement.

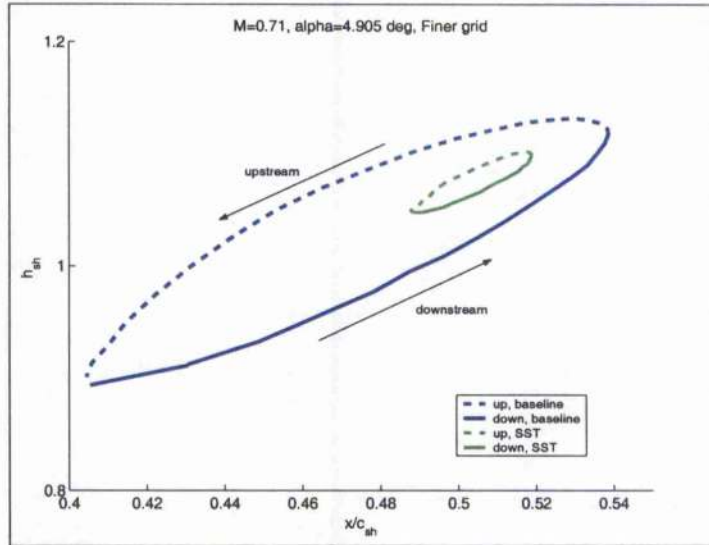


Figure 3.49: Shock height related to shock movement for the Baseline and SST models at $\alpha = 4.905^\circ$

The trailing edge displacement thickness plots also revealed that the Baseline model generates thicker trailing edge boundary layers than the SST model, see Figure 3.50.

Figure 3.51 shows the effect of grid resolution on the pressure intensity, using the Baseline model. Both the coarse and fine grids over-predicted the pressure intensities. The fine grid gives a higher pressure peak than the coarse grid. However, both grids gave a good prediction of the shock position. Notice that the experimental results show a slight hump in the pressure intensity after the shock, this hump is due to the separation bubble

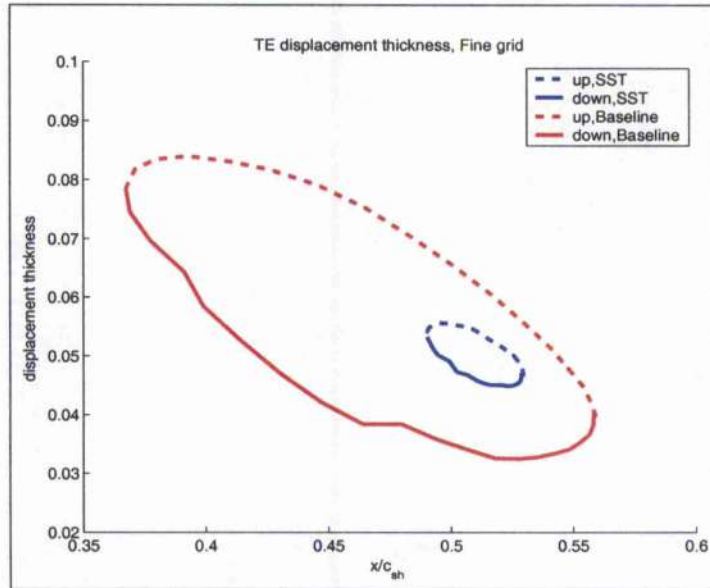


Figure 3.50: Trailing edge displacement thickness related to shock movement for the Baseline and SST models at $\alpha = 4.905^\circ$

after the shock. Both grids failed to predict this hump.

Figure 3.52 demonstrates another difference between the SST and the Baseline model. The SST model failed to exactly predict the position of the pressure peak, this is because the SST never predicted the correct shock position in the steady computations. The Baseline model produced a higher pressure peak than the SST, this may be because of the larger range of shock strength and the larger shock movement. Also notice that the Baseline gave higher pressure intensities towards the trailing edge than the SST, reason being that the Baseline generated a thicker displacement thickness at the trailing edge than the SST.

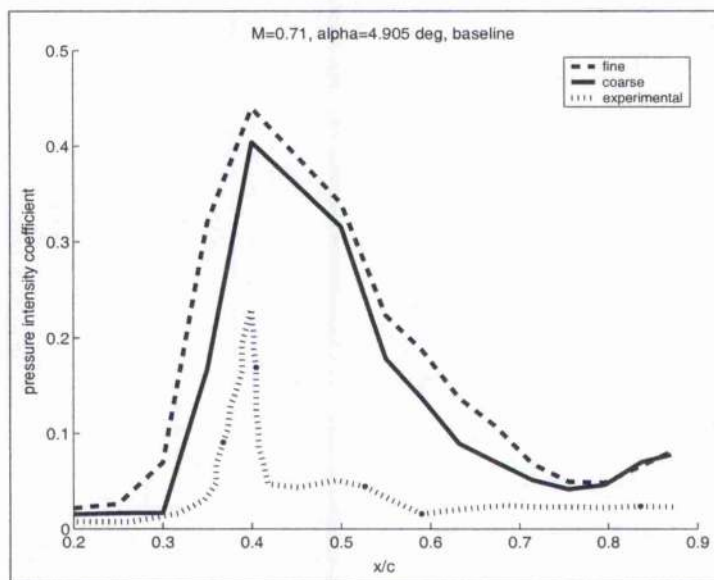


Figure 3.51: Pressure intensities for the Baseline model using two different grid levels at $\alpha = 4.905^\circ$

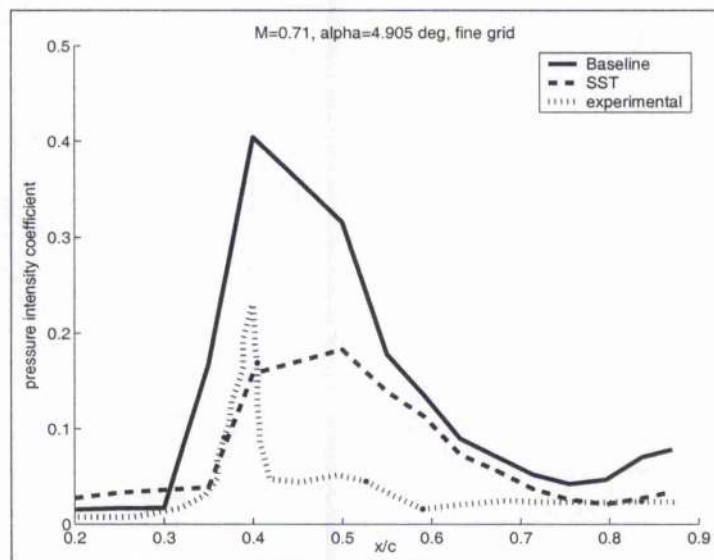


Figure 3.52: Pressure intensities for the Baseline and SST models using the fine grid at $\alpha = 4.905^\circ$

3.1.4 Unsteadiness due to employed turbulence models

A comparison of the turbulence Reynolds stresses may give an explanation into why the SST and the Baseline model gave an unsteady flow field whilst the $k-\omega$ didn't. Figures 3.53, 3.54 and 3.55 show the Reynolds turbulence stresses at different positions on the upper surface for the different turbulence models. These stresses were calculated using the following relationships:

$$\tau_{xy} = \mu_T \left(\frac{\partial u}{\partial y} + \frac{\partial v}{\partial x} \right)$$

$$\tau_{xx} = \mu_T \left(\frac{4}{3} \frac{\partial u}{\partial x} - \frac{2}{3} \frac{\partial v}{\partial y} - \frac{2}{3} \frac{\partial w}{\partial z} \right) - \frac{2}{3} \rho k$$

$$\tau_{yy} = \mu_T \left(-\frac{2}{3} \frac{\partial u}{\partial x} + \frac{4}{3} \frac{\partial v}{\partial y} - \frac{2}{3} \frac{\partial w}{\partial z} \right) - \frac{2}{3} \rho k$$

There are clear differences in the behaviour of the turbulent stresses along the upper surface of the aerofoil for the different turbulence models. These figures show that the stress levels for the $k-\omega$ model gradually decrease as the shock is approached followed by an increase after the shock. For the Baseline model, there is a gradual increase in the stresses as the shock is approached but this is followed by a drastic increase after the shock. However the opposite happens for the SST model, there being a gradual decrease in the stress levels as the trailing edge is approached. This decrease in stress levels for the SST model may be responsible for the smaller shock movement discussed earlier.

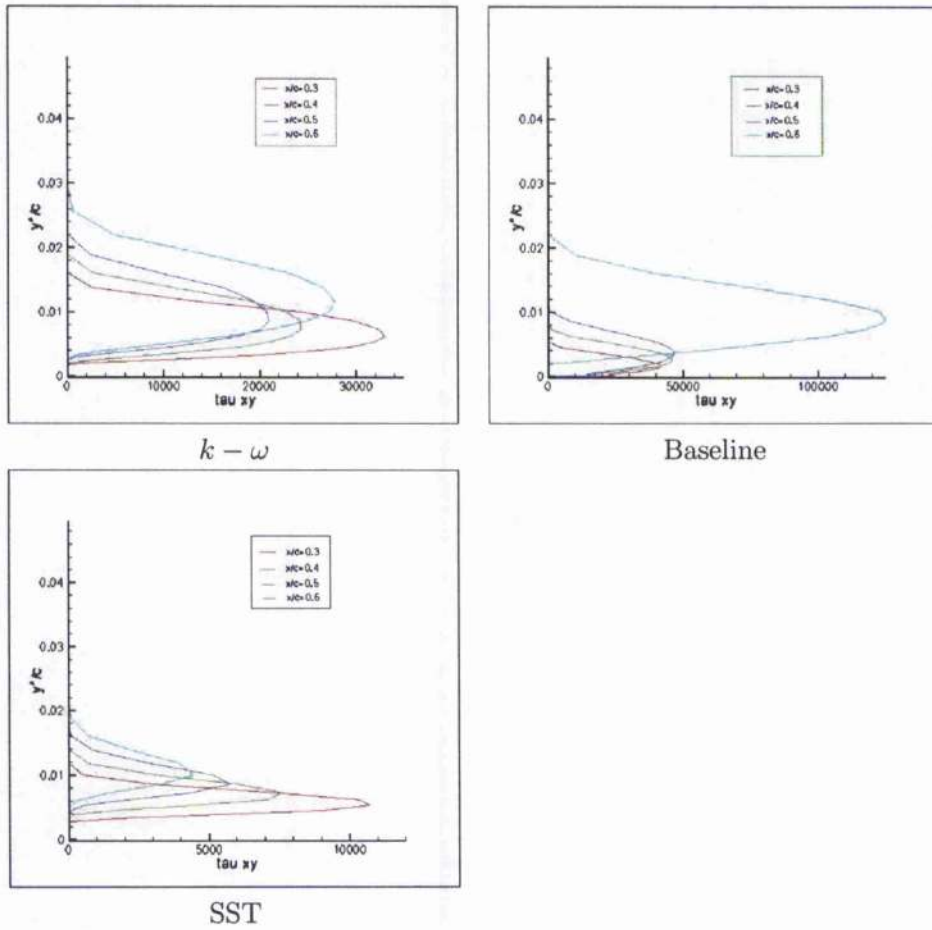


Figure 3.53: Reynolds turbulence stress, τ_{xy} profiles along the upper surface for three different turbulence models, $M=0.71$ and $\alpha=4.905^\circ$

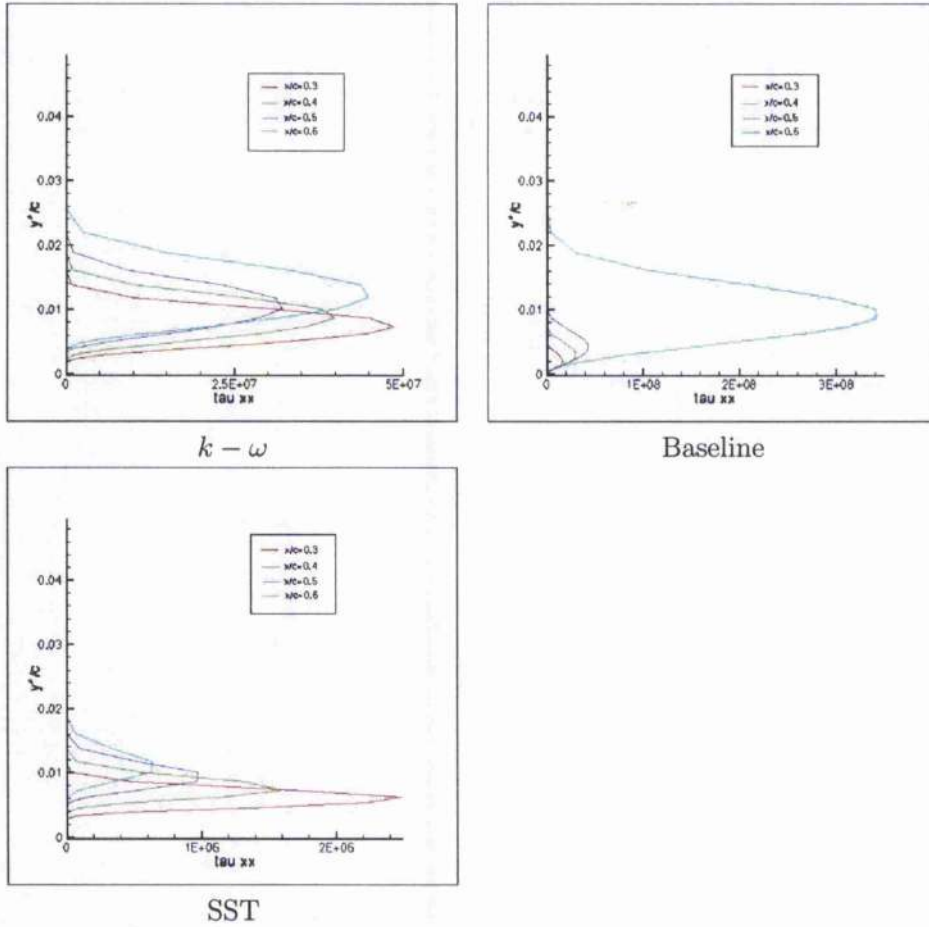


Figure 3.54: Reynolds turbulence stress, τ_{xx} profiles along the upper surface for three different turbulence models, $M=0.71$ and $\alpha=4.905^\circ$

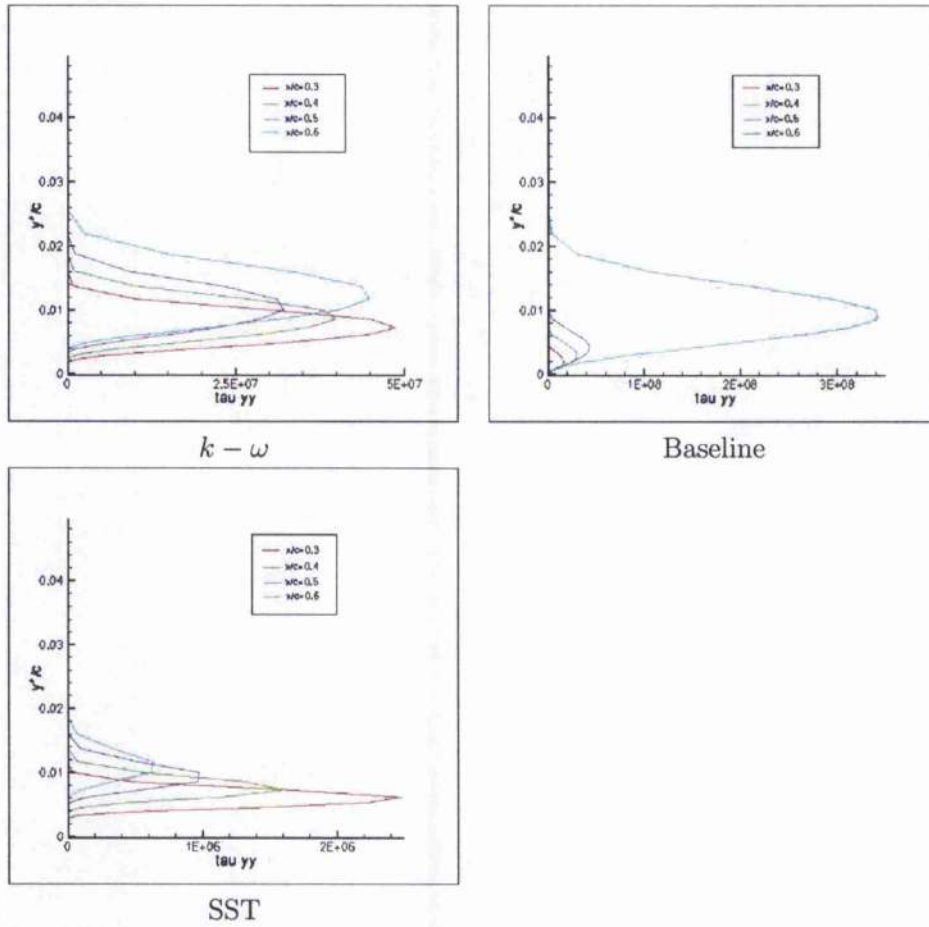


Figure 3.55: Reynolds turbulence stress, τ_{yy} profiles along the upper surface for three different turbulence models, $M=0.71$ and $\alpha=4.905^\circ$

3.2 OAT15A Aerofoil

3.2.1 Unsteadiness due to change in angle of attack

Results obtained from test case 2 will be used to explain why buffet occurs at a certain angle of attack but steady flow is observed at lower angles of attack. A comparison of certain flow field properties will reveal the behaviour of the separation region and also a significant change in some of the steady flow field properties as the angle of attack is increased and hence leading to a buffet flow field. The flow properties at two angles of attack will be looked at in detail, 3° and 3.5° . There is a steady flow field at 3° and an unsteady flow field at 3.5° , see Figure 3.56. This suggests that buffet occurs at an angle of attack between 3° and 3.5° ; this is consistent with experimental findings at ONERA, where buffet first occurred at 3.25° .

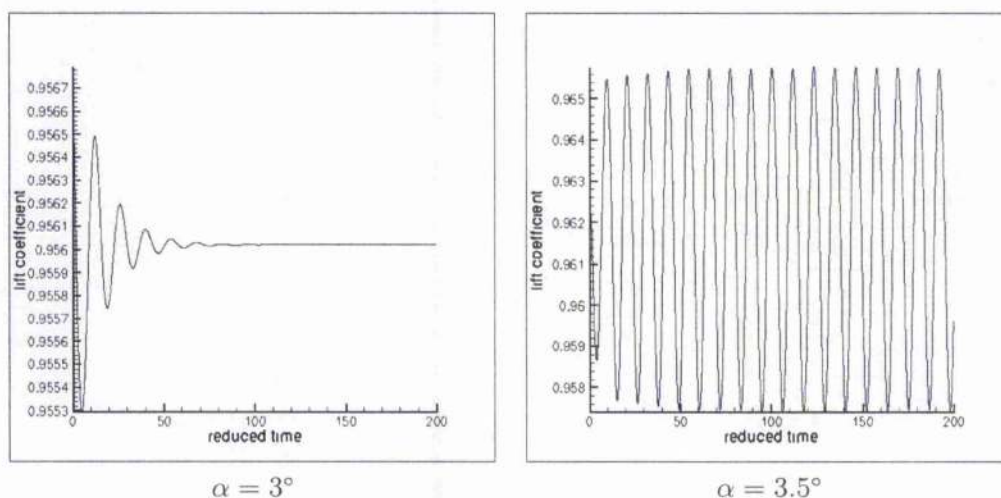


Figure 3.56: Lift coefficient plots at two different angles of attacks for $M = 0.73$ and $Re = 3 \times 10^6$

As the angle of attack increases, the shock becomes stronger. The stronger shock leads to a larger separation region. At $\alpha = 2.5^\circ$, there is a small separation bubble present at the foot of the shock followed by a region of attached flow, (see Figure 3.57). This result qualitatively is in good agreement with experimental findings.

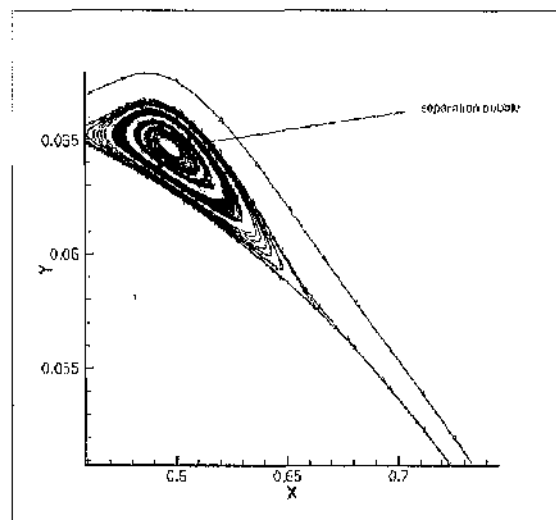


Figure 3.57: Streamlines indicating a separation bubble at $\alpha=2.5^\circ$

At $\alpha = 3^\circ$, the shock becomes stronger, a larger separation bubble is formed and there is also an emergence of trailing edge separation (see Figure 3.58).

At $\alpha = 3.5^\circ$, the shock continues to become stronger, a larger separation bubble is formed at the foot of the shock signalling a larger trailing edge separation. However, the circulation from the bubble now reaches the circulation from the trailing edge, (see Figure 3.59).

When α is increased further to 3.91° there are formations of larger separation regions caused by the stronger shock. There is more evidence of the

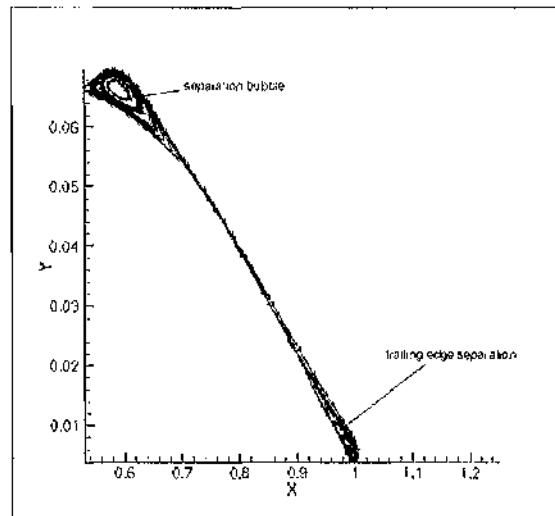


Figure 3.58: Streamlines indicating a separation bubble and trailing edge separation at $\alpha=3^\circ$

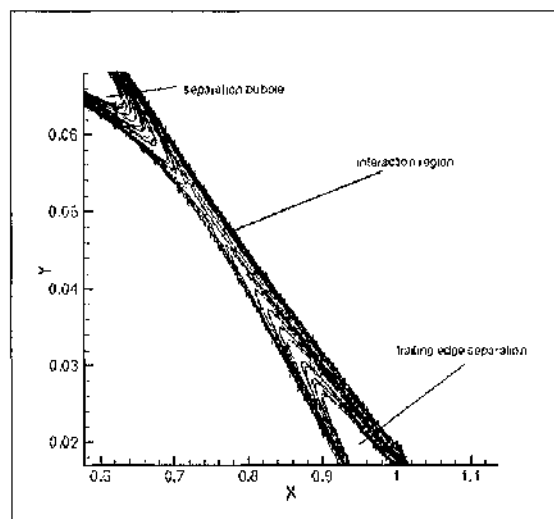


Figure 3.59: Streamlines indicating a separation bubble, trailing edge separation and an interaction region between the circulation regions at $\alpha=3.5^\circ$

two circulation regions interacting with each other, (in Figure 3.60).

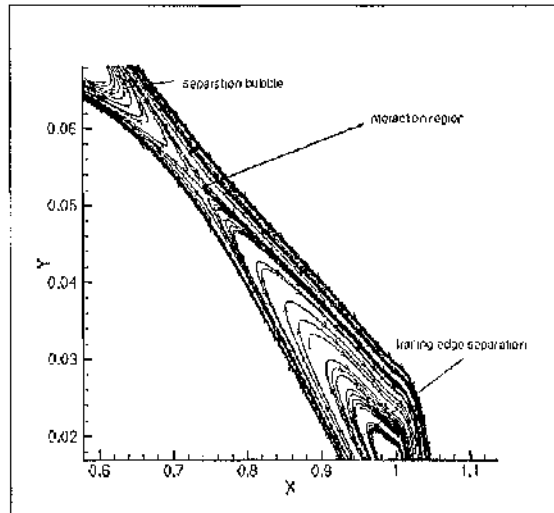


Figure 3.60: Streamlines indicating a separation bubble, trailing edge separation and an interaction region between the circulation regions at $\alpha=3.91^\circ$

It seems like the necessary condition for a buffet flow field is the communication between circulations of the separation bubble and that of the trailing edge separation. The larger these separation regions are the heavier the buffet intensity. At even larger angles of attack, these separation regions merge to become one large separation region extending from the foot of the shock to beyond the trailing edge. For these, a heavier buffet intensity is observed.

Figure 3.61 compares the convergence of levels of angles of attack 3° and 3.5° using the coarse grid. Note that this convergence plot is only for the steady part of the calculations. The maximum error in the calculations of the mean and turbulence equations is used as an indicator of convergence. One

can notice that for the higher angle of attack there are larger fluctuations in the errors of both the mean and turbulent properties than for the lower angle of attack. This may be due to the larger separation region at the higher angle of attack.

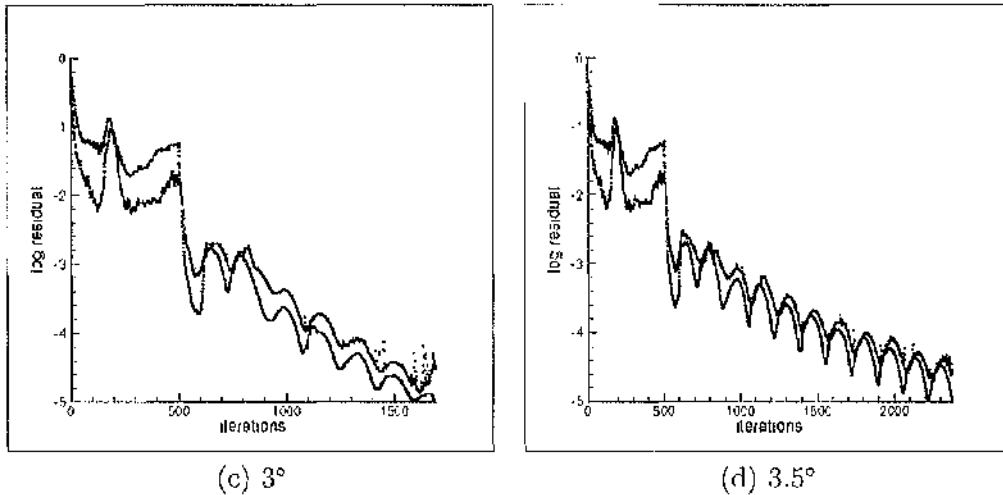


Figure 3.61: Residual plots at two different angles of attack, $M = 0.73$ and $Re = 3 \times 10^6$

This difference in separation region gives rise to different levels of turbulence flow properties. Figures 3.62 and 3.63 demonstrate that the level of the average turbulence Reynolds number increases as the angle of attack increases from 3° to 3.5° . One can also notice that the size of the separation bubble also increases considerably in size. This increase in the size of the separation region from 3° to 3.5° and the resulting rise in the average turbulence Reynolds number at 3.5° is due to the interaction between the two circulation regions. This finding is also true for the trailing edge separation.

Figure 3.64 is a plot of the turbulence Reynolds number at different points

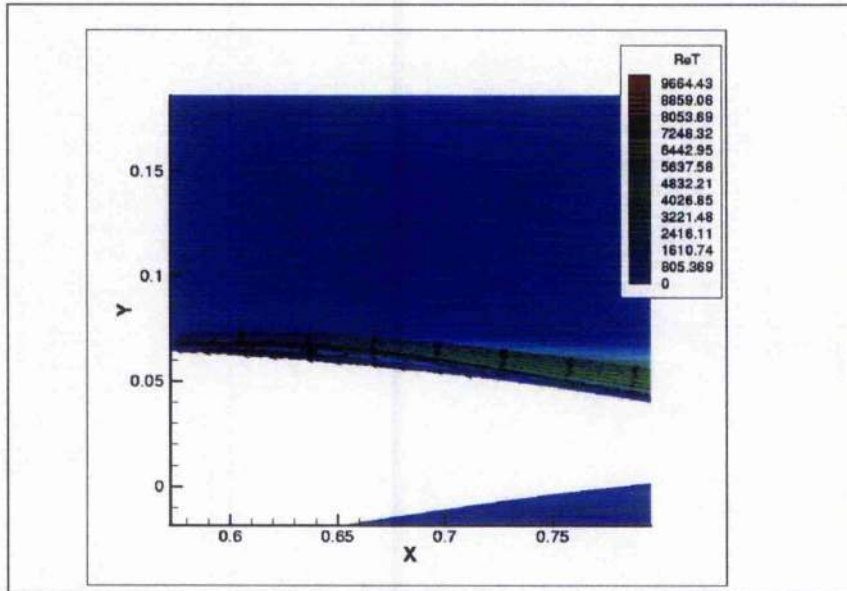


Figure 3.62: Re_t contours at the separation bubble, $M = 0.73$, $Re = 3 \times 10^6$ and 3°

on the upper surface. There is a gradual increase in the turbulence Reynolds number as the distance away from the shock increases. However, there are higher turbulence Reynolds numbers at an angle of attack of 3.5° than at 3° within the separation regions.

Other useful properties to quantify the levels of turbulence in the steady flow fields are the turbulence Reynolds shear and normal stresses. These stresses arise due to the velocity fluctuations in a turbulent flow. Figures 3.65, 3.66 and 3.67 show plots of the Reynolds shear and normal stresses along the upper surface of the aerofoil.

Figure 3.68 indicates the levels of turbulence Reynolds normal stresses generated at the blunt trailing edge. In the figure, x_0 is distance away from the trailing edge. Again higher levels of normal stresses are generated in the

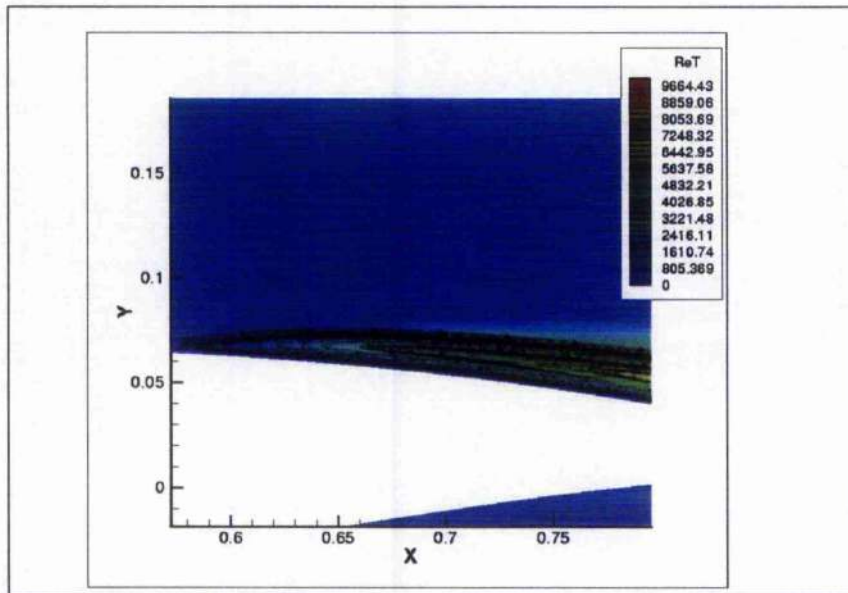


Figure 3.63: Re_t contours at the separation bubble, $M = 0.73$, $Re = 3 \times 10^6$ and 3.5°

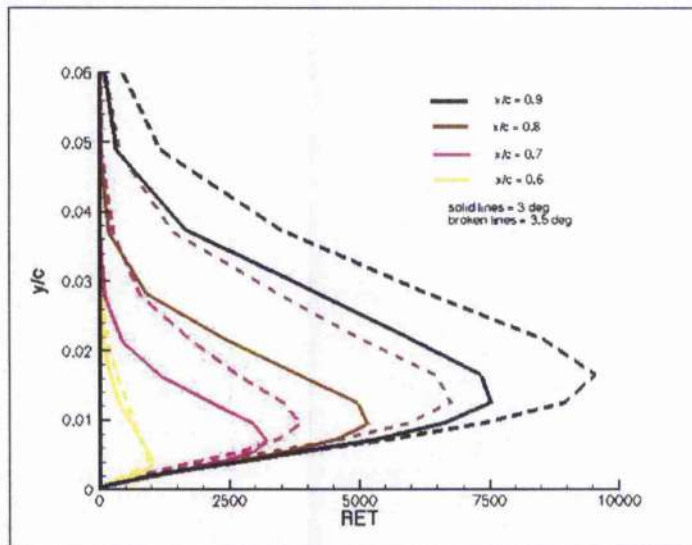


Figure 3.64: Turbulent Reynolds number plot along the upper surface for 3 and 3.5 deg.

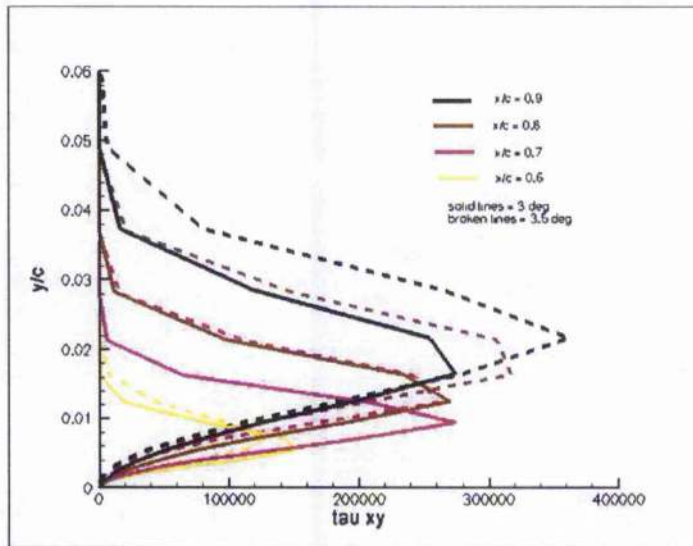


Figure 3.65: Turbulent Shear stress, τ_{xy} plots along the upper surface for 3 and 3.5 deg.

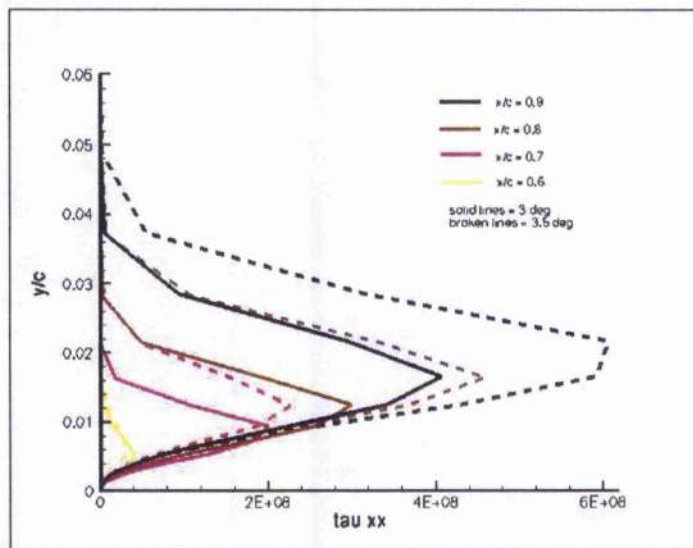


Figure 3.66: Turbulent x-normal stress, τ_{xx} plots along the upper surface for 3 and 3.5 deg.

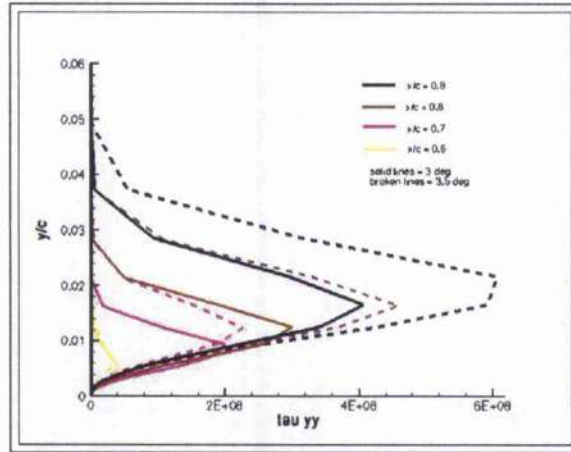


Figure 3.67: Turbulent y -normal stress, τ_{yy} plots along the upper surface for 3 and 3.5 deg.

wake at 3.5°, indicating a more turbulent flow at that angle of attack.

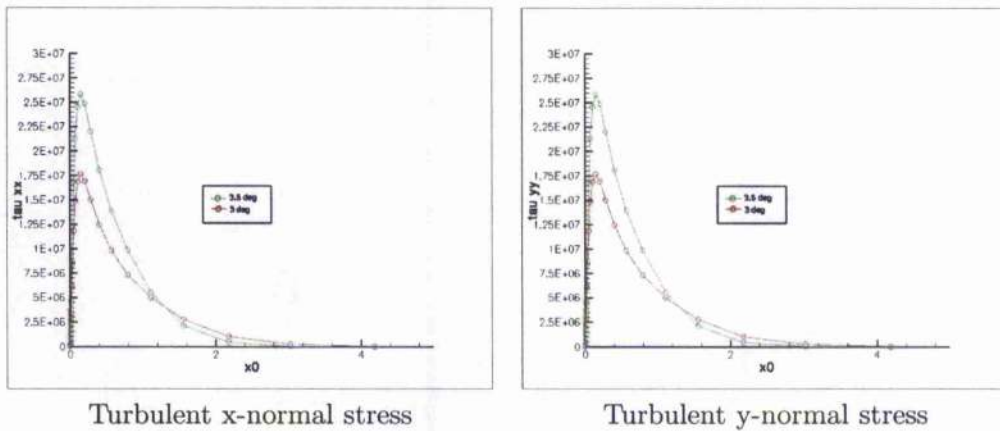


Figure 3.68: Normal stress profiles in the wake for two different angles of attack, $M = 0.73$ and $Re = 3 \times 10^6$

The temporal behaviour of the separation regions at $\alpha=3^\circ$ and $\alpha=3.91^\circ$ can be seen in Figures 3.69, 3.70 and Figures 3.71, 3.72. There isn't any change in the separation regions as time increases for $\alpha=3^\circ$. Both separation

regions remain stationary, preventing any interaction between the separation bubble and the trailing edge separation and hence the flow field is steady (see Figures 3.69 and 3.70). However at $\alpha=3.91^\circ$, there is a slight change in the size and location of these separation regions caused by the shock movement. Figure 3.71 shows a slight increase in both the separation bubble and the trailing edge separation during the upstream movement of the shock and Figure 3.72 shows a slight decrease during the downstream movement.

3.2.2 Unsteadiness due to grid refinement

Pressure intensities obtained using the two grid levels were compared with computations done at ONERA. Figure 3.73 shows that the peak pressure intensities are under-predicted on both grid levels for an angle of attack of 4.5 deg. However, this peak pressure intensity is greatly improved by increasing the grid point density and the position of the peak pressure intensity over the upper surface is improved with the fine grid.

The reason for the higher peak pressures for the ONERA computations can be clearly seen in Figure 3.74, the shock movement is for the coarse grid, ONERA predicted a larger shock movement and hence higher pressure peaks. Both grids gave a reasonable agreement in pressures before the shock position.

There is a large difference in the peak pressure intensities between the two grids when the angle of attack is increased to 5° and 5.5° , Figures 3.75 and 3.76 respectively. The above observation at an angle of attack of 4.5 deg is also consistent for the two latter angles of attack.

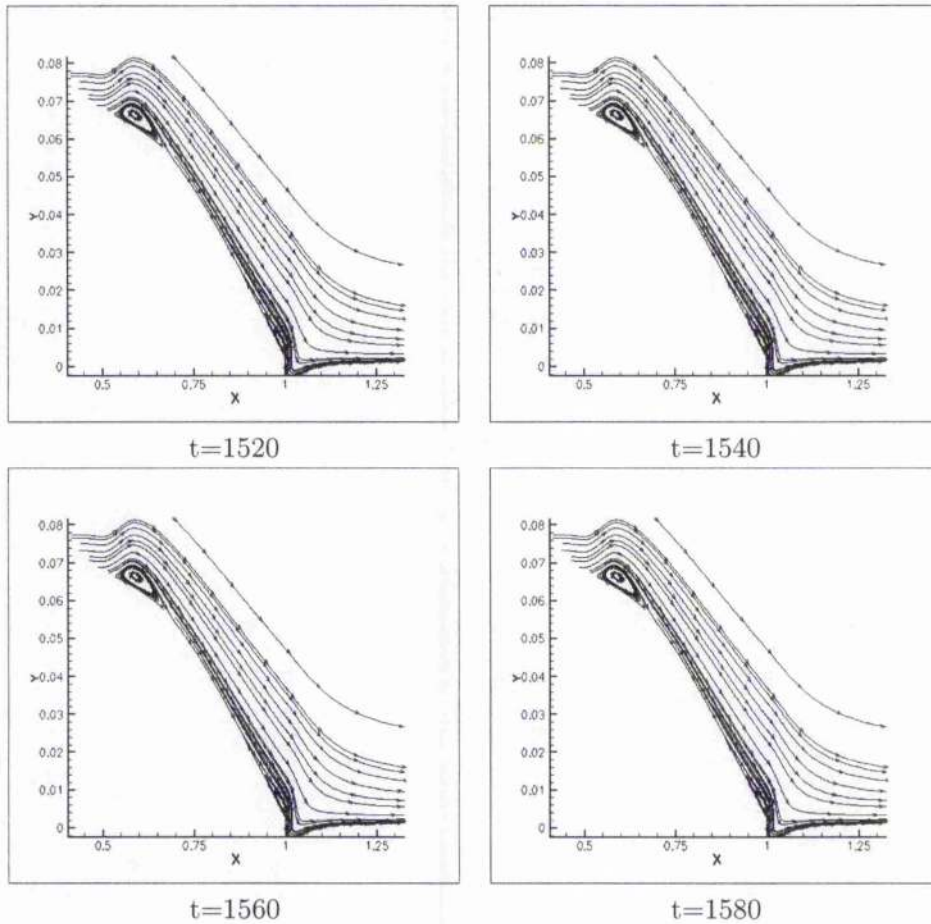


Figure 3.69: Temporal variation in separation regions during an upstream shock movement at $\alpha = 3.0^\circ$ using the Baseline model and the coarse grid.

The temporal behaviour of the separation regions using the fine grid at an angle of attack of 3.91° can be seen in Figures 3.77 and 3.78. This figure shows a buffet flow field as there is an interaction between the bubble and the trailing edge separation. However, the fine grid seems to produce larger separation regions than the coarse grid (Figures 3.71 and 3.72) and hence

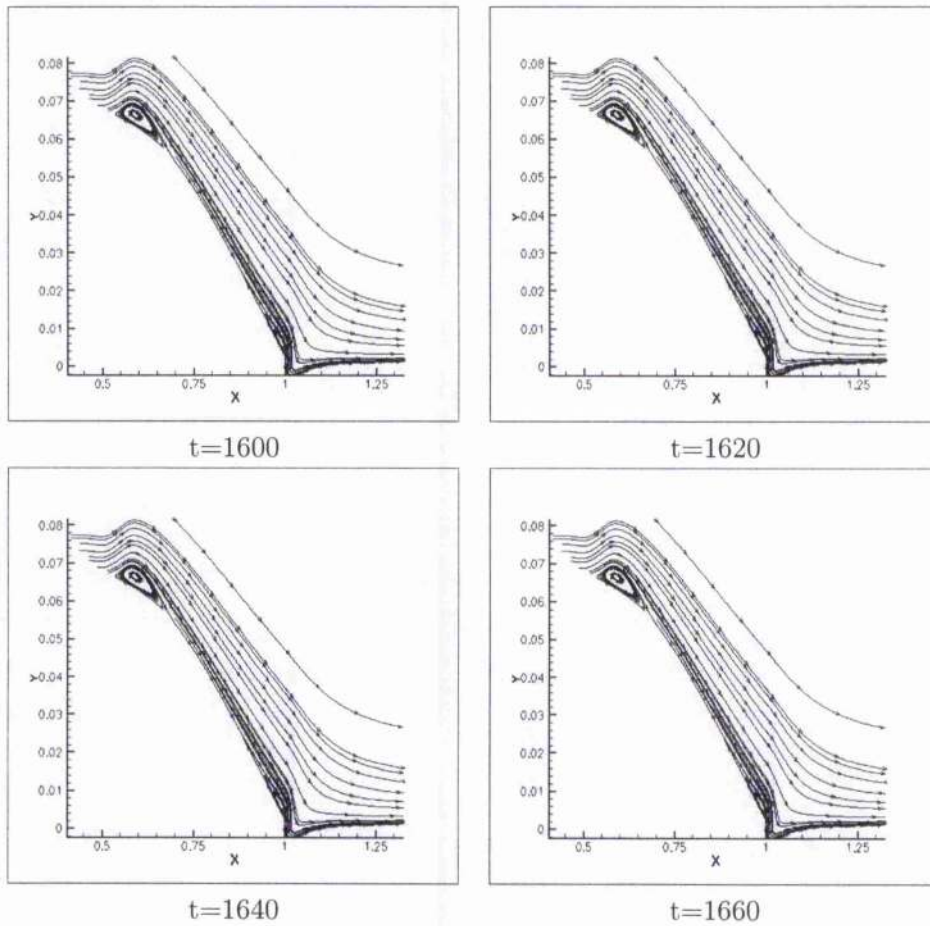


Figure 3.70: Temporal variation in separation regions during a downstream shock movement at $\alpha = 3.0^\circ$ using the Baseline model and the coarse grid.

the finer grid produces a higher buffet intensity.

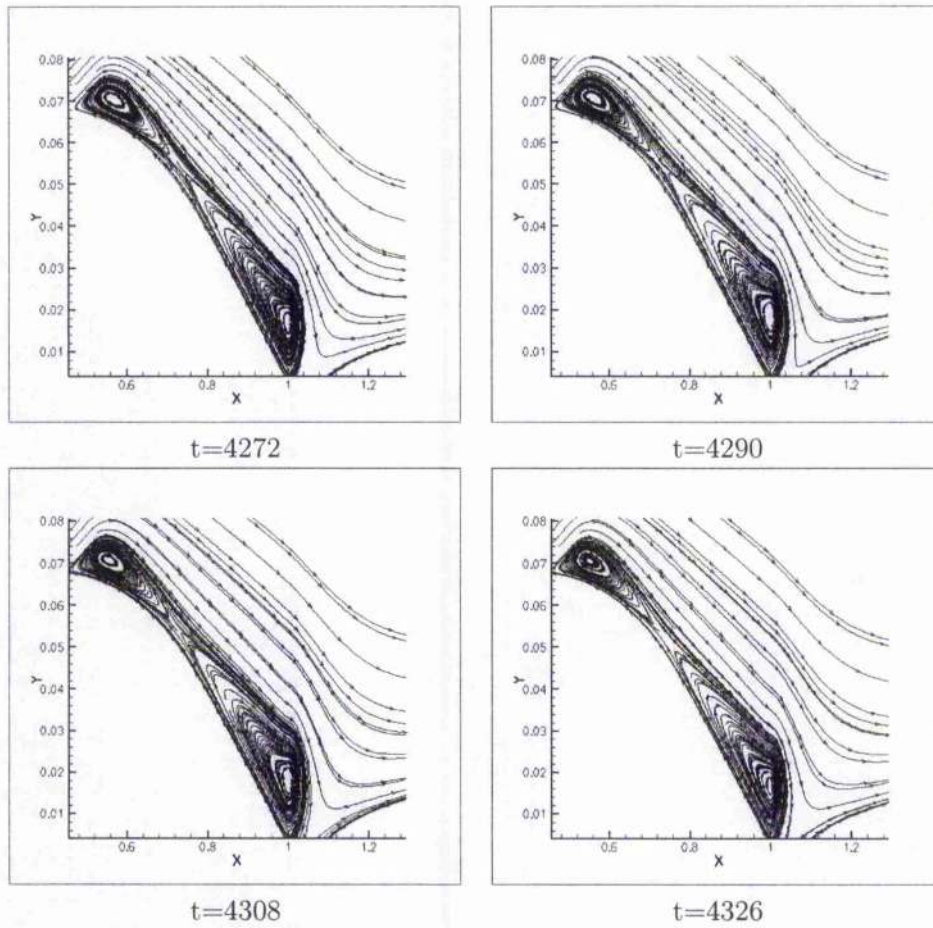


Figure 3.71: Temporal variation in separation regions during an upstream shock movement at $\alpha = 3.91^\circ$ using the Baseline model and the coarse grid.

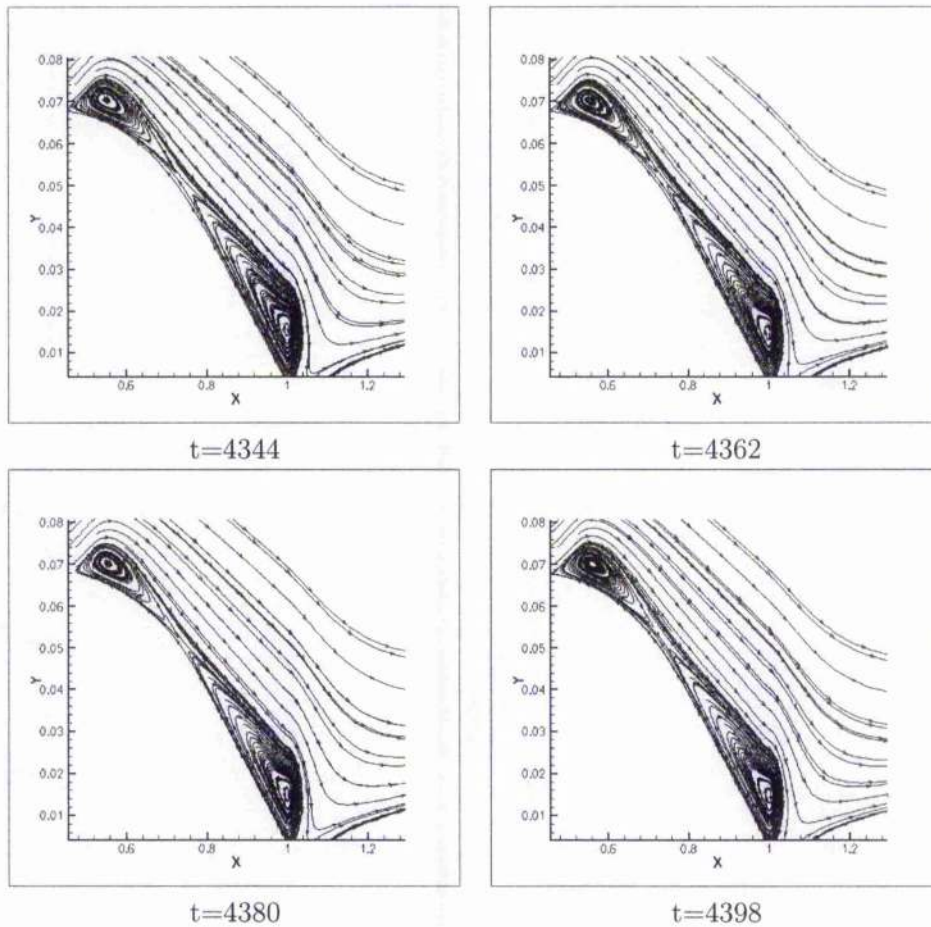


Figure 3.72: Temporal variation in separation regions during a downstream shock movement at $\alpha = 3.91^\circ$ using the Baseline model and the coarse grid.

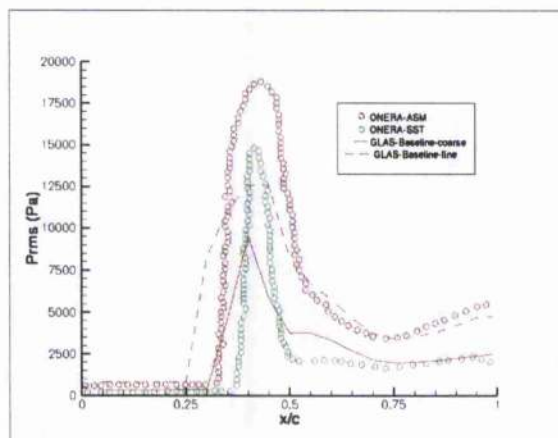


Figure 3.73: Pressure intensity plot along the upper surface at 4.5 deg.

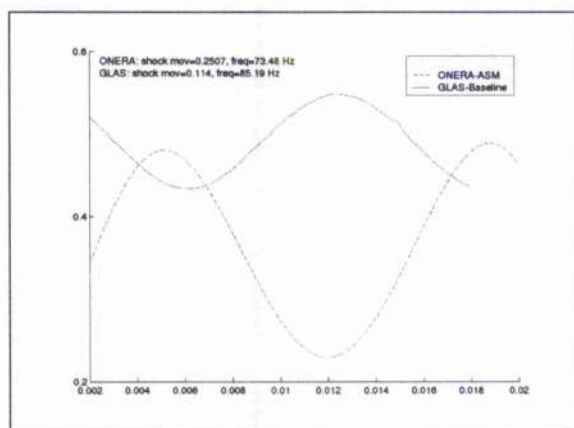


Figure 3.74: Shock movement at 4.5 deg.

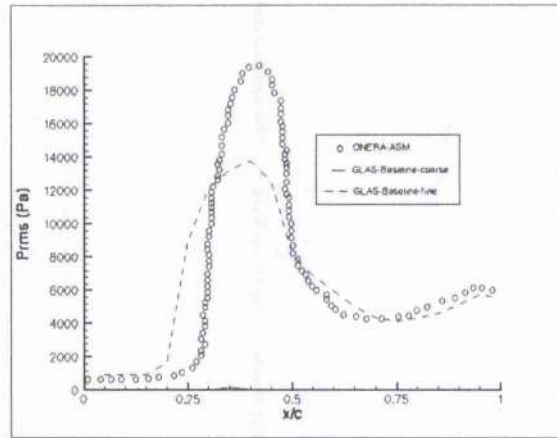


Figure 3.75: Pressure intensity plot along the upper surface at 5 deg.

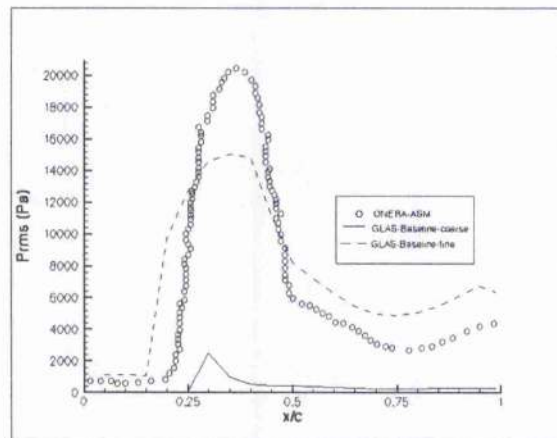


Figure 3.76: Pressure intensity plot along the upper surface at 5.5 deg.

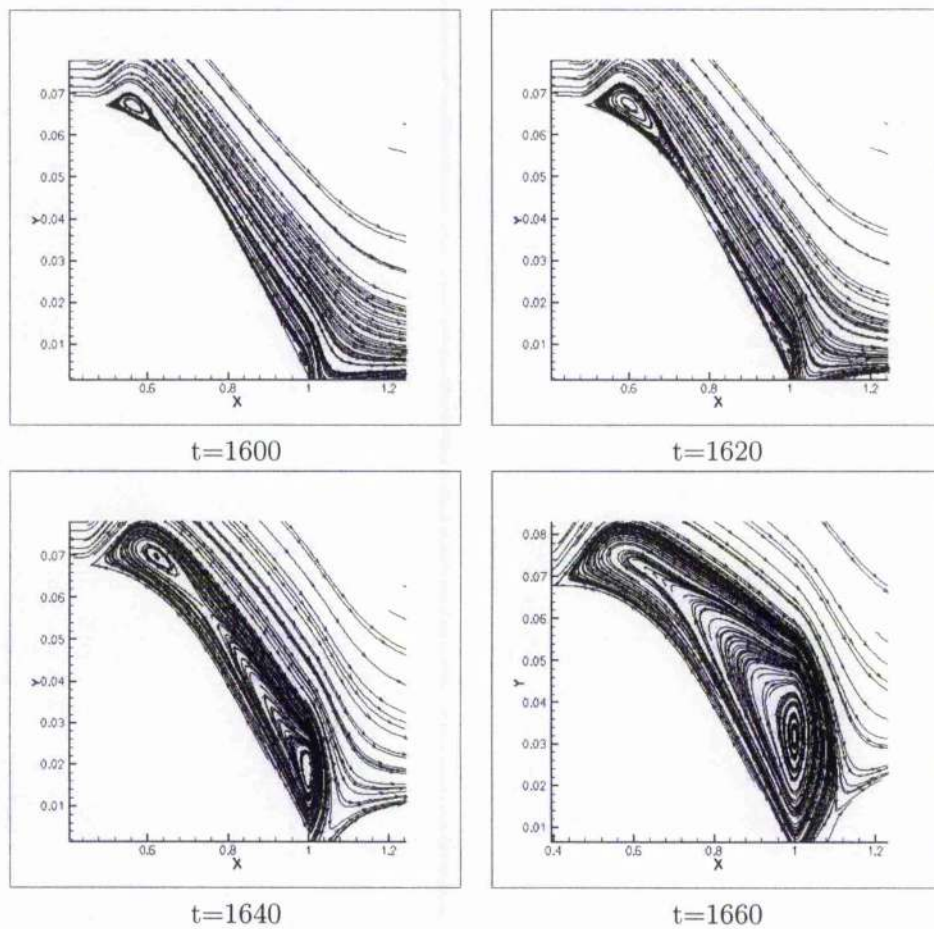


Figure 3.77: Temporal variation in separation regions during an upstream shock movement at $\alpha = 3.91^\circ$ using the Baseline model and the fine grid.

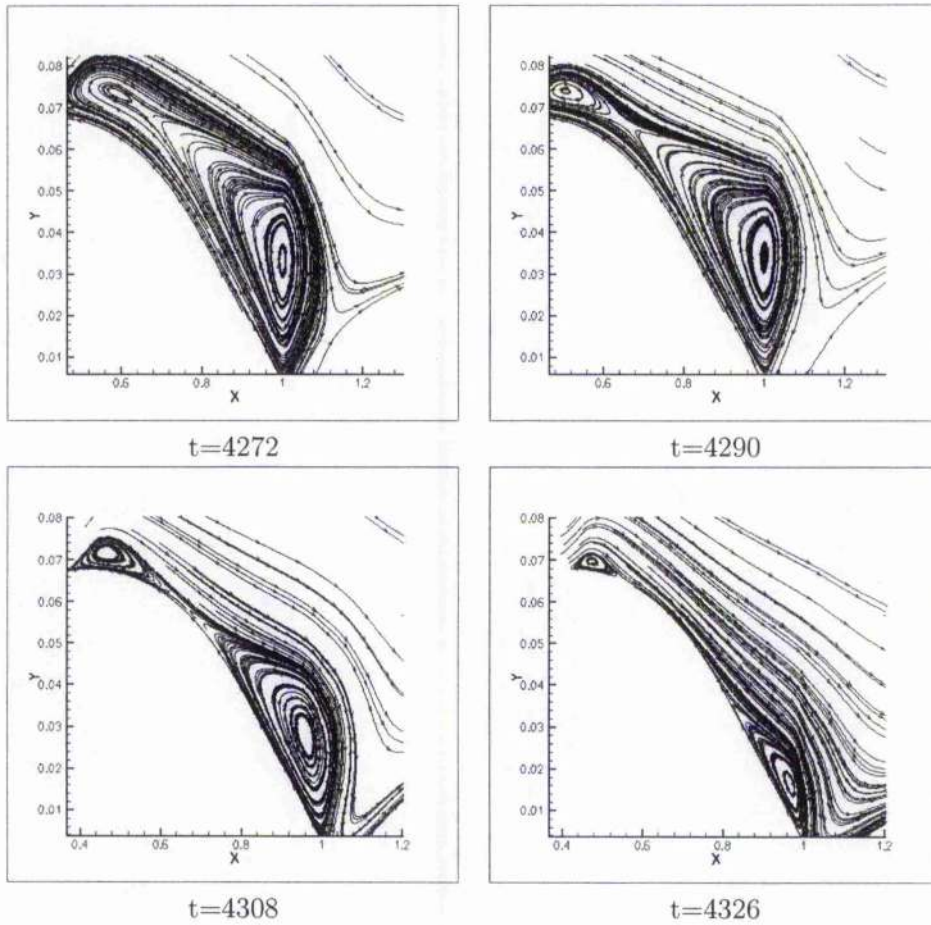


Figure 3.78: Temporal variation in separation regions during a downstream shock movement at $\alpha = 3.91^\circ$ using the Baseline model and the fine grid.

Chapter 4

Conclusion and Future Work

Both steady and unsteady characteristics of shock/boundary layer interaction have been investigated for two supercritical aerofoils using a CFD code developed at Glasgow University.

Steady results obtained demonstrated the shock/boundary layer classifications observed by experimentalists. At low angles of attack a weak shock with an attached boundary layer is formed. Increasing the angle of attack causes the shock to increase in strength allowing the boundary layer to separate at the foot of the shock forming a separation bubble followed by an attached flow and a trailing edge separation. At an increased angle of attack, there is total separation at the foot of the shock caused by a higher shock strength. The Baseline and SST models predicted the shock positions better than the other two models. However, the $k-\omega$ model gave better agreement with the regions of separation observed in experiments.

An investigation into the different boundary properties revealed that the $k-\omega$ model produced a more turbulent boundary layer before the shock. The

more turbulent flow is responsible for the delayed separation.

The difference in convergence levels of the steady solution was also used to explain why the different turbulence models produce different separation regions. It was concluded that attached flows can be related to good levels of convergence. Fluctuations tend to appear in both the mean and turbulent residual plots for higher angles of attack. These fluctuations occur because of emergence of separation regions.

Validation of the computational steady surface pressures showed a good agreement with experimental results for sub-critical flows. However, discrepancies appear for super-critical flows due to the emergence of adverse pressure gradients and separation regions.

Buffet was found to occur at higher angles of attack using the Baseline and SST models. Qualitatively the results obtained using the above turbulence models are in good agreement with experimental results obtained by Lee. However, the frequency of shock oscillation was under-predicted by both models. The Baseline model tends to over-predict the magnitude of shock movement whereas the SST model under-predicted the magnitude of shock movement.

It seems like the necessary condition for a buffet flow field is the interaction between circulation from the separation bubble and circulation from the trailing edge separation. The larger these separation regions are the heavier the buffet intensity. The communication between the shock strength and the trailing edge displacement thickness, and the coupling between the shock movement and the changes in the trailing edge pressures are responsible for the self-sustained shock movement.

A time step refinement study revealed that buffet occurs for time steps of 0.1 and below. Grid refinement studies revealed that the prediction of buffet using the SST model is heavily dependent on the grid density; only the fine and finer grids produced a buffet flow field. The frequency and magnitude of shock movement are heavily dependent on the employed grids, the frequency of shock oscillation decreases as the grid density increases. However further grid refinements are needed for both test cases in order to fully understand the effects of grid resolution on the buffet phenomenon. Another future study could be a detailed investigation into the influence of turbulence models on the buffet phenomenon. Both linear and non-linear models may be implemented in this study. Finally another interesting study will be to run calculations on three-dimensional grids and to compare and contrast with the two-dimensional results.

Appendix A

Summary of experimental work

Aerofoil Section	References	Tests Parameters	Available Data
BGK No.1	28,29	<ul style="list-style-type: none"> • $M=0.688$, $Re=20$ million • $\alpha=3.99$, 4.95, 6.43, 6.94 and 9 deg 	<ul style="list-style-type: none"> • Power spectra of normal force • Steady state pressure distribution • Pressure fluctuation/intensity plots • Skin friction plots • Normal force plots • Cross-correlation • buffet boundaries
	27,31	<ul style="list-style-type: none"> • $M=0.71$, $Re=20$ million • $\alpha=-0.316$, 1.396, 3.017, 4.905 and 6.970 deg 	<ul style="list-style-type: none"> • Power spectra of pressure • Steady state pressure distribution • Pressure fluctuation/intensity plots • Pressure-time histories plots • C_l v M plots • Normal force plots • Unsteady pressure distribution

Table 4.1: Summary of experimental work done on the BGK No.1 aerofoil

<i>Aerofoil Section</i>	References	Tests Parameters	Available Data
11.8% Joukowski		<ul style="list-style-type: none"> • Mach numbers in transonic range, $\alpha=0$ deg • $M=0.85-0.89$, $\alpha=3$ deg • $M=0.87-0.89$, $\alpha=6$ deg 	<ul style="list-style-type: none"> • No periodic flow at 0 deg • Periodic flow at 3 deg • Periodic flow at 6 deg

Table 4.2: Summary of experimental work on the Joukowski aerofoil

<i>Aerofoil Section</i>	References	Tests Parameters	Available Data
WTEA II	32	<ul style="list-style-type: none"> • $Re=20$ million • $M=0.612-0.792$ • $\alpha=0.886, 2.505, 3.736$ and 5.546 deg 	<ul style="list-style-type: none"> • Normal force fluctuation v lift coefficient plots • Power spectra of normal force • lift coefficient v M plots

Table 4.3: Summary of experimental work done on the WTEA II aerofoil

<i>Aerofoil Section</i>	References	Tests Parameters	Available Data
12% thick NACA 16	50	<ul style="list-style-type: none"> • Re=1.4 million, M=0.7-0.86 and alpha=0 deg • Re=1 million, alpha=6.7 deg, 	<ul style="list-style-type: none"> • classification of interactions • surface pressures • excitation spectra

Table 4.4: Summary of experimental work done on the 12% thick NACA 16 series aerofoil

<i>Aerofoil Section</i>	References	Tests Parameters	Available Data
NACA 0012		<ul style="list-style-type: none"> • Re=0.4-0.5 million, M=0.82-0.84 and alpha=0 deg • M=0.84-0.87, alpha=3 deg, • M=0.84-0.88, alpha=6 deg 	<ul style="list-style-type: none"> • Periodic flow at M=0.82-0.84 • Frequency v Mach number

Table 4.5: Summary of experimental work done on the NACA 0012

<i>Aerofoil Section</i>	<i>References</i>	<i>Tests Parameters</i>	<i>Available Data</i>
14% thick biconvex	42	<ul style="list-style-type: none"> • $M=0.86-0.9$ and $\alpha=0$ deg • $M=0.9$ and $\alpha=4$ deg 	<ul style="list-style-type: none"> • Periodic flow at both cases • Shock development with time • Frequency parameter with mach number

Table 4.6: Summary of experimental work done on the 14% thick biconvex aerofoil

<i>Aerofoil Section</i>	<i>References</i>	<i>Tests Parameters</i>	<i>Available Data</i>
Cast 7/DOA 1	70	<ul style="list-style-type: none"> • $Re=2-30$ million • Transonic Mach numbers • $\alpha=0-5$ deg 	<ul style="list-style-type: none"> • surface pressure plots • shock oscillation plots • trailing edge boundary layer thickness plots • shock strength • shock oscillation frequency and amplitude plots

Table 4.7: Summary of experimental work done on the Cast 7/DOA1 aerofoil

<i>Aerofoil Section</i>	References	Tests Parameters	Available Data
NACA 631-012		<ul style="list-style-type: none"> • Laminar • $M=0.65$ to 0.75 • $\text{Alpha}=0$ to 10 deg 	<ul style="list-style-type: none"> • Mean shock-wave position v alpha • flow regions • shock wave amplitude v alpha • frequency

Table 4.8: Summary of experimental work done on the NACA 631-012

<i>Aerofoil Section</i>	References	Tests Parameters	Available Data
18% circular arc	44	<ul style="list-style-type: none"> • $M=0.76$, $Re=11$ million • $\text{Alpha}=0$ deg 	<ul style="list-style-type: none"> • time histories of velocity, turbulent kinetic energy and turbulent shear stress • velocity and shear plots at different locations
	41	<ul style="list-style-type: none"> • $M=0.72$, 0.754 and 0.783 • $Re=11$ million • $\text{Alpha}=0$ deg 	<ul style="list-style-type: none"> • surface pressures • skin friction plots • Pressure-time histories plots

Table 4.9: Summary of experimental work done on the 18% circular arc

Appendix B

Numerical formulation and turbulence models

Numerical Formulation

Governing Equations

The governing equations represent the flow conservation laws and the fluid property laws. The conservative form of the governing equations is a convenient form of presenting the continuity, energy and momentum in computational fluid dynamics codes. In a three-dimensional Cartesian coordinate system, the non-dimensional form of the equation may be written as:

$$\frac{\partial \mathbf{W}}{\partial t} + \frac{\partial(\mathbf{F}^i - \mathbf{F}^v)}{\partial x} + \frac{\partial(\mathbf{G}^i - \mathbf{G}^v)}{\partial y} + \frac{\partial(\mathbf{H}^i - \mathbf{H}^v)}{\partial z} = 0 \quad (4.1)$$

Here the vector \mathbf{W} is the vector of conserved flow variables and is some-

times referred to as the solution vector. It can be written as:

$$\mathbf{W} = \begin{pmatrix} \rho \\ \rho u \\ \rho v \\ \rho w \\ \rho E \end{pmatrix} \quad (4.2)$$

In the above ρ is the density, u , v and w are the components of velocity given by the Cartesian velocity vector $\mathbf{U} = (u, v, w)$. Finally E is the total energy per unit mass. The flux vectors \mathbf{F} , \mathbf{G} , and \mathbf{H} consist of inviscid (ⁱ) and viscous (^v) diffusive parts. These are written in full as

$$\begin{aligned}
 \mathbf{F}^i &= \begin{pmatrix} \rho u \\ \rho u^2 + p \\ \rho uv \\ \rho uw \\ \rho uH \end{pmatrix} \\
 \mathbf{G}^i &= \begin{pmatrix} \rho v \\ \rho vu \\ \rho v^2 + p \\ \rho vw \\ \rho vH \end{pmatrix} \\
 \mathbf{H}^i &= \begin{pmatrix} \rho w \\ \rho wu \\ \rho wv \\ \rho w^2 + p \\ \rho wH \end{pmatrix}
 \end{aligned} \tag{4.3}$$

$$\begin{aligned}
 \mathbf{F}^\nu &= \frac{1}{Re} \begin{pmatrix} 0 \\ \tau_{xx} \\ \tau_{xy} \\ \tau_{xz} \\ u\tau_{xx} + v\tau_{xy} + w\tau_{xz} + q_x \end{pmatrix} \\
 \mathbf{G}^\nu &= \frac{1}{Re} \begin{pmatrix} 0 \\ \tau_{xy} \\ \tau_{yy} \\ \tau_{yz} \\ u\tau_{xy} + v\tau_{yy} + w\tau_{yz} + q_y \end{pmatrix} \\
 \mathbf{H}^\nu &= \frac{1}{Re} \begin{pmatrix} 0 \\ \tau_{xz} \\ \tau_{yz} \\ \tau_{zz} \\ u\tau_{xz} + v\tau_{yz} + w\tau_{zz} + q_z \end{pmatrix}
 \end{aligned} \tag{4.4}$$

$$\begin{aligned}
\tau_{xx} &= -\mu \left(2 \frac{\partial u}{\partial x} - \frac{2}{3} \left(\frac{\partial u}{\partial x} + \frac{\partial v}{\partial y} + \frac{\partial w}{\partial z} \right) \right) \\
\tau_{yy} &= -\mu \left(2 \frac{\partial v}{\partial y} - \frac{2}{3} \left(\frac{\partial u}{\partial x} + \frac{\partial v}{\partial y} + \frac{\partial w}{\partial z} \right) \right) \\
\tau_{zz} &= -\mu \left(2 \frac{\partial w}{\partial z} - \frac{2}{3} \left(\frac{\partial u}{\partial x} + \frac{\partial v}{\partial y} + \frac{\partial w}{\partial z} \right) \right) \\
\tau_{xy} &= -\mu \left(\frac{\partial u}{\partial y} + \frac{\partial v}{\partial x} \right) \\
\tau_{xz} &= -\mu \left(\frac{\partial u}{\partial z} + \frac{\partial w}{\partial x} \right) \\
\tau_{yz} &= -\mu \left(\frac{\partial v}{\partial z} + \frac{\partial w}{\partial y} \right)
\end{aligned} \tag{4.5}$$

and the heat flux vector components are written as

$$\begin{aligned}
q_x &= -\frac{1}{(\gamma - 1)M_\infty^2} \frac{\mu}{Pr} \frac{\partial T}{\partial x} \\
q_y &= -\frac{1}{(\gamma - 1)M_\infty^2} \frac{\mu}{Pr} \frac{\partial T}{\partial y} \\
q_z &= -\frac{1}{(\gamma - 1)M_\infty^2} \frac{\mu}{Pr} \frac{\partial T}{\partial z}
\end{aligned} \tag{4.6}$$

Here γ is the specific heat ratio, Pr is the laminar Prandtl number, T is the static temperature and M_∞ and Re are the freestream Mach number and Reynolds number, respectively. The various flow quantities are related

to each other by the perfect gas relations

$$\begin{aligned}
 H &= E + \frac{p}{\rho} \\
 E &= e + \frac{1}{2}(u^2 + v^2) \\
 p &= (\gamma - 1)\rho e \\
 \frac{p}{\rho} &= \frac{T}{\gamma M_\infty^2}
 \end{aligned} \tag{4.7}$$

The laminar viscosity μ is evaluated using Sutherland's law,

$$\frac{\mu}{\mu_0} = \left(\frac{T}{T_0}\right)^{3/2} \frac{T_0 + 110}{T + 110} \tag{4.8}$$

where μ_0 is a reference viscosity at a reference temperature T_0 . These can be taken as $\mu_0 = 1.7894 \times 10^{-5}$ kg/(m.s) with $T_0 = 288.16$ K. All quantities have been non-dimensionalised as follows:

$$x = \frac{x^*}{L^*}, \quad y = \frac{y^*}{L^*}, \quad t = \frac{t^*}{L^*/V_\infty^*},$$

$$u = \frac{u^*}{V_\infty^*}, \quad v = \frac{v^*}{V_\infty^*}, \quad \mu = \frac{\mu^*}{\mu_\infty^*},$$

$$\rho = \frac{\rho^*}{\rho_\infty^*}, \quad p = \frac{p^*}{\rho_\infty^* V_\infty^{*2}}, \quad T = \frac{T^*}{T_\infty^*}, \quad e = \frac{e^*}{V_\infty^{*2}} \quad (4.9)$$

Reynolds-averaged form

The instantaneous variables in a turbulent flow can be decomposed into a mean value and a fluctuating value. For example, density, pressure and velocity components are decomposed as:

$$\rho = \bar{\rho} + \rho', \quad P = \bar{P} + P', \quad u = \bar{u} + u', \quad v = \bar{v} + v', \quad w = \bar{w} + w'.$$

One reason why we decompose the variables is that in most engineering applications we are usually interested in the mean flow values rather than the time histories. Another reason is that a very fine grid will be needed in order to resolve all the turbulent scales and will also require a fine resolution in time. The Reynolds-averaged form of the Navier-Stokes equations are identical to those presented earlier, except for the stress tensor and heat flux vector components shown below. The variables should be considered as mean flow quantities (superscripts are dropped for clarity).

$$\begin{aligned}
\tau_{xx} &= -(\mu + \mu_T) \left(2 \frac{\partial u}{\partial x} - \frac{2}{3} \left(\frac{\partial u}{\partial x} + \frac{\partial v}{\partial y} + \frac{\partial w}{\partial z} \right) \right) + \frac{2}{3} \rho k \\
\tau_{yy} &= -(\mu + \mu_T) \left(2 \frac{\partial v}{\partial y} - \frac{2}{3} \left(\frac{\partial u}{\partial x} + \frac{\partial v}{\partial y} + \frac{\partial w}{\partial z} \right) \right) + \frac{2}{3} \rho k \\
\tau_{zz} &= -(\mu + \mu_T) \left(2 \frac{\partial w}{\partial z} - \frac{2}{3} \left(\frac{\partial u}{\partial x} + \frac{\partial v}{\partial y} + \frac{\partial w}{\partial z} \right) \right) + \frac{2}{3} \rho k \\
\tau_{xy} &= -(\mu + \mu_T) \left(\frac{\partial u}{\partial y} + \frac{\partial v}{\partial x} \right) \\
\tau_{xz} &= -(\mu + \mu_T) \left(\frac{\partial u}{\partial z} + \frac{\partial w}{\partial x} \right) \\
\tau_{yz} &= -(\mu + \mu_T) \left(\frac{\partial v}{\partial z} + \frac{\partial w}{\partial y} \right)
\end{aligned} \tag{4.10}$$

$$\begin{aligned}
q_x &= -\frac{1}{(\gamma - 1)M_\infty^2} \left(\frac{\mu}{Pr} + \frac{\mu_T}{Pr_T} \right) \frac{\partial T}{\partial x} \\
q_y &= -\frac{1}{(\gamma - 1)M_\infty^2} \left(\frac{\mu}{Pr} + \frac{\mu_T}{Pr_T} \right) \frac{\partial T}{\partial y} \\
q_z &= -\frac{1}{(\gamma - 1)M_\infty^2} \left(\frac{\mu}{Pr} + \frac{\mu_T}{Pr_T} \right) \frac{\partial T}{\partial z}
\end{aligned} \tag{4.11}$$

Curvilinear form

The model equations are written in curvilinear (ξ, η, ζ) form to facilitate use on curvilinear grids of arbitrary local orientation and density. A space transformation from the Cartesian co-ordinate system to the local coordinate system

must then be introduced

$$\begin{aligned}\xi &= \xi(x, y, z) \\ \eta &= \eta(x, y, z) \\ \zeta &= \zeta(x, y, z) \\ t &= t\end{aligned}$$

The Jacobian determinant of the transformation is given by

$$J = \frac{\partial(\xi, \eta, \zeta)}{\partial(x, y, z)}$$

The equation 4.1 can then be written as

$$\frac{\partial \hat{W}}{\partial t} + \frac{\partial(\hat{F}^i - \hat{F}^v)}{\partial \xi} + \frac{\partial(\hat{G}^i - \hat{G}^v)}{\partial \eta} + \frac{\partial(\hat{H}^i - \hat{H}^v)}{\partial \zeta} = 0 \quad (4.12)$$

where

$$\begin{aligned}\hat{W} &= \frac{W}{J} \\ \hat{F}^i &= \frac{1}{J} (\xi_x \mathbf{F}^i + \xi_y \mathbf{G}^i + \xi_z \mathbf{H}^i) \\ \hat{G}^i &= \frac{1}{J} (\eta_x \mathbf{F}^i + \eta_y \mathbf{G}^i + \eta_z \mathbf{H}^i) \\ \hat{H}^i &= \frac{1}{J} (\zeta_x \mathbf{F}^i + \zeta_y \mathbf{G}^i + \zeta_z \mathbf{H}^i) \\ \hat{F}^v &= \frac{1}{J} (\xi_x \mathbf{F}^v + \xi_y \mathbf{G}^v + \xi_z \mathbf{H}^v) \\ \hat{G}^v &= \frac{1}{J} (\eta_x \mathbf{F}^v + \eta_y \mathbf{G}^v + \eta_z \mathbf{H}^v) \\ \hat{H}^v &= \frac{1}{J} (\zeta_x \mathbf{F}^v + \zeta_y \mathbf{G}^v + \zeta_z \mathbf{H}^v)\end{aligned} \quad (4.13)$$

The expressions for the inviscid fluxes can be simplified somewhat by defining

$$\begin{aligned}
 U &= \xi_x u + \xi_y v + \zeta_z w \\
 V &= \eta_x u + \eta_y v + \zeta_z w \\
 W &= \zeta_x u + \zeta_y v + \zeta_z w
 \end{aligned}
 \tag{4.14}$$

The inviscid fluxes can then be written as

$$\begin{aligned}
 \hat{\mathbf{F}}^i &= \begin{pmatrix} \rho U \\ \rho u U + \xi_x p \\ \rho v U + \xi_y p \\ \rho w U + \xi_z p \\ \rho U H \end{pmatrix} \\
 \hat{\mathbf{G}}^i &= \begin{pmatrix} \rho V \\ \rho u V + \eta_x p \\ \rho v V + \eta_y p \\ \rho w V + \eta_z p \\ \rho V H \end{pmatrix} \\
 \hat{\mathbf{H}}^i &= \begin{pmatrix} \rho W \\ \rho u W + \zeta_x p \\ \rho v W + \zeta_y p \\ \rho w W + \zeta_z p \\ \rho W H \end{pmatrix}
 \end{aligned}
 \tag{4.15}$$

The derivative terms found in the viscous fluxes are evaluated using the chain rule, for example

$$\frac{\partial u}{\partial x} = \xi_x \frac{\partial u}{\partial \xi} + \eta_x \frac{\partial u}{\partial \eta} - \zeta_x \frac{\partial u}{\partial \zeta}$$

Steady State Solver

The Navier-Stokes equations are discretised using a cell-centred finite volume approach. The computational domain is divided into a finite number of non-overlapping control-volumes, and the governing equations are applied to each cell in turn. Also, the Navier-Stokes equations are re-written in a curvilinear co-ordinate system which simplifies the formulation of the discretised terms since body-conforming grids are adopted here. The spatial discretisation of equation 4.12 leads to a set of ordinary differential equations in time,

$$\frac{d}{dt} (\mathbf{W}_{i,j,k} V_{i,j,k}) = -\mathbf{R}_{i,j,k}(\mathbf{W}) \quad (4.16)$$

where \mathbf{W} and \mathbf{R} are the vectors of cell conserved variables and residuals respectively. The convective terms are discretised using Osher's upwind scheme for its robustness, accuracy, and stability properties. MUSCL variable extrapolation is used to provide second-order accuracy with the Van Albada limiter to prevent spurious oscillations around shock waves. Boundary conditions are set by using ghost cells on the exterior of the computational

domain. In the farfield ghost cells are set at the freestream conditions. At solid boundaries the no-slip condition is set for viscous flows, or ghost values are extrapolated from the interior (ensuring the normal component of the velocity on the solid wall is zero) for Euler flow.

The integration in time of equation 4.16 to a steady-state solution is performed using an implicit time-marching scheme by

$$\frac{\mathbf{W}_{i,j,k}^{n+1} - \mathbf{W}_{i,j,k}^n}{\Delta t} = -\frac{1}{V_{i,j,k}} \mathbf{R}_{i,j,k}(\mathbf{W}_{i,j,k}^{n+1}) \quad (4.17)$$

where $n+1$ denotes the time $(n+1) * \Delta t$. Equation 4.17 represents a system of non-linear algebraic equations and to simplify the solution procedure, the flux residual $\mathbf{R}_{i,j,k}(\mathbf{W}_{i,j,k}^{n+1})$ is linearised in time as follows,

$$\begin{aligned} \mathbf{R}_{i,j,k}(\mathbf{W}^{n+1}) &= \mathbf{R}_{i,j,k}(\mathbf{W}^n) + \frac{\partial \mathbf{R}_{i,j,k}}{\partial t} \Delta t + O(\Delta t^2) \\ &\approx \mathbf{R}_{i,j,k}^n(\mathbf{W}^n) + \frac{\partial \mathbf{R}_{i,j,k}}{\partial \mathbf{W}_{i,j,k}} \frac{\partial \mathbf{W}_{i,j,k}}{\partial t} \Delta t \\ &\approx \mathbf{R}_{i,j,k}^n(\mathbf{W}^n) + \frac{\partial \mathbf{R}_{i,j,k}}{\partial \mathbf{W}_{i,j,k}} \Delta \mathbf{W}_{i,j,k} \end{aligned} \quad (4.18)$$

where $\Delta \mathbf{W}_{i,j,k} = \mathbf{W}_{i,j,k}^{n+1} - \mathbf{W}_{i,j,k}^n$. Equation 4.17 now becomes the following linear system

$$\left[\frac{V_{i,j,k}}{\Delta t} \mathbf{I} + \frac{\partial \mathbf{R}_{i,j,k}}{\partial \mathbf{W}_{i,j,k}} \right] \Delta \mathbf{W}_{i,j,k} = -\mathbf{R}_{i,j,k}^n(\mathbf{W}^n) \quad (4.19)$$

The complexity of a direct method to compute a linear system is of the order of \mathcal{N}^3 , which becomes prohibitive when the total number of equations \mathcal{N} becomes large. On the other hand, iterative techniques such as Conjugate Gradient (CG) methods are capable of solving large systems of equations more efficiently in terms of time and memory. CG methods find an approximation to the solution of a linear system by minimising a suitable residual error function in a finite-dimensional space of potential solution vectors. A Krylov subspace algorithm is used to solve the linear system. The preconditioning strategy is based on a Block Incomplete Lower-Upper (BILU) factorisation since it appears to be the most promising and has the same sparsity pattern as the Jacobian matrix (BILU(0)) - i.e. the sparsity pattern of the Lower and Upper matrices is defined with respect to the sparsity of the unfactored matrix for simplicity. Furthermore the BILU(0) factorisation is decoupled between blocks to improve parallel efficiency and this approach does not seem to have a major impact on the effectiveness of the preconditioner as the number of blocks increases.

Implicit schemes require particular treatment during the early stages of

the iterative procedure. The usual approach in starting the method is to take a small CFL number and to increase it later on. However, it was found that smoothing out the initial flow doing some explicit iterations, and then switching to the implicit algorithm was equally efficient. In the present method, a specified number of forward Euler iterations are executed before switching to the implicit scheme.

The formulation leads to a Jacobian Matrix with a number of non-zero entries per row. Trying to reduce the number of non-zero entries would have several advantages. First, the memory requirements are lowered. Second, the resolution of the linear system by the GCG method is faster in terms of CPU-time since all the matrix-vector multiplications involved require less operation counts. Finally, the linear system is easier to solve since the approximate Jacobian matrix is more diagonally dominant. The steady state solver for the turbulent case is formulated and solved in an identical manner to that described above for the mean flow. The eddy-viscosity is regarded calculated from the latest values of k and ω (for example) and is used to advance the mean flow solution and then this new solution is used to update the turbulence solution, freezing the mean flow values. An approximate Jacobian is used for the source term by only taking into account the contribution of the dissipation terms \hat{D}_k and \hat{D}_ω i.e. no account of the production terms is taken on the left hand side of the system.

Unsteady State Solver

The formulation is described for the turbulent case. The laminar and inviscid cases represent a simplification of this.

Following the pseudo-time formulation, the updated mean flow solution is calculated by solving the steady state problems

$$\mathbf{R}_{i,j,k}^* = \frac{3\mathbf{w}_{i,j,k}^{n+1} - 4\mathbf{w}_{i,j,k}^n + \mathbf{w}_{i,j,k}^{n-1}}{2\Delta t} + \mathbf{R}_{i,j,k}(\tilde{\mathbf{w}}_{i,j,k}^{k_m}, \tilde{\mathbf{q}}_{i,j,k}^{k_t}) = 0 \quad (4.20)$$

$$\mathbf{Q}_{i,j,k}^* = \frac{3\mathbf{q}_{i,j,k}^{n+1} - 4\mathbf{q}_{i,j,k}^n + \mathbf{q}_{i,j,k}^{n-1}}{2\Delta t} + \mathbf{Q}_{i,j,k}(\tilde{\mathbf{w}}_{i,j,k}^{l_m}, \tilde{\mathbf{q}}_{i,j,k}^{l_t}) = 0. \quad (4.21)$$

Here k_m, k_t, l_m and l_t give the time level of the variables used in the spatial discretisation. Here the grid is moved rigidly but if grid deformation was required then time varying areas would be required in the expression for the real time derivative in equations 4.20 and 4.21. If $k_m = k_t = l_m = l_t = n + 1$ then the mean and turbulent quantities are advanced in real time in a fully coupled manner. However, if $k_m = l_m = l_t = n + 1$ and $k_t = n$ then the equations are advanced in sequence in real time, i.e. the mean flow is updated using frozen turbulence values and then the turbulent values are updated using the latest mean flow solution. This has the advantage that the only modification, when compared with the laminar case, to the discretisation of the mean flow equations is the addition of the eddy viscosity from the previous time step. The turbulence model only influences the mean flow solution

through the eddy viscosity and so any two equation model can be used without modifying the mean flow solver. Hence, the implementation is simplified by using a sequenced solution in real time. However, the uncoupling could adversely effect the stability and accuracy of the real time stepping, with the likely consequence of limiting the size of the real time step that can be used.

Equations (4.20) and (4.21) represent a coupled nonlinear system of equations. These can be solved by introducing an iteration through *pseudo time* τ to the steady state, as given by

$$\frac{\mathbf{w}_{i,j}^{n+1,m+1} - \mathbf{w}_{i,j}^{n+1,m}}{\Delta\tau} + \frac{3\mathbf{w}_{i,j}^{k_m} - 4\mathbf{w}_{i,j}^n + \mathbf{w}_{i,j}^{n-1}}{2\Delta t} + \mathbf{R}_{i,j}(\tilde{\mathbf{w}}_{i,j}^{k_m}, \tilde{\mathbf{q}}_{i,j}^{k_t}) = 0 \quad (4.22)$$

$$\frac{\mathbf{q}_{i,j}^{n+1,m+1} - \mathbf{q}_{i,j}^{n+1,m}}{\Delta\tau} + \frac{3\mathbf{q}_{i,j}^{l_t} - 4\mathbf{q}_{i,j}^n + \mathbf{q}_{i,j}^{n-1}}{2\Delta t} + \mathbf{Q}_{i,j}(\tilde{\mathbf{w}}_{i,j}^{l_m}, \tilde{\mathbf{q}}_{i,j}^{l_t}) = 0. \quad (4.23)$$

where the m -th pseudo-time iterate at the $n+1$ th real time step are denoted by $\mathbf{w}^{n+1,m}$ and $\mathbf{q}^{n+1,m}$ respectively. The iteration scheme used only effects the efficiency of the method and hence we can sequence the solution in pseudo time without compromising accuracy. For example, using explicit time stepping we can calculate $\mathbf{w}^{n+1,m+1}$ using $k_m = n+1, m$ and $k_t = n+1, m$ and $\mathbf{q}^{n+1,m+1}$ using $l_m = n+1, m+1$ and $l_t = n+1, m$. For implicit time stepping in pseudo time we can use $k_m = l_m = l_t = n+1, m+1$ and $k_t = n+1, m$. In both of these cases the solution of the equations is decoupled by freezing values but at convergence the real time stepping proceeds with no sequencing error. It is easy to recover a solution which is sequenced in real time

from this formulation by setting $k_t = n$ throughout the calculation of the pseudo steady state. This facilitates a comparison of the current pseudo time sequencing with the more common real time sequencing. In the code the pseudo steady-state problems are solved using the implicit steady state solver described in detail in section 4.

Turbulence Models

The Spalart-Allmaras (S-A) Turbulence Model

The S-A model is a one-equation model. This model is defined as follows:

Eddy Viscosity Function

$$\nu_T = \tilde{\nu} f_{v1} \quad (4.24)$$

where

$$f_{v1} = \frac{\chi^3}{\chi^3 + c_{v1}^3}, \quad \chi \equiv \frac{\tilde{\nu}}{\nu} \quad (4.25)$$

Convective Transport Equation of the Eddy Viscosity

$$\frac{D\tilde{\nu}}{Dt} = c_{b1}\tilde{S}\tilde{\nu} + \frac{1}{\sigma}[\nabla \cdot ((\nu + \tilde{\nu})\nabla\tilde{\nu}) + c_{b2}(\nabla\tilde{\nu})^2] - c_{w1}f_w \left[\frac{\tilde{\nu}}{d}\right]^2 \quad (4.26)$$

where

$$\tilde{S} \equiv S + \frac{\tilde{\nu}}{\kappa^2 d^2} f_{v2}, \quad f_{v2} = 1 - \frac{\chi}{1 + \chi f_{v1}} \quad (4.27)$$

and

$$f_w = g \left[\frac{1 + c_{w3}^6}{g^6 + c_{w3}^6} \right]^{1/6}, \quad g = r + c_{w2}(r^6 - r), \quad r \equiv \frac{\tilde{\nu}}{\tilde{S}\kappa^2 d^2}$$

Closure Coefficients

$$c_{b1} = 0.135, \quad \sigma = 2/3, \quad c_{b2} = 0.622, \quad \kappa = 0.41,$$

$$c_{w1} = 2.762, \quad c_{w2} = 0.3, \quad c_{w3} = 2, \quad c_{p1} = 7.1$$

$$c_{w1} = 2.762, \quad c_{w2} = 0.3, \quad c_{w3} = 2, \quad c_{p1} = 7.1 \quad (4.28)$$

The k - ω Turbulence Model

The two-equation k - ω model by Wilcox can be defined as follows:

Eddy Viscosity

$$\mu_T = \rho k / \omega \quad (4.29)$$

Turbulence Kinetic Energy

$$\rho \frac{\partial k}{\partial t} + \rho \mathbf{V} \cdot \nabla k - \frac{1}{Re} \nabla \cdot [(\mu + \sigma^* \mu_T) \nabla k] = P_k - \beta^* \rho k \omega \quad (4.30)$$

Specific Dissipation Rate

$$\rho \frac{\partial \omega}{\partial t} + \rho \mathbf{V} \cdot \nabla \omega - \frac{1}{Re} \nabla \cdot [(\mu + \sigma \mu_T) \nabla \omega] = P_\omega - \beta \rho \omega^2 \quad (4.31)$$

Closure Coefficients

$$\alpha = 5/9, \quad \beta = 3/40, \quad \beta^* = 9/100, \quad \sigma = 1/2, \quad \sigma^* = 1/2 \quad (4.32)$$

In the above relations the production terms of k and ω , P_k and P_ω respectively, are

$$P_k = \mu_T P - \frac{2}{3} \rho k S \quad (4.33)$$

$$P_\omega = \alpha \frac{\omega}{k} P_k \quad (4.34)$$

and

$$P = \left[(\nabla \mathbf{V} + \nabla \mathbf{V}^T) : \nabla \mathbf{V} - \frac{2}{3} (\nabla \cdot \mathbf{V})^2 \right] \quad (4.35)$$

$$S = \nabla \cdot \mathbf{V} \quad (4.36)$$

The equations as shown above use the same non-dimensional quantities as in section 3.1.1, with the addition of

$$k = \frac{k^* Re}{U_\infty^{*2}}, \quad \omega = \frac{\omega^* L^*}{U_\infty^*}, \quad \mu_T = \frac{\mu_T^*}{\mu_\infty^*} \quad (4.37)$$

The Shear Stress Transport (SST) Turbulence Model

The SST turbulence model of Menter is defined as follows:

Eddy Viscosity

$$\mu_T = \frac{\rho k / \omega}{\max [1; \Omega F_2 / (a_1 \omega)]}, \quad a_1 = 0.31 \quad (4.38)$$

In turbulent boundary layers the maximum value of the eddy viscosity is limited by forcing the turbulent shear stress to be bounded by the turbulent kinetic energy times a_1 . This effect is achieved by using an auxiliary function F_2 and an absolute value of the vorticity, Ω . This auxiliary function is defined as a function of the wall distance (y) as

$$F_2 = \tanh \left[\left(\max \left[2 \frac{\sqrt{k}}{0.09 \omega y}, \frac{500 \mu}{\rho y^2 \omega} \right] \right)^2 \right] \quad (4.39)$$

Turbulence Kinetic Energy

The two transport equations of the model are defined below with a blending function F_1 for the model coefficients of the original ω and ϵ model equations. The transport equation are given by

$$\rho \frac{\partial k}{\partial t} + \rho \mathbf{V} \cdot \nabla k - \frac{1}{Re} \nabla \cdot [(\mu + \sigma^* \mu_T) \nabla k] = P_k - \beta^* \rho k \omega \quad (4.40)$$

Specific Dissipation Rate

$$\rho \frac{\partial \omega}{\partial t} + \rho \mathbf{V} \cdot \nabla \omega - \frac{1}{Re} \nabla \cdot [(\mu + \sigma_{\omega} \mu_T) \nabla \omega] = P_{\omega} - \beta \rho \omega^2$$

$$+ 2(1 - F_1) \frac{\rho \sigma_{\omega 2}}{\omega} \nabla k \nabla \omega \quad (4.41)$$

Closure Coefficients

The function F_1 is designed to blend the model coefficients of the original $k - \omega$ model in boundary layer zones with the transformed $k - \epsilon$ model in free-shear layer freestream zones. This function takes the value of one on no-slip surfaces and near one over a large portion of the boundary layer, and goes to zero at the boundary layer edge. This auxiliary blending function, F_1 , is defined as

$$F_1 = \tanh \left[\left[\min \left(\max \left[\frac{\sqrt{k}}{0.09 \omega y}, \frac{500 \mu}{\rho y^2 \omega} \right]; \frac{4 \rho \sigma_{\omega 2} k}{CD_{k\omega} y^2} \right) \right]^4 \right] \quad (4.42)$$

where

$$CD_{k\omega} = \max \left[\frac{2 \rho \sigma_{\omega 2}}{\omega} \nabla k \nabla \omega; 10^{-20} \right]$$

where $CD_{k\omega}$ stands for cross-diffusion in the $k - \omega$ model. The constants are

$$a_1 = 0.31, \quad \beta^* = 0.09, \quad \kappa = 0.41 \quad (4.43)$$

The model coefficients β , γ , σ_k , and σ_ω denoted with the symbol ϕ are defined by blending the coefficients of the original $k - \omega$ model, denoted as ϕ_1 , with those of the transformed $k - \epsilon$ model, denoted ϕ_2 .

$$\phi = F_1\phi_1 + (1 - F_1)\phi_2,$$

where

$$\phi = [\sigma_k, \sigma_\omega, \beta, \gamma] \quad (4.44)$$

with the coefficients of the original models defined as

- Inner model coefficients

$$\sigma_{k1} = 0.85, \quad \sigma_{\omega1} = 0.5, \quad \beta_1 = 0.075,$$

$$\gamma_1 = \beta_1/\beta^* - \sigma_{\omega1}\kappa^2/\sqrt{\beta^*} = 0.553 \quad (4.45)$$

- Outer model coefficients

$$\sigma_{k2} = 1.0, \quad \sigma_{\omega2} = 0.856, \quad \beta_2 = 0.0828,$$

$$\gamma_2 = \beta_2/\beta^* - \sigma_{\omega2}\kappa^2/\sqrt{\beta^*} = 0.440 \quad (4.46)$$

Bibliography

- [1] Girodroux-Lavigne P, Le Balleur JC. “Unsteady viscous-inviscid interaction method and computation on buffeting over airfoils”. Proceedings of Joint IMA/SMIA Conference, Computational methods in aeronautical fluid dynamic, University of Reading, Berlin: Springer, 1987.
- [2] Alstatt MC. “An experimental and analytical investigation of a transonic shock-wave boundary layer interaction”. Technical Report AEDC TR 77-47, Arnold Engineering Development Center, May 1977.
- [3] Anderson JD Jr. “Fundamentals of Aerodynamics”. Second Edition, Aerospace Science Series, McGraw-Hill International Editions, 1991.
- [4] Baldwin B, Lomax H. “Thin layer approximation and algebraic model for separated turbulent flow”. AIAA 78-257, AIAA 16th Aerospace Sciences Meeting,, Huntsville, Alabama, January 1978.
- [5] Barakos G, Drikakis D. “An implicit unfactored method for unsteady turbulent compressible flows with moving solid boundaries”. *Comput Fluids*, 28(8):899–921, 1999.

-
- [6] Barakos G, Drikakis D. "Numerical simulation of transonic buffet flows using various turbulence closures". *Int J Heat fluid flow*, 21(5):620-6, 2000.
- [7] Bartels RE, Rothmayer AP. "An IBL approach to multi-scaled shock induced oscillation". AIAA 95-2157, AIAA 26th Fluid Dynamics Conference, San Diego, CA, June 1995.
- [8] Batina JT. "Unsteady transonic algorithm improvements for realistic aircraft configurations". *Aircraft J*, 26(2):131-9, 1989.
- [9] Bauer F, Garabedian PR, Korn D. "A Theory of Supercritical Wing Sections, with Computer Programs and Examples". *Lecture Notes in Economics and Mathematical Systems*, 66, 1972.
- [10] Benoit B, Legrain I. "Buffeting Prediction for Transport Aircraft Applications Based on unsteady Pressure Measurements". AIAA 87-2356, August 1987.
- [11] Bradshaw P. "An introduction to turbulence and its measurement". Pergamon Press, 1971.
- [12] Brunet V. "Computational Study of Buffet Phenomenon with Unsteady RANS Equations". AIAA Paper, 2003-3679, 2003.
- [13] Butefisch KA, Stanewsky E. "Experimental flow field study on a supercritical airfoil". *Aircraft J*, 24(11):783-8, 1987.
- [14] Cantariti F, Dubuc L, Gribben B, Woodgate M, Badcock K and Richards B. "Approximate Jacobians for the solution of the Euler

- and Navier-Stokes equations". Technical Report Technical Report 5, Aerospace Engineering, University of Glasgow, 1997.
- [15] Coe CF. "Buffet forces on two-dimensional airfoils as affected by thickness and thickness distribution". NACA RM A53K24, National Advisory Committee for Aeronautics, February 1954.
- [16] Couston M, Angelini J. "Numerical solutions of nonsteady two-dimensional transonic flows". *Fluid Eng J*, 101:341-7, 1979.
- [17] Deiweit GS. "Computation of separated transonic turbulent flows". AIAA-75-829, AIAA 8th Fluid and Plasma Dynamics Conference, Hartford, Connecticut, June 1975.
- [18] Edwards JW. "Transonic shock oscillations with a new boundary layer coupling method". AIAA 93-0777, AIAA 31st Aerospace Sciences Meeting, Reno, Nevada, January 1993.
- [19] Edwards JW, Thomas JL. "Computational methods for unsteady transonic flows". AIAA 87-0107, AIAA 25th Aerospace Sciences Meeting, Reno, Nevada, January 1987.
- [20] Eggleston B, Poole RJD. "Thick supercritical airfoils with low drag and natural laminar flow". *Aircraft J*, 24(6):405-11, 1987.
- [21] Finke K. "Unsteady shock-wave boundary-layer interaction on profiles in transonic flow". AGARD-CPP-168, Paper No.28., 1975.
- [22] Geissler W Ruiz-Calavera. "Transition and turbulence modelling for dynamic stall and buffet". www.sm.go.dlr.de/wolfgang/corsica.99.fr.pdf.

- [23] Gerteisen EA. "Computations of unsteady flows around airfoil sections by explicit and implicit methods solving the Euler and Navier-Stokes equations". AGARD CP-507, Transonic unsteady aerodynamics and aeroelasticity,, pages 13.1–13, San Diego, CA, USA, 7-11 October 1991.
- [24] Gibb J. "The cause and cure of periodic flows at transonic speeds". Proceedings 16th Congress of the International Council of the Aeronautical Sciences., pages 1522–30, Jerusalem, Israel, August–September 1988.
- [25] Gillan MA. "Computational analysis of buffet alleviation in viscous transonic flow over a porous airfoil". *AIAA J*, 33(4):769–772, 1995.
- [26] Hirose N, Miwa H. "Computational and experimental research on buffet phenomena of transonic airfoils". Technical Report TR-996 T, National Aerospace Laboratory, Japan, September 1988.
- [27] Jameson A. "Time dependent calculations using multigrid, with applications to unsteady flows past airfoils and wings". AIAA Paper, 91-1596, 1991.
- [28] Johnson DA, Bachalo WD, Owen FK. "Transonic flow past a symmetric airfoil at high angle of attack". AIAA 75-1500, AIAA 12th Fluid and Plasma Dynamics Conference,, Williamsburg, Virginia, July 1979.
- [29] Kawai N, Hirose N. "Development of the code NSFOIL for analyzing high Reynolds number transonic flow around an airfoil". *National Aerospace Laboratory*, NAL-TR-816:Japan, 1984.

-
- [30] Le Balleur JC, Girodroux-Lavigne P. "A viscous-inviscid interaction method for computing unsteady transonic separation". Proceedings of third Symposium on Numerical and Physical Aspects of Aerodynamic Flows, California State University, p. 252-71, 1986.
- [31] Le Balleur JC, Girodroux-Lavigne P. "Time-consistent computation of transonic buffet over airfoils". ICAS -88-5.52, Proceedings of 16th Congress of the International Council of the Aeronautical Sciences, p. 779-87, 1988.
- [32] Lee BHK. "Investigation of flow separation on a supercritical airfoil". *J Aircraft*, 26(11):1032-7, 1989.
- [33] Lee BHK. "Oscillatory shock motion on an airfoil caused by transonic shock boundary layer interactions". *AIAA J*, 28(5):942-4, 1990.
- [34] Lee BHK. "Transonic buffet on a supercritical airfoil". *Aeronaut J*, pages 143-52, May 1990.
- [35] Lee BHK. "Effect of trailing-edge flap on buffet characteristics of a supercritical airfoil". *J Aircraft*, 29(8):93-100, 1992.
- [36] Lee BHK. "Self-sustained shock oscillations on airfoils at transonic speeds". *Progress in Aerospace Sciences J*, 37:147-196, 2001.
- [37] Lee BHK and Ellis FA and Bureau J. "Investigation of the buffet characteristics of two supercritical airfoils". *J Aircraft*, 26(8):731-6, 1989.

-
- [38] Lee BHK, Murty H, Jiang H. "Calculation of compressible turbulent boundary layers with heat and mass transfer". *AIAA J*, 9(6):1091-7, 1971.
- [39] Lee BHK, Murty H, Jiang H. "Implicit finite-difference simulation of flow about arbitrary two-dimensional geometries". *AIAA J*, 16(7):673-86, 1978.
- [40] Lee BHK, Murty H, Jiang H. "Role of Kutta waves on oscillatory shock motion on an airfoil experiencing heavy buffeting". AIAA 93-1589, 34th AIAA/ASME/ASCE/AHS/ASC Structural Dynamics and Material Conference,, La Jolla, CA, April 1993.
- [41] Lee BHK, Murty H, Jiang H. "Role of Kutta waves on oscillatory shock motion on an airfoil". *AIAA J*, 32(4):789-96, 1994.
- [42] Lee BHK, Ohman L. "Unsteady pressure and force measurements associated with transonic buffeting of a two-dimensional supercritical aerofoil". Technical Report NAE-AN-14, National Research Council of Canada, June 1983.
- [43] Lee BHK, Tang FC. "An experimental study of transonic buffet of a supercritical airfoil with trailing edge flap". Technical Report NAE-AN-54, National Research Council of Canada, September 1988.
- [44] Lee BHK, Tang FC. "Transonic buffet of a supercritical airfoil with trailing-edge flap". *Aircraft J*, 26(5):459-64, 1989.

- [45] Lessen M, Fox JA, Zien HM. "On the inviscid stability of the laminar mixing of two parallel streams of a compressible fluid". *Fluid Mech J*, 23(2):335–67, 1965.
- [46] Levy Jr. LL. "Experimental and computational steady unsteady transonic flows about a thick airfoil". *AIAA J*, 16(6):564–72, 1978.
- [47] Liepmann HW and Roshko A. "Elements of Gasdynamics". John Wiley and Sons, New York, 1957.
- [48] Mabey DG and Welsh BL and Cripps BE. "Periodic flows on a rigid 14% thick biconcave wing at transonic speeds". Technical Report TR 81059, Royal Aircraft Establishment, May 1981.
- [49] Marvin JG. "Experiments planned specifically for developing turbulence models in computations of flow fields around aerodynamic shapes". AGARD Conference Proceedings No.210 on Numerical Methods and wind tunnel testing, Paper No.14, Von Karman Institute for Fluid Dynamics, Rhode-St-Genese, Belgium., June 1976.
- [50] Marvin JG and Levy Jr LL and Seegmiller HL. "Turbulence modeling for unsteady transonic flows". *AIAA J*, 18(5):489–96, 1980.
- [51] Mason WH. "Transonic Aerodynamics of Airfoils and Wings (DRAFT)". www.aoc.vt.edu/, 2002.
- [52] McDevitt JB. "Supercritical flow about a thick circular-arc airfoil". Technical Report NASA-TM-78549, National Aeronautics and Space Administration, January 1979.

-
- [53] McDevitt JB and Levy Jr LL and Deiwert GS. "Transonic flow past a thick circular-arc airfoil". *AIAA J*, 14(5):606-13, 1976.
- [54] McDevitt JB, Okuno AF. "Static and dynamic pressure measurements on a NACA 0012 airfoil in the Ames High Reynolds Number Facility.". Technical Report NASA TP-2485, National Aeronautics and Space Administration, USA, 1985.
- [55] Menter FR. "Zonal two equation kappa-omega turbulence models for aerospace flows". AIAA Paper, 93-2906, 1993.
- [56] Menter FR. "Zonal two equation k- ω models for aerodynamic flows". AIAA 99-3118, July 1993.
- [57] Mohan SR. "Periodic flows on rigid aerofoils at transonic speeds". AIAA-91-0598, 29th Aerospace Sciences Meeting, Hartford Connecticut, January 1991.
- [58] Mundell ARG and Mabey DG. "Pressure fluctuations caused by transonic shock/boundary-layer interaction". *Aeronaut J*, pages 274-81, Aug/Sept 1986.
- [59] Nagano Y, Kim C. "A two equation model for heat transport in wall turbulent shear flows". *Heat Transfer J*, 110:583-9, 1988.
- [60] Pearcy HH. "A method for the prediction of the onset of buffeting and other separation effects from wind tunnel tests on rigid models.". Technical Report AGARD Report 223, 1958.

- [61] Pearcy HH, Osborne J and Haines AB. "The interaction between local effects at the shock and rear separation-a source of significant scale effects in wing-tunnel tests on airfoils and wings". Paper 11 AGARD CP 35, 1968.
- [62] Raghunathan S. "Passive control of shock-boundary layer interaction". *Prog Aerosp Sci*, 25:271-96, 1988.
- [63] Raghunathan S, Gillian MA, Cooper RK, Mitchell RD, Cole JS. "Shock oscillations on biconvex aerofoils". *Aerospace Sci Technol*, 3(1):1-9, 1999.
- [64] Raghunathan S, Hall DE, Mabey DG. "Alleviation of shock oscillations in transonic flow by passive controls". *Aeronaut J*, 937:245-50, 1990.
- [65] Raghunathan S, Mitchell RD, Gillan MA. "Transonic shock oscillations on NACA0012 aerofoil". *Shock Waves*, 8(4):191-202, 1998.
- [66] Redeker G and Proksch HJ. "The prediction of buffet onset and light buffet by means of computational methods". Technical Report AGARD CP-204, NASA Ames Research Centre, Moffat Field, CA, USA, September 1976.
- [67] Reynolds WC. "Large-scale instabilities of turbulent wakes". *Fluid Mech J*, 54(3):481-8, 1972.
- [68] Roos FW. "Surface pressure and wake flow fluctuations in a supercritical airfoil flowfield". AIAA 75-66, AIAA 13th Aerospace Sciences Meeting,, Pasadena, California, January 1975.

- [69] Roos FW. "Some features of unsteady pressure field in transonic airfoil buffeting". *J Aircraft*, 17(11):781–8, 1980.
- [70] Rumsey CL and Thomas JL and Warren GP and Liu GC. "Upwind Navier-Stokes solutions for separated periodic flows". AIAA-86-0247, AIAA 24th Aerospace Sciences Meeting, Reno, Reno Nevada, January 1986.
- [71] Rumsey Cl, Sanetrik MD, Biedron RT, Melson ND, Parlette EB. "Efficiency and Accuracy of time-accurate turbulent Navier-Stokes computations". AIAA-95-1835, 13th AIAA Applied Aerodynamics Conference, San Diego CA, June 1995.
- [72] Seegmiller HL and Marvin JG and Levy Jr LL. "Steady and unsteady transonic flow". *AIAA J*, 16(12):1262–70, 1978.
- [73] Shen-Jwu Su, Chuen-Yen Chow. "Improvement of transonic buffet by geometric modifications". *Aircraft J*, 32(4):901–903, 1995.
- [74] Singh JP. "Estimation of shock-induced buffet onset". *Acta Mechanica*, 151(3-4):245–253, 2001.
- [75] Sod GA. "Numerical methods in fluid dynamics". Cambridge University Press, UK, 1985.
- [76] Sorenson RM, Wyss JA, Kyle JC. "Preliminary investigation of the pressure fluctuations in the wakes of two-dimensional wings at low angles of attack". NACA RM A51G10, October 1951.

- [77] Spalart P, Allmaras S. "A one-equation turbulence model for aerodynamic flows". AIAA 92-0439, AIAA 30th Aerospace Sciences Meeting and Exhibit,, Reno, Nevada, January 1992.
- [78] Spee BM. "Wave propagation in transonic flow past two-dimensional aerofoils". Technical Report NLT-TN-T.123, National Aerospace Laboratory, July 1966.
- [79] Stanewsky F, Basler D. "Experimental investigation of buffet onset and penetration on a supercritical airfoil at transonic speeds". AGARD CP-483, Aircraft dynamic loads due to flow separation,, Sorrento Italy, 1-6 April 1990.
- [80] Tijdeman H. "Investigation of the transonic flow around oscillation airfoils". Technical Report NLR TR 77090, National Aerospace Laboratory, The Netherlands, 1977.
- [81] Wilcox DC. "Turbulence modelling for CFD". DCW Industries, La Canada, California, 1993.

